Kiloparsec-scale outflows are prevalent among luminous AGN: outflows and feedback in the context of the overall AGN population

C. M. Harrison,[1][*] D. M. Alexander,[1] J. R. Mullaney[1,2] and A. M. Swinbank[3]

[1]*Department of Physics, Durham University, South Road, Durham DH1 3LE, UK*
[2]*Department of Physics & Astronomy, University of Sheffield, Sheffield S3 7RH, UK*
[3]*Institute for Computational Cosmology, Durham University, South Road, Durham DH1 3LE, UK*

ABSTRACT

We present integral field unit observations covering the [O III]$\lambda\lambda$4959, 5007 and Hβ emission lines of 16 $z < 0.2$ type 2 active galactic nuclei (AGN). Our targets are selected from a well-constrained parent sample of $\approx$24 000 AGN so that we can place our observations into the context of the overall AGN population. Our targets are radio quiet with star formation rates (SFRs; $\lesssim$[10–100] M$_\odot$ yr^{-1}) that are consistent with normal star-forming galaxies. We decouple the kinematics of galaxy dynamics and mergers from outflows. We find high-velocity ionized gas (velocity widths $\approx$600–1500 km s^{-1}; maximum velocities $\leq$1700 km s^{-1}) with observed spatial extents of $\gtrsim$(6–16) kpc in all targets and observe signatures of spherical outflows and bi-polar superbubbles. We show that our targets are representative of $z < 0.2$, luminous (i.e. $L_{\rm [O\,III]} > 10^{41.7}$ erg s^{-1}) type 2 AGN and that ionized outflows are not only common but also in $\geq$70 per cent (3σ confidence) of cases, they are extended over kiloparsec scales. Our study demonstrates that galaxy-wide energetic outflows are not confined to the most extreme star-forming galaxies or radio-luminous AGN; however, there may be a higher incidence of the most extreme outflow velocities in quasars hosted in ultraluminous infrared galaxies. Both star formation and AGN activity appear to be energetically viable to drive the outflows and we find no definitive evidence that favours one process over the other. Although highly uncertain, we derive mass outflow rates (typically $\approx$10 times the SFRs), kinetic energies ($\approx$0.5–10 per cent of $L_{\rm AGN}$) and momentum rates (typically $\gtrsim$10–20 $\times$ $L_{\rm AGN}/c$) consistent with theoretical models that predict AGN-driven outflows play a significant role in shaping the evolution of galaxies.

Key words: galaxies: active – galaxies: evolution – galaxies: kinematics and dynamics – quasars: emission lines.

1 INTRODUCTION

One of the most remarkable discoveries in modern astronomy is that all massive galaxies host supermassive black holes (BHs) with masses that are proportional to that of their host galaxy spheroid (e.g. Kormendy & Richstone 1995; Magorrian et al. 1998; Tremaine et al. 2002; Gültekin et al. 2009; see Kormendy & Ho 2013 for a review). These BHs primarily grow through mass accretion that is visible as active galactic nuclei (AGN) in the centre of galaxies. Theoretical models of galaxy formation have found it necessary to implement AGN 'feedback' processes, during which AGN activity injects energy into the gas in the larger scale environment, in order to reproduce the properties of local massive galaxies, intracluster gas and the intergalactic medium (e.g. BH mass–spheroid mass relationship; the sharp cut-off in the galaxy luminosity function; colour bi-modality; metal enrichment; X-ray temperature–luminosity re-

lationship; e.g. Silk & Rees 1998; Churazov et al. 2005; Bower et al. 2006; Hopkins et al. 2006; McCarthy et al. 2010; Gaspari et al. 2011). Placing observational constraints on how AGN activity couples to the gas in galaxies and haloes, and where these processes are most prevalent, is an important area of ongoing research (for reviews see Cattaneo et al. 2009; Alexander & Hickox 2012; Fabian 2012; McNamara & Nulsen 2012).

Several of the most successful galaxy formation models invoke a dramatic form of energy injection (sometimes called the 'quasar mode' or 'starburst mode') where AGN drive galaxy-wide (i.e. $\gtrsim$0.1–10 kpc) energetic outflows that expel gas from their host galaxies and consequently this shuts down future BH growth and star formation and/or enriches the larger scale environment with metals (e.g. Silk & Rees 1998; Fabian 1999; Benson et al. 2003; King 2003; Granato et al. 2004; Di Matteo, Springel & Hernquist 2005; Springel, Di Matteo & Hernquist 2005; Hopkins et al. 2006, 2008; Booth & Schaye 2010; Debuhr, Quataert & Ma 2012). This is in contrast to the 'maintenance mode' (or 'hot-halo') feedback

where radio jets, launched by AGN, control the level of cooling of the hot gas in the most massive haloes (see Bower, Benson & Crain 2012; Harrison 2013, for a discussion on the two modes). While there is little doubt that star formation processes (e.g. stellar winds and supernovae) drive galaxy-wide outflows (e.g. Heckman, Armus & Miley 1990; Lehnert & Heckman 1996; Swinbank et al. 2009; Genzel et al. 2011; Newman et al. 2012; Bradshaw et al. 2013; see review in Veilleux, Cecil & Bland-Hawthorn 2005) and are an integral part of galaxy evolution (e.g. Dalla Vecchia & Schaye 2008; Hopkins et al. 2013a), it is believed that AGN activity is required to drive the highest velocity outflows and are particularly important for the evolution of the most massive galaxies (e.g. Benson et al. 2003; McCarthy et al. 2011; Hopkins et al. 2013b; Zubovas & King 2014).

X-ray and ultraviolet spectroscopy has shown that a high fraction, and potentially all, of high accretion rate AGN drive high-velocity outflows ($v \approx 0.1c$) close to their accretion discs (i.e. on subparsec scales; e.g. Blustin et al. 2003; Reeves, O'Brien & Ward 2003; Ganguly & Brotherton 2008; Tombesi et al. 2010; Gofford et al. 2011). However, are AGN capable of driving outflows over galaxy scales as is required by galaxy formation models? A diagnostic that is commonly used to identify outflowing gas over large scales is broad (i.e. exceeding that expected from galaxy dynamics), asymmetric and high-velocity [O III] λ5007 emission-line profiles. This emission line traces the kinematics of the ionized gas; however, we briefly note that outflowing gas has been observed in multiple gas phases in some AGN (e.g. Martin 2005; Rupke, Veilleux & Sanders 2005; Feruglio et al. 2010; Fischer et al. 2010; Alatalo et al. 2011; Cimatti et al. 2013; Rupke & Veilleux 2013; Veilleux et al. 2013). As a forbidden transition the [O III] λ5007 emission line cannot be produced in the high-density subparsec scales of the AGN broad-line region (BLR) making it a good tracer of the kinematics in the narrow-line region (NLR) and can be observed over parsecs to tens of kiloparsecs (e.g. Wampler et al. 1975; Boroson, Persson & Oke 1985; Wilson & Heckman 1985; Stockton & MacKenty 1987; Osterbrock 1989). The [O III] λ5007 emission line has long been used to identify outflowing ionized gas in small samples of local and low-redshift AGN (e.g. Weedman 1970; Stockton 1976; Heckman et al. 1981; Veron 1981; Feldman et al. 1982; Heckman, Miley & Green 1984; Vrtilek 1985; Whittle 1985; Whittle et al. 1988; Veilleux 1991; Boroson & Green 1992; Veilleux et al. 1995; Nelson & Whittle 1996); however, the small sample sizes make it difficult to know how representative these observations are. More recently, large systemic spectroscopic surveys [e.g. the Sloan Digital Sky Survey (SDSS); York et al. 2000] have enabled the study of NLR kinematics in hundreds to tens of thousands of AGN (e.g. Boroson 2005; Greene & Ho 2005; Komossa et al. 2008; Wang, Mao & Wei 2011; Zhang et al. 2011; Mullaney et al. 2013) that can constrain both the ubiquity of these outflow features and study them as a function of key AGN properties.

Mullaney et al. (2013) used the SDSS spectroscopic data base to study the one-dimensional kinematic properties of [O III] λ5007 by performing multicomponent fitting to the optical emission-line profiles of $\approx$24 000, $z < 0.4$ optically selected AGN. They showed that $\approx$17 per cent of the AGN have emission-line profiles that indicate their ionized gas kinematics are *dominated* by outflows and a considerably larger fraction are likely to host ionized outflows at lower levels. The fraction of AGN with ionized gas kinematics dominated by outflows increases to $\gtrsim$40 per cent for the more radio-luminous AGN (i.e. those with $L_{1.4\,\mathrm{GHz}} > 10^{23}$ W Hz^{-1}), in contrast, when taking into account intrinsic correlations, this fraction shows little dependence on [O III] luminosity or Eddington ratio (Mullaney et al.

2013). In agreement with smaller studies (e.g. Heckman et al. 1981; Whittle 1985, 1992; Gelderman & Whittle 1994; Nelson & Whittle 1996; Nesvadba et al. 2011; Kim et al. 2013; see also Greene & Ho 2005), this result shows that ionized outflows are most common in AGN that have moderate-to-high radio luminosities. However, while insightful, the origin of the radio emission is often unknown, particularly at the moderate radio luminosities (i.e. $L_{1.4\,\mathrm{GHz}} \approx 10^{23}$–$10^{24}$ W Hz^{-1}) where AGN cores, radio jets, shocks and high levels of star formation could all contribute (e.g. Condon et al. 2013; Del Moro et al. 2013; Zakamska & Greene 2014). It is therefore vital to measure star formation rates (SFRs) and properly investigate the origin of the radio emission in the sources that host these outflows to properly interpret these results.

The one-dimensional spectra discussed above provide no insight into the spatial extent or structure of the outflows, for this, we must appeal to spatially resolved spectroscopy. Both longslit and integral field unit (IFU) observations of AGN, over a large range of redshifts, have identified disturbed and high-velocity ionized gas over kiloparsec scales (e.g. McCarthy, Baum & Spinrad 1996; Colina, Arribas & Borne 1999; Villar-Martín, Binette & Fosbury 1999; Nesvadba et al. 2007, 2008; Holt, Tadhunter & Morganti 2008; Fu & Stockton 2009; Lipari et al. 2009; Lípari et al. 2009; Alexander et al. 2010; Humphrey et al. 2010; Greene et al. 2011; Rupke & Veilleux 2011, 2013; Cano-Díaz et al. 2012; Harrison et al. 2012; Westmoquette et al. 2012; Förster Schreiber et al. 2013; Husemann et al. 2013; Liu et al. 2013a,b). Several of these studies have revealed considerable masses of outflowing ionized gas with velocities higher than the galaxy escape velocities, in apparent agreement with basic predictions from galaxy formation models. However, a key limitation of these studies is that it is often difficult to place these observations into the context of the overall AGN and galaxy populations as the samples are small, inhomogeneous and/or only represent the most extreme AGN or star-forming systems in the Universe.

In this paper we are interested in measuring the prevalence, properties and the potential impact of galaxy-wide energetic outflows. We present Gemini (South) Multi-Object Spectrograph (GMOS; Allington-Smith et al. 2002) IFU observations of 16 $0.08 < z < 0.2$ type 2 AGN drawn from the parent sample of Mullaney et al. (2013). Importantly, this means that we can place our IFU observations into the context of the overall AGN population. So that we can properly interpret our results, we perform Spectral Energy Distribution (SED) fitting and analyse the available radio data to measure SFRs, AGN luminosities and to search for evidence of radio jets in all of our targets. In Section 2, we give details of the IFU observations, data reduction and SED fitting. In Section 3, we provide details of our analysis of the ionized gas kinematics and in Section 4 we present our results. In Section 5 we discuss our results and their implication for understanding galaxy evolution and in Section 6 we give our conclusions. We provide background information and a discussion of the results on individual sources in Appendix A. We have adopted $H_0 = 71$ km s^{-1} Mpc^{-1}, $\Omega_{\mathrm{M}} = 0.27$ and $\Omega_{\Lambda} = 0.73$ throughout; in this cosmology, 1 arcsec corresponds to $\approx$1.5–3.3 kpc for the redshift range of our sample ($z = 0.08$–0.2).

2 TARGETS, OBSERVATIONS AND DATA REDUCTION

2.1 Target selection

We are interested in studying the spatially resolved ionized gas kinematics in luminous AGN, with the aim of understanding the prevalence and properties of galaxy-wide ionized outflows. For this

study, we selected 16 $z < 0.2$ type 2 AGN from the parent catalogue of Mullaney et al. (2013) to observe with the GMOS (South) IFU. We describe our selection criteria below (also illustrated in Fig. 1) and we provide a list of the targets, along with their positions and redshifts, in Table 1.

Our parent catalogue (Mullaney et al. 2013) contains fits to the emission-line profiles of 24 264, $z < 0.4$, optical AGN (identified using a combination of 'BPT' diagnostics; Baldwin, Phillips & Terlevich 1981 and emission-line widths) from the SDSS data release Data Release 7 (DR7; Abazajian et al. 2009). Mullaney et al. (2013) decompose the [O III] λ5007 emission-line profiles into two components ('narrow' and 'broad') to identify emission-line profiles that are broad and asymmetric, indicative of outflow kinematics. A primary aim of this work is to establish if the broad and asym-
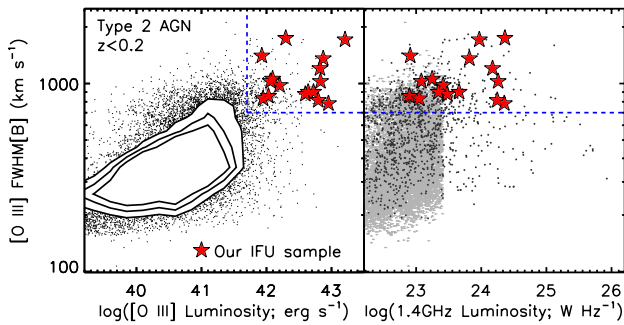
Figure 1. Left: the FWHM of the broadest, luminous (contributes at least 30 per cent of the total flux; FWHM[B]) [O III] emission-line component versus total [O III] luminosity for our IFU targets (red stars) compared to the overall population of $z < 0.2$ type 2 AGN (black data points and contours; Mullaney et al. 2013). The dashed lines show the selection criteria used to select the luminous AGN ($L_{\text{[OIII]}} > 5 \times 10^{41}$ erg s^{-1}) with the spectral signatures of ionized outflows ([O III] FWHM[B] > 700 km s^{-1}). Right: FWHM[B] versus 1.4 GHz luminosity; the symbols are the same as in the left-hand panel (with the addition of upper limits plotted in grey).

Table 1. Positions and redshifts for the type 2 AGN in our IFU sample.

Name (1)	RA (J2000) (2)	Dec (J2000) (3)	Run (4)	z_{sys} (5)	FWHM[B] (6)
J0945+1737	09:45:21.33	+17:37:53.2	10	0.1283	1027
J0958+1439	09:58:16.88	+14:39:23.7	10	0.1092	878
J1000+1242	10:00:13.14	+12:42:26.2	10	0.1480	815
J1010+1413	10:10:22.95	+14:13:00.9	10	0.1992	1711
J1010+0612	10:10:43.36	+06:12:01.4	10	0.0984	1743
J1100+0846	11:00:12.38	+08:46:16.3	10	0.1005	1203
J1125+1239	11:25:46.35	+12:39:22.6	12	0.1669	1028
J1130+1301	11:30:28.86	+13:01:19.6	12	0.1353	857
J1216+1417	12:16:22.73	+14:17:53.0	12	0.0818	1404
J1316+1753	13:16:42.90	+17:53:32.5	10	0.1505	1357
J1338+1503	13:38:06.53	+15:03:56.1	12	0.1857	901
J1339+1425	13:39:56.48	+14:25:29.6	12	0.1390	830
J1355+1300	13:55:45.66	+13:00:51.0	12	0.1519	1058
J1356+1026	13:56:46.10	+10:26:09.0	10	0.1238	783
J1430+1339	14:30:29.88	+13:39:12.0	10	0.0855	901
J1504+0151	15:04:20.90	+01:51:59.4	12	0.1827	978

Notes: Details of the targets that we observed with the Gemini-GMOS IFU. (1) Object name; (2)–(3) optical RA and DEC positions from SDSS (DR7); (4) the Gemini-GMOS run when we observed this object (see Section 2.2); (5) systemic redshifts derived from this work (see Section 3.2); (6) FWHM (in km s^{-1}) of the broadest, luminous (contributes at least 30% of the total flux) [O III]λ5007 emission-line component from Mullaney et al. (2013).

metric emission-line features observed in one-dimensional spectra are spatially extended and we therefore selected sources that have a luminous broad [O III] λ5007 emission-line component. Our definition of a luminous broad component is one that contributes at least 30 per cent of the total flux and has full width at half-maximum (FWHM) > 700 km s^{-1} (see Fig. 1). Additionally, we only selected sources that are classified as type 2 AGN by Mullaney et al. (2013), i.e. the permitted and forbidden lines are of similar width, implying that we cannot directly see the BLR in these objects (e.g. Antonucci 1993). From these, we selected the sources that have total observed [O III] luminosities of $L_{\text{[O III]}} > 5 \times 10^{41}$ erg s^{-1} and have a redshift $z < 0.2$ to ensure sufficient emission-line flux for measuring the spatially resolved kinematics with reasonable exposure times for our IFU observations. Finally, we chose 16 targets with celestial co-ordinates that are accessible with Gemini-South. Our final target list is given in Table 1 and we give notes in Appendix A on the relevant multiwavelength observations of these targets that can be found in the literature. The majority of our targets have received little or no attention previously in the literature, with the exceptions of J0945+1737, J1316+1753 and J1356+1026 that have been studied in some detail (see Appendix A).

It is important to address where our targets fit into the overall AGN population if we are to draw global conclusions from our observations. First, we note that our targets are all type 2 AGN, which are thought to constitute at least half of the overall AGN population (e.g. Lawrence & Elvis 2010), and that they have *observed* [O III] luminosities in the range $L_{\text{[O III]}} = 10^{41.9}$–$10^{43.2}$ erg s^{-1} (see Table 2) that fit the luminosity criteria for type 2 ('obscured') quasars (i.e. $L_{\text{[O III]}} \gtrsim 10^{41.9}$ erg s^{-1}; Reyes et al. 2008). The absorption corrected [O III] luminosities of our targets have the range $L_{\text{[O III]}} = 10^{42.4}$–$10^{43.2}$ erg s^{-1} (calculated using the Hα/Hβ emission-line flux ratios from Mullaney et al. 2013 and following Calzetti et al. 2000). Additionally, we emphasize that all of our targets are classified as 'radio quiet' in the νL_ν(1.4 GHz)-$L_{\text{[O III]}}$ plane (Xu, Livio & Baum 1999; Zakamska et al. 2004) which make up the majority of the luminous type 2 AGN population (i.e. ≈90 per cent based on the sample in Zakamska et al. 2004). Furthermore, considering all galaxies at low redshift (i.e. $0.0 < z < 0.5$), the radio luminosities of our targets [i.e. $L_{1.4\,\text{GHz}} = (< 0.8 - 25) \times 10^{23}$ W Hz^{-1}] are known to be common with a space density of ≈10^{-4} Mpc^{-3} and ≈10^{-5} Mpc^{-3} for sources with $L_{1.4\,\text{GHz}} = 10^{23}$ and 10^{24} W Hz^{-1}, respectively (Simpson et al. 2012).

The key advantage of selecting our sources from a large parent sample of AGN is that we can quantitatively define how representative our targets are. In Fig. 2 we show histograms for the FWHM of the broad [O III] emission-line components for both the parent sample and our targets. Considering all of the type 2 AGN from Mullaney et al. (2013) with $z < 0.2$ and with an [O III] luminosity, $L_{\text{[O III]}} > 5 \times 10^{41}$ erg s^{-1} (i.e. to match our selection criteria), we find that 45 ± 3 per cent (246 out of 546 sources and assuming $\sqrt{N}$ errors) have a luminous [O III] component with FWHM[B] > 700 km s^{-1} (Fig. 2). This indicates that roughly half of luminous type 2 AGN have a luminous broad component to their [O III] emission-line profiles and demonstrates that our targets do not represent a rare subpopulation. Additionally, this fraction can be considered a lower limit, as the fraction of sources that host weaker broad components will be considerably higher. In Fig. 2 we also show histograms of the radio luminosities of our targets and the type 2 AGN in the parent sample that have luminous and broad [O III] emission-line components. Our targets cover a similar range in radio luminosities to those in the parent sample further demonstrating that our targets are representative of the parent population.

Table 2. Target properties.

Name	log[$L_{[O\,III]}$] (erg s^{-1})	log[$L_{H\beta}$] (erg s^{-1})	$S_{1.4}$ (mJy)	log[$L_{1.4}$] (W Hz^{-1})	θ_{FIRST}	PA$_{1.4}$/$R_{1.4}$ °/arcsec	log[$L_{IR,\,SF}$] (erg s^{-1})	SFR (M$_\odot$ yr^{-1})	log[L_{AGN}] (erg s^{-1})	q_{IR}
(1)	(2)	(3)	(4)	(5)	(6)	(7)	(8)	(9)	(10)	(11)
J0945+1737	42.83	41.80	44.5[4]	24.3	1.072[3]	112°/2.9	$45.5^{+0.1}_{-0.1}$	81^{+7}_{-25}	$45.5^{+0.2}_{-0.1}$	$1.8^{+0.1}_{-0.1}$
J0958+1439	42.60	41.49	10.4[4]	23.5	1.006[9]	–	$45.1^{+0.1}_{-0.1}$	36^{+12}_{-11}	$45.0^{+0.3}_{-0.3}$	$2.2^{+0.1}_{-0.1}$
J1000+1242	42.80	41.84	31.8[4]	24.2	1.111[4]	158°/3.3	$45.0^{+0.3}_{-0.2}$	29^{+18}_{-16}	$45.7^{+0.1}_{-0.1}$	$1.3^{+0.2}_{-0.2}$
J1010+1413	43.21	42.15	8.8[5]	24.0	1.044[13]	–	$45.7^{+0.2}_{-0.1}$	122^{+60}_{-32}	$46.0^{+0.2}_{-0.1}$	$2.3^{+0.2}_{-0.2}$
J1010+0612	42.30	41.48	99.3[1.3]	24.4	1.038[3]	–	$44.9^{+0.1}_{-0.1}$	23^{+4}_{-7}	$45.6^{+0.1}_{-0.1}$	$1.1^{+0.1}_{-0.1}$
J1100+0846	42.82	41.77	61.3[3]	24.2	1.0230[12]	–	<46.1	<365	$46.0^{+0.1}_{-0.1}$	<2.5
J1125+1239	42.06	40.94	1.7[5]	23.1	0.96[6]	–	<45.4	<66	$45.2^{+0.1}_{-0.2}$	<2.9
J1130+1301	42.03	40.88	1.7[4]	22.9	1.07[7]	122°/5.1†	$44.8^{+0.2}_{-0.2}$	18^{+7}_{-7}	$45.1^{+0.1}_{-0.1}$	$2.5^{+0.2}_{-0.2}$
J1216+1417	41.93	–	5.1[4]	22.9	1.07[2]	97°/2.7†	<44.6	<10	$45.3^{+0.1}_{-0.1}$	<2.1
J1316+1753	42.87	41.81	11.4[4]	23.8	1.04[1]	–	<45.5	<77	$45.4^{+0.1}_{-0.1}$	<2.2
J1338+1503	42.64	–	2.4[4]	23.3	1.06[5]	–	$45.5^{+0.1}_{-0.1}$	81^{+13}_{-13}	$45.2^{+0.3}_{-0.1}$	$2.7^{+0.2}_{-0.1}$
J1339+1425	41.95	40.84	<3.0	<23.2	–	–	<44.9	<23	$44.3^{+0.1}_{-0.1}$	–
J1355+1300	42.09	41.13	3.0[5]★	23.2	–	–	<45.4	<62	$45.7^{+0.1}_{-0.1}$	<2.7
J1356+1026	42.95	41.99	59.6[4]	24.4	1.014[2]	–	$45.4^{+0.1}_{-0.1}$	63^{+7}_{-17}	$45.1^{+0.3}_{-0.2}$	$1.6^{+0.1}_{-0.1}$
J1430+1339	42.72	41.88	26.4[4]	23.7	1.400[9]	77°/7.8	$44.4^{+0.2}_{-0.2}$	7^{+3}_{-3}	$45.3^{+0.1}_{-0.1}$	$1.3^{+0.2}_{-0.1}$
J1504+0151	42.20	–	3.0[4]	23.4	1.06[4]	–	$45.2^{+0.1}_{-0.1}$	44^{+10}_{-10}	$45.2^{+0.2}_{-0.2}$	$2.4^{+0.2}_{-0.1}$

Notes. Details of our IFU targets that we observed with GMOS. (1) Object name; (2)–(3) Total [O III] λ5007 and Hβ luminosities derived in this work, uncertainties are typically 15 per cent; (4) 1.4 GHz flux densities obtained from the FIRST survey (Becker, White & Helfand 1995) and uncertainties that are defined as 3 × the RMS noise of the radio map at the source position; (5) Rest-frame radio luminosities using a spectral index of $\alpha = 0.7$ and assuming $S_\nu \propto \nu^{-\alpha}$ (we note that a range of $\alpha = 0.2$–1.5 introduces an spread of $\lesssim \pm 0.1$ dex on the radio luminosity); (6) Radio morphology parameter, where sources with $\theta > 1.06$ are classified as extended in the 1.4 GHz FIRST data (see Section 2.4); (7) The deconvolved PA and major-axis radius from the FIRST survey for the radio-extended sources; (8)–(10) Infrared luminosities from star formation, SFRs and bolometric AGN luminosities derived from our SED analyses (see Section 2.4); (11) The q_{IR} ('radio excess') parameter for each source, where sources with $q_{IR} \leq 1.8$ are classified as 'radio excess' (see Section 2.4). ★The 1.4 GHz flux density for SDSS 1355+1300 is taken from the NVSS survey (Condon et al. 1998). †The uncertainty on θ is high and therefore these sources may not be truly extended in their FIRST images.
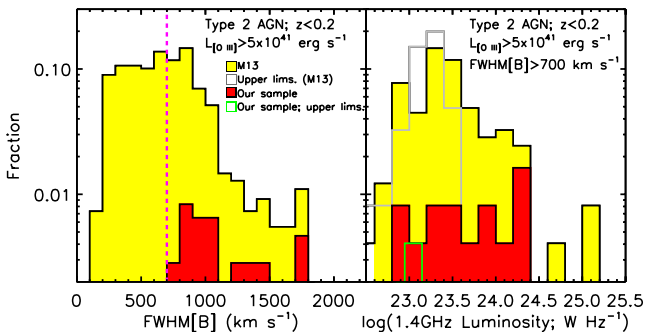
Figure 2. Histograms demonstrating how representative our IFU targets are of the overall luminous ($L_{[O\,III]} > 5 \times 10^{41}$ erg s^{-1}) type 2 AGN population in the redshift range $z < 0.2$. Left: histogram of the FWHM of the broadest, luminous [O III] component (FWHM[B]; see Fig. 1) from (Mullaney et al. 2013, M13). The filled red histogram represents the sources selected for this work and yellow represents the parent sample. The vertical dashed line shows our selection criteria of FWHM[B] > 700 km s^{-1}. Right: histogram of radio luminosity for the sources with FWHM[B] > 700 km s^{-1} from the parent sample (yellow; Mullaney et al. 2013) and our IFU targets (red; Table 2). The grey and green empty histograms represent the sources with upper limits from the parent sample and our IFU targets, respectively. Our targets are selected from the 45±3 per cent of luminous type 2 AGN in this redshift range have luminous broad [O III] emission-line components and their radio luminosities are representative of the parent population (see Section 2.1).

2.2 GMOS (South) observations and data reduction

The observations of our targets were performed using GMOS (South; Allington-Smith et al. 2002) in IFU mode. The GMOS IFU uses a lenslet array to slice the focal plane into several small components which are each coupled to a fibre. We made use of the one-slit mode with the B1200 grating to obtain the required wavelength coverage to observe the [O III] $\lambda\lambda$4959, 4007 and Hβ emission-lines for all our targets. In this mode the IFU consists of 25×20 lenslets sampling a 5 arcsec × 3.5 arcsec field of view. The GMOS IFU also has a dedicated set of 250 lenslets to simultaneously observe the sky ≈1 arcmin away from the target field of view. We determined the instrumental dispersion for the observations of each source ($\Delta v \approx 50$–60 km s^{-1}, with uncertainties $\lesssim$5 km s^{-1}) by measuring the widths of several skylines close to the observed wavelengths of the emission lines. The emission-line profiles we measure are typically non-Gaussian and the non-parametric line widths we quote (see Section 3.1) are very large ($\gtrsim$500 km s^{-1}); therefore, we do not correct for this instrumental broadening. This will result in the quoted line-width measurements being broadened by $\lesssim$2 per cent.

The observations were undertaken during two observing programmes: GS-2010A-Q-8 (PI: Mullaney) taken between 2010 February 09 and March 19, and GS-2012A-Q-21 (PI: Harrison) taken between 2012 February 16 and June 26. For the observations in the 2012A run, that covered the fainter targets, the on-source exposures consisted of 6 × 1500 s while for the 2010A run, that covered the brighter targets, the exposure times consisted of 4 × 1300 s. Table 1 indicates during which run each target was observed. The

Table 3. Infrared photometric data.

Name	W1 (3.4 μm)	W2 (4.6 μm)	W3 (12 μm)	W4 (22 μm)	*IRAS* 12 μm	*IRAS* 25 μm	*IRAS* 60 μm	*IRAS* 100 μm
J0945+1737	1.9 ± 0.6	6.0 ± 1.8	53 ± 16	310 ± 90	<127	440 ± 70	890 ± 60	570 ± 130
J0958+1439†	2.0 ± 0.6	3.8 ± 1.1	30 ± 9	130 ± 40	<250	<400	470 ± 140	<3000
J1000+1242	3.3 ± 1.0	7 ± 2	49 ± 15	220 ± 70	<118	<372	280 ± 70	<428
J1010+1413	1.8 ± 0.6	5.7 ± 1.7	56 ± 17	250 ± 70	<122	270 ± 50	470 ± 40	<625
J1010+0612	11 ± 3	17 ± 5	64 ± 19	290 ± 90	110 ± 30	290 ± 60	520 ± 50	590 ± 130
J1100+0846††	15 ± 5	34 ± 10	180 ± 50	540 ± 160	–	–	–	–
J1125+1239	1.0 ± 0.3	1.4 ± 0.4	8 ± 2	29 ± 9	<250	<400	<300	<3000
J1130+1301*	2.8 ± 0.8	3.6 ± 1.1	12 ± 4	45 ± 14	<114	<186	180 ± 50	<619
J1216+1417	5.9 ± 1.8	13 ± 4	42 ± 13	150 ± 50	<105	<400	<300	<620
J1316+1753	2.0 ± 0.6	3.2 ± 1.0	19 ± 6	90 ± 30	<250	<400	<300	<3000
J1338+1503	1.2 ± 0.4	2.5 ± 0.8	17 ± 5	80 ± 30	<134	<126	340 ± 50	<583
J1339+1425	0.5 ± 0.2	0.5 ± 0.1	1.1 ± 0.4	6 ± 2	<250	<400	<300	<3000
J1355+1300	7 ± 2	15 ± 4	40 ± 13	80 ± 20	<250	<400	<300	<3000
J1356+1026	2.2 ± 0.7	4.6 ± 1.4	27 ± 8	190 ± 60	<58	210 ± 50	800 ± 90	600 ± 150
J1430+1339	7 ± 2	11 ± 3	40 ± 12	180 ± 50	<105	190 ± 30	260 ± 40	<605
J1504+0151	2.0 ± 0.6	2.8 ± 0.8	10 ± 3	30 ± 9	<108	<93	210 ± 40	<508

Notes: The mid-infrared–far-infrared photometric flux densities, uncertainties and upper limits for the targets in our sample (in units of mJy) which are used in our SED analysis (these photometric data are shown in Fig. 3). These were obtained from *WISE* and *IRAS* all-sky catalogues (Moshir, Kopman & Conrow 1992; Wright et al. 2010; see Section 2.4 for details). The first *WISE* band (W1) falls outside of the wavelength range of our templates, therefore these flux densities are not included in the SED fitting procedure. †The *IRAS* fluxes for J0958+1439 are from SCANPI (http://irsa.ipac.caltech.edu/applications/Scanpi); ††J1100+0846 was not covered by *IRAS* observations; *J1130+1301 did not have an entry in the *IRAS* faint source catalogue; however, inspection of the images indicates that it is detected and therefore we obtained the fluxes from the *IRAS* reject catalogue.

observations were performed with *V* band seeing of ≲ 0.8 arcsec (typically ≈0.7 arcsec, from measurements of the acquisition images taken before each IFU observation).

We reduced the data using the standard Gemini IRAF GMOS pipeline to perform wavelength calibration and flat fielding and we used a dedicated set of IDL routines to perform sky subtraction, cosmic ray removal and cube construction. We did not resample the pixels and therefore the pixel scale of the final cubes is 0.17 arcsec × 0.2 arcsec. To find spatial centroids for the individual data cubes, emission-line free continuum images from each exposure were produced that were then spatially aligned and co-added to create the final mosaics, using a median stack with a 3σ clipping threshold to remove the remaining cosmetic defects and cosmic rays. Flux calibration for each target was performed in two stages. Stage one involved reducing standard star observations in an identical manner to the targets and consequently obtaining the instrumental response using IRAF routines from the ONEDSPEC package. Stage two used the SDSS spectra to find the absolute flux calibration for each of the objects. This was achieved by fitting a low-order polynomial to the emission-line free SDSS spectrum and also an emission-line free spectrum extracted from our IFU data cubes over the same spatial region as covered by the SDSS fibres (i.e. ≈3 arcsec diameter). We verified that the equivalent widths of the emission lines were consistent between these two spectra and then used the ratio between these fits to apply the flux calibration to each of the data cubes. We estimate a conservative uncertainty of 15 per cent on the absolute flux calibration using this process (see Abazajian et al. 2009; Liu et al. 2013a).

2.3 Aligning the IFU data to SDSS images

As part of our analyses we compare the location of the kinematic features we observe in our IFU data, to the host galaxy morphologies based upon three-colour (*g*, *r*, *i*) SDSS images (Section 4.2). We aligned the SDSS three-colour images to our IFU data by match-

ing the surface brightness peak in the *g*-band SDSS images to the surface brightness peak of images constructed from our IFU data cubes, collapsed around ≈5000 Å. We then rotated the SDSS images to match the orientation of our IFU data cubes. We note that we only use these images for qualitative descriptions of the galaxy morphology with respect to our IFU data and therefore we do not require a more accurate alignment process.

2.4 SFRs, AGN luminosities and the origin of the radio emission

To thoroughly interpret our results we investigate the properties of the AGN and host galaxies of our targets in more detail (i.e. we measure SFRs and AGN luminosities and explore the origin of the radio emission). To obtain the bolometric AGN luminosities and SFRs of our targets (see Table 2) we performed mid-infrared to far-infrared SED fitting to archival photometric data that is available for our targets (described below). Our procedure decomposes the emission from AGN activity and star formation, so that we do not need to make any assumptions about the relative contribution from these two processes. At the end of this section, we also briefly investigate the possible presence of radio AGN activity (i.e. radio cores or radio jets) in our targets by combining the results of our SED fitting with archival radio data.

For our SED fitting, we obtained mid-infrared to far-infrared photometric flux densities, uncertainties and upper limits (over 3–100 μm; see Table 3) from (1) the *Wide-field Infrared Survey Explorer* (*WISE*) all-sky survey (Wright et al. 2010) using the closest source to the SDSS position (all are <0.6 arcsec) and (2) the *Infrared Astronomical Satellite* (*IRAS*; Neugebauer et al. 1984) faint source catalogue (Moshir et al. 1992) with a matching radius of ≤30 arcsec.[1] We added in quadrature 30 per cent of the measured

---

[1] We verified these matches by following the log likelihood method of matching *IRAS* to *WISE* counterparts outlined in Wang et al. (2014).
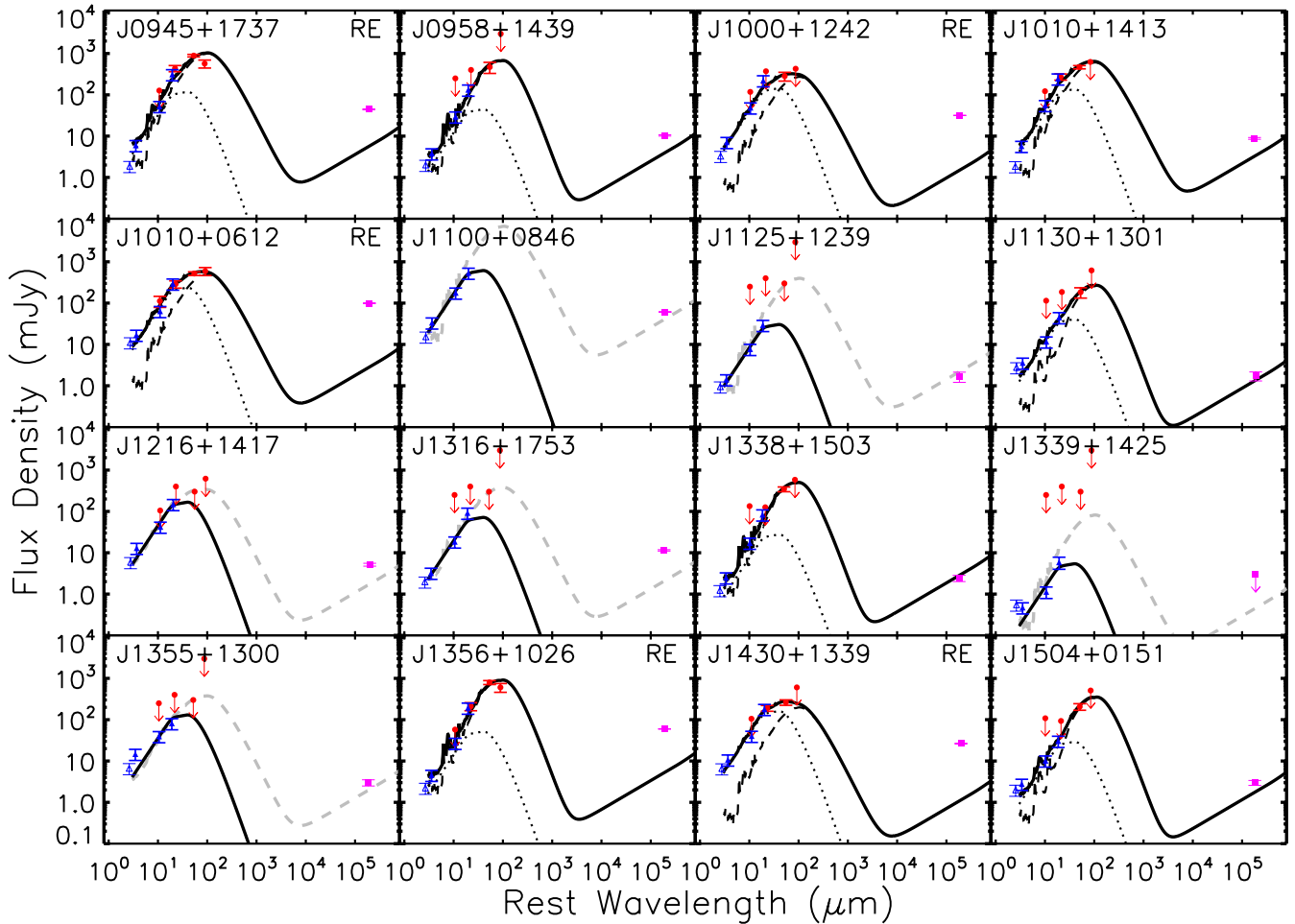
Figure 3. The infrared SEDs for each target in our sample. The flux densities used in the fitting procedure are shown as blue filled triangles (*WISE* data) and red filled circles (*IRAS* data; photometric data in Table 3). The first *WISE* band (at 3.4 μm) falls outside of the wavelength range of our templates and is shown with an empty symbol. Also shown are the overall best-fitting SEDs: the total SEDs are shown as solid curves, the AGN templates are shown as dotted curves and the starburst templates as dashed curves. The grey dashed curves show the upper limits on the starburst templates for the sources that lack far-infrared data. Using these SED fits we obtain SFRs and AGN luminosities (see Section 2.4 and Table 2). We also plot the 1.4 GHz flux densities (square symbols) that are not included in the fitting but do illustrate that five of the sources have significant excess radio emission above that expected from star formation (indicated with 'RE' in the top right of their panels; see Section 2.4; Table 2).

flux densities to the quoted *WISE* uncertainties to account for calibration uncertainties in the *WISE* data (Wright et al. 2010) and the discrete nature of the SED templates used in our analysis (see below; also see Del Moro et al. 2013). For the sources that do not have *IRAS* flux density measurements (see Table 3) we estimated conservative maximum upper limits of 0.25, 0.4, 0.3 and 3 mJy for the 12, 25, 60, and 100 μm bands, respectively. One source (SDSS J1100+0846) falls into an area of the sky that was not observed by *IRAS* observations and we therefore cannot place photometric constraints on the *IRAS* bands for this source. The photometric data we used are shown in Fig. 3.

To perform the SED fitting we followed the procedure described in Mullaney et al. (2011) that simultaneously fits an empirically derived AGN model (parametrized in an analytical form) and empirically derived host galaxy templates to the infrared photometric data (Table 3). All of the sources in our sample are known to host an AGN (from optical spectroscopy) and additionally all but one of the sources are classified as an infrared AGN based upon the *WISE* colours (W2−W1 and W3−W2) by falling inside

the 'AGN wedge' defined in Mateos et al. (2012).[2] We therefore simultaneously fit these data with the five star-forming galaxy templates ('SB1'−'SB5') and the mean AGN model, originally defined in Mullaney et al. (2011) and extended to cover the wavelength range 3–10^5 μm, by Del Moro et al. (2013).[3] To derive the AGN

---

[2] SDSS J1339+1425 does not have *WISE* colours that place it inside the 'AGN wedge'; however, we still found that including an AGN template provided a better fit than any of the star-forming templates alone.

[3] We tested how much of an effect our limited range of templates have on our quoted results (Table 2) by: (1) re-fitting including an Arp 220 model SED and (2) allowing the second power-law slope of the AGN model to be a free parameter (i.e. α_2 in Mullaney et al. 2011). The first of these changes allows for a more extreme ULIRG-like SED that is not covered by our main SB templates. The second change allows for a very large range in intrinsic AGN SEDs, to account for the variations seen in AGN of different luminosities (see fig. 7 in Mullaney et al. 2011). When performing the SED fitting with these two additions we found that all the results were consistent within the errors of our quoted results (Table 2) with only two minor exceptions:

luminosities and SFRs (Table 2) we use the star-forming template plus AGN template combination that gives the lowest overall χ^2 value, rejecting all fits that lie above the photometric upper limits (given in Table 3; see Fig. 3). For the sources where we have no detections in the far-infrared bands (i.e. the *IRAS* bands), we are unable to measure reliable SFRs and we therefore calculate conservative upper limits by increasing the normalization of the star-forming templates until either the photometric upper limits were reached or the solution was 3σ above one of the photometric data points.

We calculated the SFRs for each source (Table 2) by measuring the infrared luminosities of the star formation components from the best-fitting SED solutions ($L_{\rm IR, SF}$; integrated over 8–1000 μm) and using the relationship of Kennicutt (1998; corrected to a Chabrier initial mass function, IMF, by dividing by a factor of 1.7; Chabrier 2003). To determine the bolometric AGN luminosities for each source (Table 2), we first calculated the AGN continuum luminosity at 6 μm from the best-fitting SED solution and converted this to an AGN bolometric luminosity using a correction factor of $\times 8$ (Richards et al. 2006; see Table 2). The conservative upper and lower bounds on both the SFRs and AGN luminosities are derived from summing in quadrature the range in solutions from the different star formation templates (only those which did not exceed the upper limits) and the formal uncertainties from the best-fitting solution. We emphasize that our method decomposes the emission due to an AGN and star formation, therefore removing the need to assume the relative contributions from these two processes. Furthermore, this procedure produces consistent SFRs and AGN luminosities with those derived from mid-infrared spectra where available (see Appendix A and Footnote 13; also see Del Moro et al. 2013).

The bolometric AGN luminosities for our targets span $L_{\rm AGN} = (0.2 - 10) \times 10^{45}\,{\rm erg\,s^{-1}}$ (with a median $L_{\rm AGN} = 2 \times 10^{45}\,{\rm erg\,s^{-1}}$) and therefore cover the classical 'quasar' threshold of $L_{\rm AGN} = 10^{45}\,{\rm erg\,s^{-1}}$. We note that these mid-infrared derived AGN luminosities are a factor of ≈ 1–20 lower than those that would be predicted using the [O III] luminosity and the relationship of Heckman et al. (2004; i.e. $L_{\rm AGN} = 3500 L_{\rm [O III]}$). However, this is consistent with other studies of luminous ($L_{\rm [O III]} \gtrsim 10^{42}\,{\rm erg\,s^{-1}}$) type 2 AGN, at similar redshifts, that show that $L_{\rm [O III]}$ is not linearly correlated with the nuclear luminosity and can over predict the AGN luminosity by an order of magnitude or more (Hainline et al. 2013; Schirmer et al. 2013).

Of the 16 sources in our sample, 8 have far-infrared luminosities that classify them as luminous infrared galaxies (LIRGs; $L_{\rm IR, SF} = 10^{11}$–$10^{12}\,{\rm L_\odot}$) and 1 as an ultraluminous infrared galaxy (ULIRG: $L_{\rm IR, SF} > 10^{12}\,{\rm L_\odot}$). Of the remaining 7 sources, 6 of them have upper limits on their far-infrared luminosities which are less than or consistent with the luminosity of LIRGs (see Table 2).[4] These infrared luminosities correspond to SFRs of $\lesssim [7$–$120]\,{\rm M_\odot\,yr^{-1}}$ and are typical for AGN of these luminosities at these redshifts (e.g. Zakamska et al. 2008; Mullaney et al. 2010; Rosario et al. 2012).

Finally, we investigate the origin of the radio emission from our targets. We plot the 1.4 GHz radio flux densities (given in Table 2) on the SEDs shown in Fig. 3. We identify if there is radio emission

significantly above that expected from their ongoing star formation (e.g. Helou, Soifer & Rowan-Robinson 1985; Condon, Anderson & Broderick 1995), that may indicate radio emission due to an AGN either in form of a radio core or radio jets (e.g. see Del Moro et al. 2013, and references therein) or due to shocks (e.g. Zakamska & Greene 2014). To do this we use the definition given by Ivison et al. (2010; see also Helou et al. 1985), calculating the ratio between the far-infrared and radio emission ($q_{\rm IR}$) as

$$q_{\rm IR} = \log\left[\frac{S_{\rm IR}/3.75 \times 10^{12}\,{\rm W\,m^{-2}}}{S_{1.4}/{\rm W\,m^{-2}\,Hz^{-1}}}\right], \qquad (1)$$

where $S_{\rm IR}$ is the rest-frame far-infrared (8–1000 μm) flux and $S_{1.4}$ is the rest-frame 1.4 GHz flux density assuming, $S_\nu \propto \nu^{-\alpha}$, with a radio spectral index of $\alpha = 0.7$. We give the value of $q_{\rm IR}$ for each source in our sample in Table 2. The quoted uncertainties combine the uncertainties on $S_{1.4}$, $S_{\rm IR}$ and a range in the unknown radio spectral indices (we use $\alpha = 0.2$–1.5). Star-forming galaxies have $q_{\rm IR} \approx 2.4$ and we define 'radio excess' sources as those with $q_{\rm IR} \le 1.8$, i.e. $\gtrsim 2.5\sigma$ away from the peak seen in the star-forming galaxies (Ivison et al. 2010; see also Del Moro et al. 2013 who use a similar definition). Using this definition we identify five of our targets as being radio excess and five sources that are classified as radio normal (see Table 2 and Fig. 3); however, we cannot rule out low-level radio emission above that expected from star formation in these targets as it can be difficult to identify using this method, especially in systems with high SFRs (e.g. Del Moro et al. 2013). The remaining six sources have upper limits on their $S_{\rm IR}$ values which results in upper limits on their $q_{\rm IR}$ values that are consistent with them being either radio normal or radio excess sources.

Based on FIRST (Becker et al. 1995) and NVSS (Condon et al. 1998) images only one of our sources (J1430+1339) shows clear evidence for luminous extended radio structures on scales >5 arcsec (see Table 2 and Appendix A). Therefore, we follow the method of Kimball & Ivezić (2008) to search for evidence of extended radio structures (on ≈ 2–5 arcsec scales) that compares the peak and integrated 1.4 GHz FIRST flux densities ($F_{\rm peak}$ and $F_{\rm int}$, respectively). They define the parameter $\theta = (F_{\rm int}/F_{\rm peak})^{0.5}$ and any source with $\theta > 1.06$ is classed as spatially resolved. We provide θ for all of our targets with FIRST detections in Table 2. For the five sources with $\theta > 1.06$, i.e. those that pass the criteria to be 'resolved', we also provide the position angle and radius of the de-convolved major axis provided by FIRST. Of these five sources, two have very low 1.4 GHz flux densities and therefore the uncertainty on θ is high. The other three have stronger evidence for being spatially resolved and are also 'radio excess' sources; therefore, they are the strongest candidates for having radio jets on ≈ 3–8 arcsec scales (i.e. ≈ 7–12 kpc; Table 2), although shocks due to outflows is another possible explanation for this excess radio emission (Zakamska & Greene 2014). High-resolution radio imaging will be instrumental in determining the origin and morphology of the radio emission in the whole sample.

3 VELOCITY DEFINITIONS AND SPATIALLY RESOLVED KINEMATICS

3.1 Non-parametric velocity definitions

We are interested in the spatially resolved kinematics of the [O III] $\lambda\lambda 4959, 5007$ and Hβ emission lines for the 16 type 2 AGN we observed with the GMOS IFU. The combination of these emission-line species allows us to measure emission-line region sizes (Section 4.1), spatially resolve the ionized gas kinematics (Section 4.2)

---

(1) the SFR for J1430+1339 had an upper limit of $<2\,{\rm M_\odot\,yr^{-1}}$ and (2) the AGN luminosity of J1504+0151 was $\log[L_{\rm AGN}] = 45.4^{+0.1}_{-0.3}\,{\rm erg\,s^{-1}}$. We therefore conclude that our primary choice of templates is sufficient for this work.

[4] The remaining source, SDSS J1100+0846, which is not covered by *IRAS* and therefore has poor FIR constraints, has an upper limit consistent with a ULIRG.
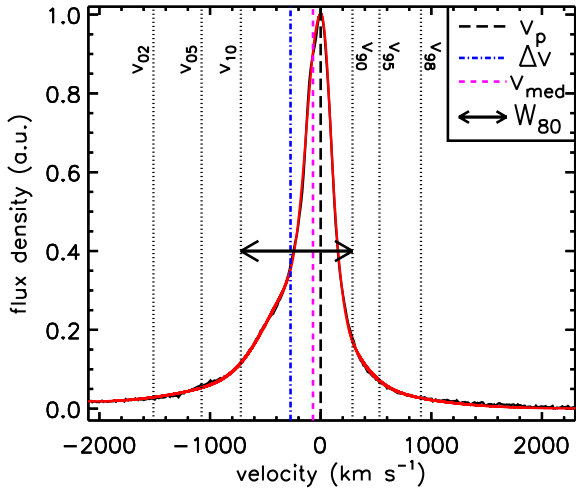
Figure 4. Illustration of the different non-parametric velocity definitions used in this work which are described in Section 3.1. We show an example [O III] λ5007 emission-line profile from our sample (black curve) and our fit to this profile (red curve). The vertical dotted lines show different percentiles to the flux contained in the overall emission-line profile (from left to right: 2nd; 5th; 10th; 90th; 95th and 98th). The long-dashed line shows the velocity of the peak flux density (v_p). The vertical short-dashed line shows the median velocity (v_{med}) and the dot–dashed line shows the velocity offset of the underlying broad wings (Δv; see Section 3.1). The arrow indicates the line width that contains 80 per cent of the flux (W_{80}).

and calculate ionized gas masses (Section 4.3) for our targets. The emission-line profiles in type 2 AGN are often found to be complex, consisting of multiple narrow and broad components (e.g. Veilleux 1991; Greene et al. 2011; Villar-Martín et al. 2011b), which is also the case for our sample (Fig. 5 and Figs A1–A15). Due to the complexity of the emission-line profiles we opted to use non-parametric definitions to characterize their widths and velocities within each pixel of the IFU data. We used an approach that (1) is consistent for all of the targets in the sample; (2) allows us to de-couple galaxy dynamics, merger remnants and outflow features and (3) provides results that are directly comparable to observations in the literature. The definitions that we have used throughout, for describing both the galaxy-integrated emission-line profiles and the spatially resolved kinematics, are described below and are illustrated in Fig. 4.

(i) The peak velocity (v_p) is the velocity of the peak flux density in the overall [O III] λ5007 emission-line profile. For our targets, this traces the brightest narrow emission-line component (i.e. those with FWHM $\lesssim 500$ km s^{-1}).

(ii) The line width, W_{80}, is the velocity width of the line that contains 80 per cent of the emission-line flux such that $W_{80} = v_{90} - v_{10}$, where v_{10} and v_{90} are the velocities at the 10th and 90th percentiles, respectively (Fig. 4). For a single Gaussian profile this is approximately the FWHM.

(iii) To measure the velocity offset of the broad underlying wings we define the velocity offset, Δv, that is measured as $\Delta v = (v_{05} + v_{95})/2$, where v_{05} and v_{95} are the velocities at the 5th and 95th percentiles of the overall emission-line profiles, respectively (Fig. 4). For a profile that is well characterized by a single narrow Gaussian component and a luminous broad Gaussian component, Δv is the velocity offset of the broad component. For a single Gaussian component $\Delta v = 0$.

(iv) To enable us to compare to previous work we also measured v_{02} and v_{98}, which are the 2nd and 98th percentiles of the flux contained in the overall emission-line profiles (as used in Rupke & Veilleux 2013)[5] and can be considered the 'maximum' projected velocity of the gas.

(v) Finally, we measured the median velocity (v_{med}; Fig. 4) of the overall emission-line profile so that we can compare to the type 2 AGN observed in Liu et al. (2013b). We find that v_{med} is likely to be dominated by galaxy kinematics in many cases (i.e. galaxy rotation or mergers; see Section 4.2.2) and should be used with care if interpreting outflow kinematics.

We emphasize that these definitions are used to enable us to consistently compare all of the targets in our sample as well as compare to observations in the literature; however, for a few individual cases some care should be taken when interpreting these measurements due to the uniqueness and complexity of the emission-line profiles. For this reason we discuss the details of kinematics of individual sources in Appendix A.

3.2 Emission-line profile fitting procedure

As several of the velocity definitions outlined above and illustrated in Fig. 4 are measured from the broad wings of the emission-line profiles they are subject to the influence of noise in the spectra, especially in the lower surface brightness regions of our IFU observations. To circumvent this issue, we characterize each emission-line profile using a combination of multiple Gaussian components. We note that we do not draw any physical meaning from the individual Gaussian components, they are only used to characterize the emission-line profiles. Below, we describe the emission-line profile fitting procedure that we use throughout for fitting the galaxy-integrated spectra and also the spectra used to produce the spatially resolved maps and velocity profiles described in Section 3.3.

Initially, we isolated the [O III] λλ4959, 5007 emission-line doublet from the underlying continuum by linearly interpolating each spectrum between line-free regions close to the emission lines, a commonly used method for type 2 AGN (e.g. Husemann et al. 2013; Liu et al. 2013b). The emission-line doublet was then fitted with a minimizing-χ^2 method, using the IDL routine MPFIT (Markwardt 2009) with Gaussian components. For every Gaussian component we simultaneously fit the [O III] λ5007 and [O III] λ4959 emission lines using the same line width, a fixed wavelength separation and the intensity ratio was fixed at [O III] λ4959/[O III] λ5007 = 0.33 (e.g. Dimitrijević et al. 2007). Initially we fit a single Gaussian component to the emission-line profile and consequently additional Gaussian components were added to the overall fit (up to a maximum of six components) until the important values for our study (i.e. Δv, W_{80} and v_p; see Fig. 4) became stable within ≤ 20 per cent, i.e. the addition or removal of a Gaussian component does not change these values significantly. We only fitted more than one Gaussian component if the emission line was detected above a signal-to-noise ratio (S/N) threshold of ≈ 30, with this threshold being motivated by visually inspecting the fits and the reduced

---

[5] We note that Rupke & Veilleux (2013) fit a broad and narrow component to the emission lines and then define v_{98} for the broad component only. As a result their values are likely to be higher than our values that we defined from the *overall* emission-line profile so as not to make any assumptions on the kinematic structure of the emission lines (i.e. the number of distinct velocity components).
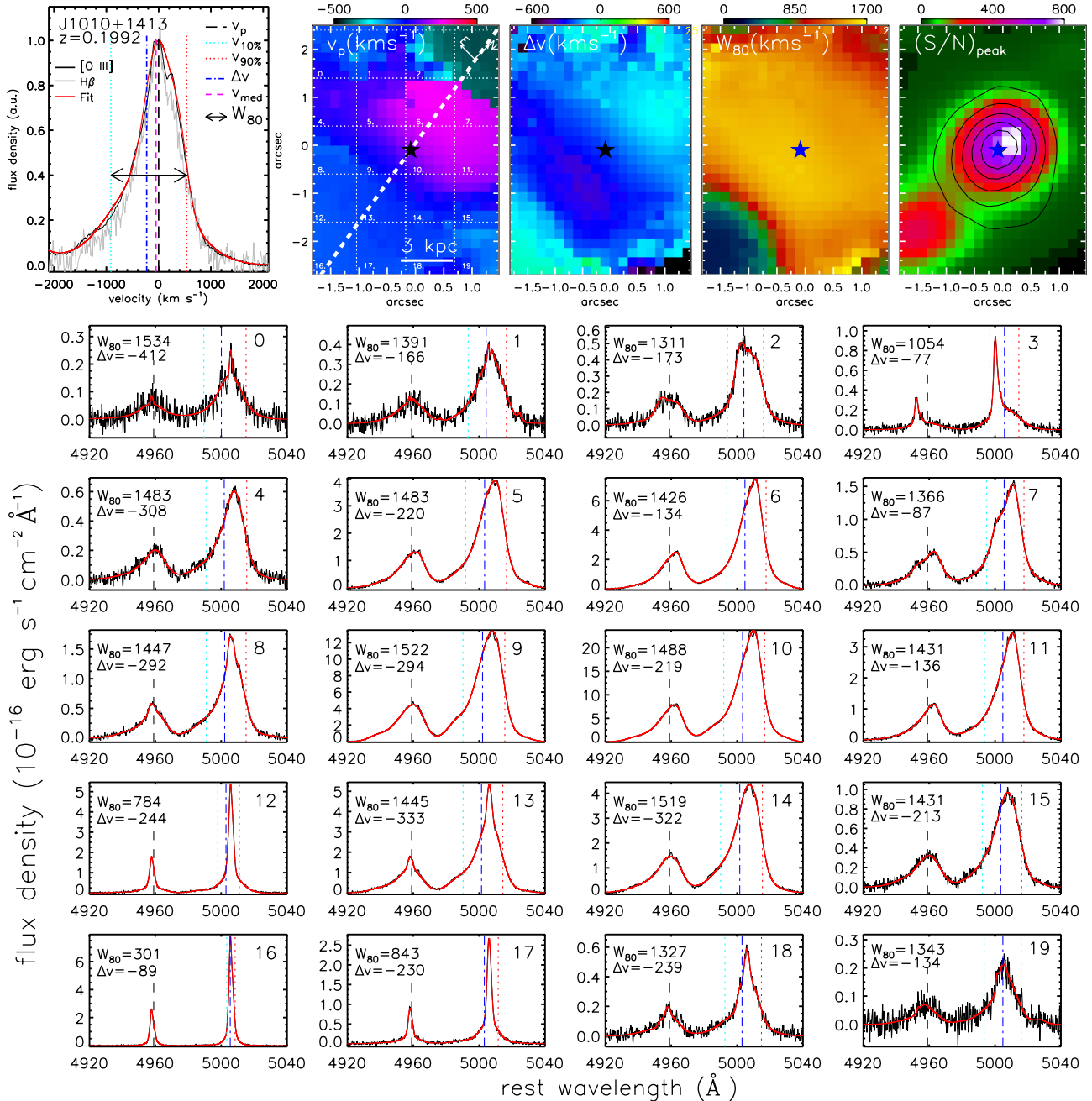
Figure 5. Our IFU data for an example object in our sample (SDSS J1010+1413). The equivalent plots for the rest of the sample can be found in Appendix A. Upper panels from left to right: panel 1: galaxy-integrated [O III] λ5007 emission-line profile (black curve) extracted from the full field of view of the IFU. Zero velocity corresponds to the redshift given in Table 2 and the spectrum has been normalized to the peak flux density. The solid red curves indicate the best fit to the emission-line profile. The vertical dashed and dotted lines correspond to the non-parametric velocity definitions described in Fig. 4 and Section 3.1. The Hβ emission-line profile is shown in grey. Panel 2: the velocity of the [O III] emission-line peak (v_p) at each pixel. The solid bars indicate 3 kpc in spatial extent and the dashed line indicates the kinematic 'major axis' as defined in Section 3.3. The dotted lines and numbers indicate the spatial regions from which we extracted the spectra shown in the lower panels. Panel 3: the value of the velocity offset of the broad emission-line wings (Δv) at each pixel. Panel 4: the value of the emission-line width (W_{80}) at each pixel. Panel 5: S/N of the peak flux density of the [O III] emission-line profile at each pixel. The contours show the morphology of line-free continuum emission (collapsed around a ≈200 Å wavelength region centred on [O III] λ5007) indicated by lines of constant S/N, starting at 15σ with increments of 10σ. The stars in each panel show the position of the peak of this continuum emission. Lower panels: continuum-subtracted spectra extracted from the individual spatial regions indicated in Panel 2. The definitions of the curves and lines are the same as in Panel 1 with the addition that the black vertical dashed line fixed at λ = 4959 Å that indicates the systemic wavelength for the [O III] λ4959 emission line.

χ^2 values (see below). For spectra below this S/N threshold, W_{80} cannot be well characterized and we are also unable to define Δv. We included appropriate constraints to the line widths to avoid fitting excessively broad components to the continuum or narrow

components to noise spikes (i.e. limited by the spectral resolution). We verified that our fitting procedure was effective across the whole field of view by visually inspecting the spectra and their best-fitting solutions extracted from 25 spatial regions for each object

individually (Fig. 5 and Figs A1–A15). An additional verification of the success of our fitting procedure was that, in all but one of the targets,[6] the median reduced χ^2 values of the fits to the individual pixels in the data cubes are between 1.0 and 1.8 with $\geq$60 per cent of the pixels having reduced χ^2 values between 0.8 and 2.5.

Using the overall fits to the emission-line profiles, we measure the non-parametric velocity definitions defined in Section 3.1 (see Fig. 4). Random errors on these quantities were calculated by taking the 1σ spread of values calculated from a 1000 random spectra that were generated using the final models plus Gaussian random noise (based on the standard deviation of the continuum). To obtain the final quoted uncertainties, we added these random errors in quadrature with an estimated systematic error that we calculated from the range in the velocity values derived from adding or removing a Gaussian component to the final emission-line models. We note that these uncertainties are extremely small ($\lesssim$10 per cent) in the high S/N spectra and therefore the uncertainties will be dominated by the physical interpretation of these values (see Section 4).

To enable us to measuring ionized gas masses (Section 4.3) we also measured the Hβ emission-line profiles and fluxes from our IFU data. To do this, we extract the Hβ emission-line profiles from the IFU data cubes in the same manner to that for [O III] λ4959, 5007 and show them in Fig. 5 and Figs A1–A15. We find that the overall shapes of the Hβ emission-line profiles are in excellent agreement with the [O III] emission-line profiles for all but three of our sources (the exceptions are SDSS J1216+1417; SDSS J1338+1503 and SDSS 1504+0151). This indicates that for the majority of the sources, the Hβ emission lines are not significantly affected by stellar absorption features (which is true for many AGN with luminous emission lines; Soto & Martin 2010; Harrison et al. 2012; Liu et al. 2013b) and this emission line traces the same kinematic components as the [O III] emission line (see also Rodríguez Zaurín et al. 2013). For these 13 sources we measure the Hβ emission-line fluxes by fitting the [O III] emission-line models (described above) to the data at the observed wavelength of the Hβ emission lines, allowing only the overall normalization to vary. The remaining three sources, which have different profiles for these two emission-line species, may have varying ionization states for different kinematic components and/or have higher levels of Hβ stellar absorption features that is certainly plausible given the stellar continua and absorption features observed in their optical spectra (see Appendix A). For this work, we wish to avoid using a variety of approaches for our targets; therefore, we choose to not use the Hβ emission lines in the analyses of these sources.

Due to the lack of clearly defined stellar absorption lines in the spectra across our targets, we define the systemic redshift from the velocity of the peak flux density in the [O III] λ5007 emission line (see Fig. 5). This choice of systemic redshift effectively traces the mean velocity of the narrow components in the emission-line profiles, which are often attributed to galaxy kinematics (e.g. Greene & Ho 2005; Harrison et al. 2012; Rupke & Veilleux 2013; also see Section 4.2.1); however, this might not always be the case and therefore places an uncertainty on our systemic redshift. For SDSS J0958+1439 and SDSS J1316+1753 where the overall emission-line profiles lack a clear single peak (see Figs A2 and A9) we take the flux weighted mean velocity of the narrow components (i.e. those with FWHM <500 km s^{-1}) used in the fit to the

galaxy-integrated spectrum (i.e. similar to the procedure used in Rodríguez Zaurín et al. 2013). Across the whole sample, the mean velocity offset between our systemic redshift and the SDSS redshift is -18 km s^{-1} with a scatter of 54 km s^{-1}. We note that any velocity *differences* that are measured (such as W_{80}) are unaffected by the choice in systemic redshift.

3.3 Velocity maps and velocity-distance profiles

We significantly detect [O III] emission to the edges of the IFU field of view in all 16 sources (i.e. over $\geq$10–20 kpc; see discussion in Section 4.1). These extended emission-line regions enable us to trace the ionized gas kinematics over these scales. In Fig. 5 we show example velocity maps of v_p, W_{80} and Δv (for the target J1010+1413) that were created by measuring these quantities across the field of view following the procedure outlined in Section 3.2 (see Figs A1–A15 for these maps for the other targets). The spectra used to calculate these values are from averaging over 3 × 3 pixels (i.e. ≈0.6 arcsec; comparable to the seeing of the observations) at the position of every pixel. At each position we measured the velocities from the fits to the [O III] emission-line profiles but only if it was detected in the spectra with a S/N $\geq$ 7. In Fig. 5 we also show the peak signal-to-noise ratio [(S/N)$_{peak}$] map which is the ratio of the peak flux density of the fitted [O III] emission-line profile to the noise in the spectrum at each pixel position. These maps are discussed in Section 4.

To further aid our analyses we also produced velocity profiles along two axes through the IFU data cubes for each source (shown in Fig. 6 and Figs A1–A15). We first defined a 'major axis' for each source based upon the velocity peak maps (v_p; e.g. Fig. 5). The positional angle (PA) of the 'major axis' for each source was chosen such that the velocity shear of the v_p map was the maximum. For a source where v_p traces galactic rotation this 'major axis' corresponds to the kinematic major axis of the galaxy (for a discussion see Section 4.2.1). The second axis was taken perpendicular to the 'major axis' (see e.g. Fig. 6). Using the PAs defined above we produced pseudo-longslit spectra with a slit width of five pixels (≈0.8 arcsec–1 arcsec). We obtained the spectra along each slit (from averaging over a length of 3 pixels) and calculated the velocity measurements outlined in Section 3.1. In these velocity profiles, we also plot the ratio of the [O III] to Hβ emission-line fluxes, plotting the 3σ lower limit on this ratio when Hβ is not detected above 3σ.

4 RESULTS

Using GMOS IFU data we study the spatially resolved properties of the [O III] $\lambda\lambda$4959, 5007 and Hβ emission lines of 16 luminous type 2 AGN (Table 2) chosen from our well-constrained parent sample (described in Section 2.1; see Figs 1 and 2). In Fig. 5 and Figs A1–A15 we show the spatially integrated [O III] λ5007 and Hβ emission-line profiles, the velocity maps and the peak [O III] S/N maps for all of the sources in our sample. In Fig. 6 and Figs A1–A15 we show SDSS images and velocity-distance profiles and in Table 4 we tabulate the values that we derive from the galaxy-integrated spectra, the emission-line images and the velocity maps. In the following sections we present our results of the sample as a whole, first presenting the sizes and morphologies of the emission-line regions (Section 4.1) before presenting the spatially resolved kinematics (Section 4.2). We give notes on the results from our IFU data for the individual sources in Appendix A.

---

[6] The source with a higher median reduced χ^2 = 3.5 is SDSS J1356+1026 that we attribute to the highly complex emission-line profile and exceptionally low noise (Fig. A13).
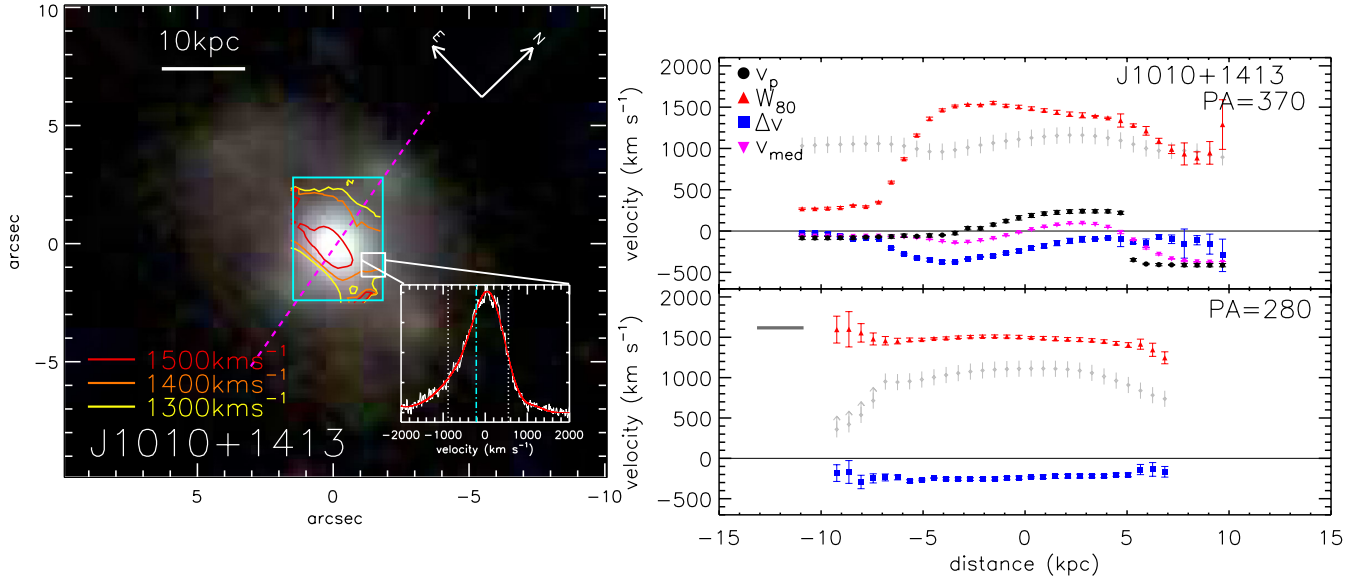
Figure 6. Our IFU data and SDSS image from an example object (J1010+1413) in our sample. The equivalent plots for the rest of the sample can be found in Appendix A. Left: three colour (*g*, *r*, *i*) SDSS image. The cyan box shows the field of view of our GMOS IFU observations. The contours show values of W_{80} and highlights the spatial distribution where the [O III] emission-line profiles are broadest (see Fig. 5). The dashed line shows the kinematic 'major axis' defined in Section 3.3. We also show an example [O III] emission-line profile extracted from the highlighted spatial region (white box; for curve and line definitions see Fig. 5). Right upper: [O III] velocity profiles (using the velocity definitions described in Section 3.1) along the kinematic 'major axis' indicated in the left-hand panel. Empty red triangles in Figs A1–A15 are where the S/N of the spectra is low and the emission-line widths cannot be well characterized (see Section 3.2). The grey diamonds indicate the flux ratio: $1000 \times \log$ ([O III]/Hβ). Right lower: velocity profiles taken perpendicular to the kinematic 'major axis' indicated in the left-hand panel. The solid horizontal bar indicates the typical seeing of the observations (i.e. 0.7 arcsec). For this source very broad emission-line profiles ($W_{80} \gtrsim 800\,\mathrm{km\,s^{-1}}$) with a velocity offset of $\Delta v = -300\,\mathrm{km\,s^{-1}}$ are found over the full extent of the field of view ($\approx 16\,\mathrm{kpc}$). Extended broad emission is found in all of the objects in our sample but with a variety of morphologies.

Table 4. Kinematic measurements and emission-line region sizes.

Name	$\langle W_{80} \rangle$ (km s^{-1})	$W_{80,\,\mathrm{max}}$ (km s^{-1})	$\langle \Delta v \rangle$ (km s^{-1})	$|\Delta v_{\mathrm{max}}|$ (km s^{-1})	$\langle v_{02} \rangle$ (km s^{-1})	$\Delta v_{\mathrm{med,\,max}}$ (km s^{-1})	Gal. kinematics	$R_{\mathrm{[O\,III]}}$ (kpc)	D_{600} (kpc)
(1)	(2)	(3)	(4)	(5)	(6)	(7)	(8)	(9)	(10)
J0945+1737	1009	1284	−273	284	−1511	138	I	2.7 ± 1.6	≥12
J0958+1439	815	904	−46	107	−866	190	R	2.6 ± 1.4	≥10
J1000+1242	795	873	−58	171	−761	311	R/I	4.3 ± 1.8	14
J1010+1413	1449	1525	−229	350	−1523	299	R/I	3.9 ± 2.3	≥16
J1010+0612	1280	1468	−95	216	−1267	138	R	1.6 ± 1.3	≥6
J1100+0846	1066	1367	−30	148	−1192	55	R	1.9 ± 1.3	≥10
J1125+1239	1285	1574	−265	424	−1547	73	F	2.9 ± 2.0	≥9
J1130+1301	778	849	149	173	−616	140	R	2.8 ± 1.7	8
J1216+1417	1228	1456	124	230	−1115	40	F	1.5 ± 1.1	≥6
J1316+1753	1127	1169	−191	326	−1216	500	R/I	3.1 ± 1.8	≥14
J1338+1503	890	1085	124	182	−813	145	R/I	3.5 ± 2.2	≥13
J1339+1425	672	724	147	178	−505	84	R	2.5 ± 1.7	6
J1355+1300	667	953	−184	277	−797	71	R	3.5 ± 1.8	≥6
J1356+1026	900	964	−215	544	−1049	523	I	3.1 ± 1.5	≥11
J1430+1339	822	1042	−152	268	−999	439	R/I	1.8 ± 1.1	≥9
J1504+0151	1184	1181	−495	520	−1739	149	R	2.9 ± 2.1	≥7

Notes. Velocity values and sizes derived from the galaxy-integrated spectra and velocity maps shown in Fig. 5 and Figs A1–A15 (see Section 3.1 and Fig. 4 for velocity definitions). (1) Object name; (2) value of the [O III] emission-line width, W_{80}, derived from the galaxy-integrated spectra; (3) maximum value of W_{80} from the spatially resolved maps (with a 95 per cent clipping threshold to remove spurious pixels); (4) velocity offset, Δv, derived from the galaxy-integrated spectrum; (5) absolute value of the maximum Δv in the spatially resolved maps (with 95 per cent clipping); (6) the value of maximum [O III] velocity, v_{02}, derived from the integrated spectrum; (7) the maximum velocity shear of the median velocity, v_{med}, from the velocity maps (with 95 per cent clipping); (8) qualitative description of the peak velocity maps: R=rotation-like velocity fields; R/I=red-blue velocity gradient but irregular velocity field; I= irregular velocity field; F=no velocity gradients (see Section 4.2.1); (9) observed semimajor axis of the [O III] emission-line region from fitting an ellipse with uncertainties that are the typical seeing (i.e. 0″.7); (10) total projected extent of observed broad emission-line profiles (i.e. with $W_{80} > 600\,\mathrm{km\,s^{-1}}$) with conservative uncertainties of 2 × the seeing. Measurement uncertainties on the galaxy-integrated velocities are typically <10 per cent and therefore the dominant source of uncertainty is the physical interpretation of these values (see Section 4.2).
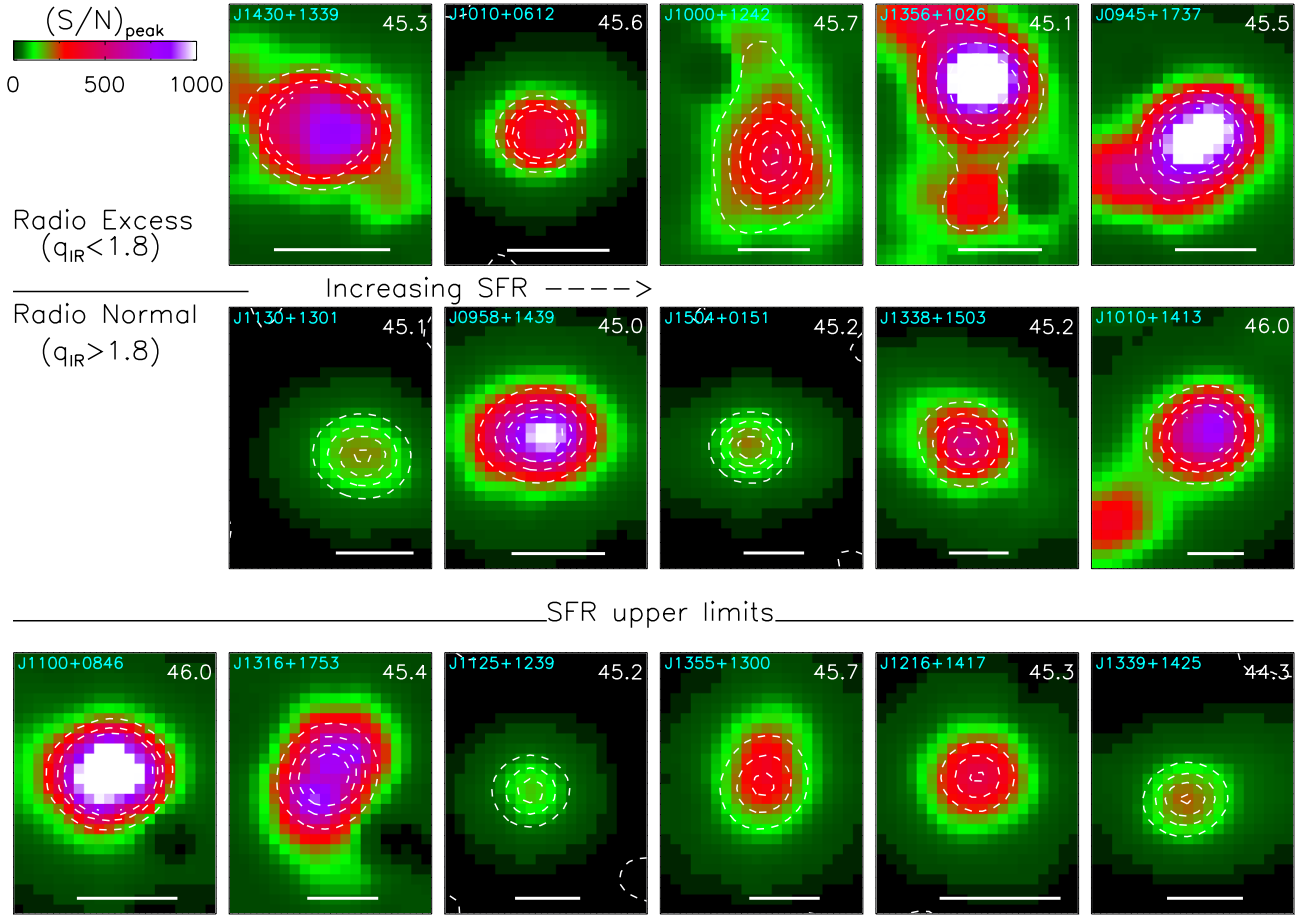
Figure 7. The [O III] peak S/N maps (see Section 3.3) for all 16 type 2 AGN in our sample. We have split the maps for the targets by radio excess (top row), radio normal (middle row) and those with only upper limits on their SFRs, for which we cannot determine their radio excess parameter (bottom row; see Table 2). The top two rows are arranged by SFR from the lowest (left) to the highest (right). The dashed contours show the morphology of the wavelength collapsed [O III] λ5007 images. The horizontal bars represent 3 kpc in extent. The numbers in the top right of each map is the AGN luminosity for that source (log [L_{AGN}; erg s^{-1}]; Table 2). The [O III] images are predominantly round or moderately elliptical and there is tentative evidence that the radio excess sources show a higher incidence of irregular morphologies.

4.1 Extended emission-line regions: sizes and morphologies

Although the ionized gas kinematics are the focus of this study, it is useful to make some initial comments on the emission-line region sizes and morphologies to compare to previous studies and to aid our later discussion. We detect [O III] emission over physical spatial extents of $\geq$10–20 kpc (i.e. in some cases the [O III] emission is extended beyond the IFU field of view). This is consistent with other studies that have shown that luminous AGN can have emission-line regions up to tens of kiloparsecs in size (e.g. Bennert et al. 2002; Humphrey et al. 2010; Greene et al. 2011; Harrison et al. 2012; Hainline et al. 2013; Husemann et al. 2013; Liu et al. 2013a; Schirmer et al. 2013). In Fig. 7 we show the peak [O III] S/N maps, for the whole sample, overlaid with contours showing the continuum-free [O III] λ5007 images (i.e. wavelength collapsed images around the emission line). We fit single ellipses to the [O III] emission-line images to calculate the semi-major axis ($R_{[O III]}$; Table 4). The range of sizes we get from this method are $R_{[O III]} = 1.5$–4.3 kpc, similar to, but generally higher than, the ULIRG-AGN composites observed in Rodríguez Zaurín et al. (2013). We note that if we subtract the typical seeing of the observations (see Table 4), in quadrature, from these size measurements they are reduced by $\approx$20 per cent with a *worst-case* scenario

of $\approx$50 per cent if the seeing reached 0.9 arcsec.[7] Based on a comparison to high-resolution imaging Rodríguez Zaurín et al. (2013) suggest that $R_{[O III]}$ is an overestimate of the emission-line region size for their sample; however, using the kinematics of our IFU data we commonly find spatially resolved emission over much larger extents (see Section 4.2 and Table 4) and therefore find that $R_{[O III]}$ is probably an underestimate of the size of the emission-line regions in our sources. Although we do not use identical methods, our observed sizes are comparable to, but towards the lower end of, those seen in the more luminous type 2 quasars in Liu et al. (2013a) as is expected by the [O III] size–luminosity relationship (e.g. Bennert et al. 2002; Hainline et al. 2013).

In agreement with previous studies of radio-quiet AGN (e.g. Husemann et al. 2013; Liu et al. 2013a; Liu, Zakamska & Greene 2014) we find that the emission-line regions in our sample are predominantly round or moderately elliptical (Fig. 7). However, we find tentative evidence that radio excess sources (i.e. those with the strongest evidence of radio emission above that expected from star

---

[7] The one source that has a $R_{[O III]}$ value smaller than 0.9 arcsec (i.e. our most pessimistic value of the seeing across the whole sample) was taken under good conditions of $\approx$0.6 arcsec and is therefore spatially resolved.

formation) have a higher incidence of extended and irregular morphologies. It has previously been shown that radio-loud quasars have a higher incidence of irregular morphologies than their radio-quiet counterparts (Liu et al. 2013a and references there-in). Although the radio data presented here are of insufficient spatial resolution to establish a direct (or lack there-of) connection, our results may imply that the presence of radio-AGN activity, even at modest luminosities, is connected to the morphologies of their emission-line regions (see also Husemann et al. 2013 and Appendix A). Alternatively, the 'radio excess' in these sources could be due to shocks that are also responsible for the irregular emission-line regions that we observe in Fig. 7 (see Zakamska & Greene 2014). Multifrequency high-resolution radio imaging is required to determine the origin and morphology of the radio emission in these objects.

4.2 Spatially resolved ionized gas kinematics

Multiple kinematic components (i.e. multiple narrow and broad components) are seen in the galaxy-integrated emission-line profiles of the sources in our sample (Fig. 5 and Figs A1–A15). There are several possible origins for these kinematic components such as merging nuclei, merger remnants or merger debris, halo gas, rotating gas discs and outflowing or inflowing gas. Indeed, previous spatially resolved spectroscopy of type 2 AGN has shown that multiple kinematic processes are likely to contribute to the overall emission-line profiles of ionized gas (e.g. Holt et al. 2008; Fischer et al. 2011; Villar-Martín et al. 2011a,b; Rupke & Veilleux 2013). By studying the spatially resolved velocity maps, velocity profiles and peak S/N maps from our IFU data (Figs 5, 6 and Figs A1–A15) we can distinguish between these scenarios and characterize individual kinematic components. Although the focus of our study is to identify and characterize galaxy-wide ionized outflows, in order to isolate the kinematics due to outflows we must also investigate these other kinematic features. In Section 4.2.1 we give a qualitative description of the observed kinematics due to galaxy rotation and merger features, including candidate dual AGN (summarized in Table 4), and in Section 4.2.2 we describe the outflow kinematics. The ionized gas kinematics for individual sources are described in Appendix A. We note here that most of the analysis is described on the basis of inspecting our velocity maps and velocity-distance profiles; however, we checked that these maps are a reasonable representation of the data by inspecting the spectra extracted from several regions across the IFUs (these spectra are shown in Fig. 5 and Figs A1–A15).

4.2.1 Ionized gas kinematics: galaxy rotation, mergers and dual AGN

Rotating gas discs will produce regular velocity fields, with a gradient of blue to red and relatively narrow emission-line profiles (i.e. $W_{80} < 600\,\mathrm{km\,s^{-1}}$). As discussed in Section 3.1 the emission-line peak velocity (v_{p}; see Fig. 4) predominantly traces the luminous narrow emission-line components in our data. We find regular v_{p} velocity fields and velocity profiles, indicative of tracing galaxy rotation (e.g. Courteau 1997), for 7 of the 16 objects in the sample. We give these a classification of 'R' in Table 4 and give a justification for this, for individual sources, in Appendix A. This interpretation of rotating discs is often supported by the kinematic 'major axis' (defined in Section 3.3) being aligned with the morphological major axis in the disc-like galaxies revealed in the SDSS images and/or the optical continuum seen in our IFU data. Indeed, it has previously been observed that the narrow components (or 'cores'; i.e.

with the broad-wings removed) of ionized emission-line profiles, can be good tracers of stellar dynamics (i.e. traces galactic rotation and/or stellar velocity dispersion) or molecular gas discs (e.g. Greene & Ho 2005; Barth, Greene & Ho 2008; Barbosa et al. 2009; Rupke & Veilleux 2013; but see Zakamska & Greene 2014). Further confirmation that the v_{p} velocity fields are tracing rotation would require detailed kinematic analysis (e.g. Courteau 1997; Krajnović et al. 2006) that is beyond the scope of this paper. In further five sources we see a velocity gradient from blue to red in the v_{p} velocity maps and profiles; however, the velocity fields are more irregular and therefore they may not be dominated by galaxy rotation but instead may trace kinematics due other processes such as merging components or outflows (given a classification 'R/I' in Table 4; see Appendix A for discussion of individual cases).

We next consider kinematics due to mergers. Mergers are known to create extended emission-line regions due to companion galaxies or merger debris and have previously been observed in spatially resolved spectroscopy of AGN (e.g. Villar-Martín et al. 2011a,b; Harrison et al. 2012). Furthermore, they may be expected to be common in our sample as $\gtrsim 60$ per cent of type 2 AGN at moderate redshifts $z \approx 0.3$–0.4 show signs of morphological disturbance at some level in *Hubble Space Telescope* (*HST*) imaging (Villar-Martín et al. 2012).[8] The [O III] emission-line peak S/N maps (Fig. 7) allow us to search for faint spatially distinct emission-line regions which could indicate companion/merging galaxies, merger debris, tidal features or halo gas. Based on these maps, five sources show spatially distinct emission-line regions with distinct velocities to the rest of the host galaxy. One of these has clear signs of major-merger activity based on the SDSS image and our IFU data (J1356+1026; Fig. A13), three are likely to be distinct emission-line regions (i.e. merger debris or halo gas; J0945+1737; Fig. A1; J1010+1413; Fig. 5 and J1000+1242; Fig. A3) and one could have several interpretations (J1316+1753; Fig. A9; these objects are discussed in detail in Appendix A).

Major mergers of galaxies naturally lead to the possibility of 'dual' AGN; i.e. two nuclei which are gravitationally bound and are both actively accreting material. Systematic spectroscopic searches for AGN with luminous double peaked [O III] emission-line profiles have become a popular method to identify candidate dual AGN (e.g. Wang et al. 2009; Liu et al. 2010; Smith et al. 2010; Ge et al. 2012; Comerford et al. 2013). However, these double peaks could also be due to other processes such as rotating gas discs, merging components or outflows, all illuminated by a single AGN (e.g. Fu et al. 2011, 2012; see Comerford et al. 2012 for a discussion). Two of our sources show luminous double peaks (J1316+1753 and J1356+1026) in their galaxy-integrated [O III] emission-line profiles. Based on our data, the strongest case for a dual AGN is J1356+1026 (see also Greene, Zakamska & Smith 2012), where we observe two distinct emission-line and continuum regions (see Appendix A for further discussion of these two sources).

### 4.2.2 Ionized gas kinematics: galaxy-wide outflows

In the IFU data of all 16 targets we find broad [O III] $\lambda\lambda4959, 5007$ emission-line profiles across the field of view (i.e. $W_{80,\,\mathrm{max}} \approx 720$–$1600\,\mathrm{km\,s^{-1}}$; Table 4) with a range of maximum projected

---

[8] We note that Villar-Martín et al. (2012) refer to low-level morphological disturbances of several types based on the classifications of Ramos Almeida et al. (2011). The number of *major mergers* observed in AGN is much lower (e.g. Cisternas et al. 2011).

velocity offsets ($|\Delta v_{max}| = 110$–540 km s^{-1}; Table 4). Such broad (i.e. $W_{80} \gtrsim 600$ km s^{-1}) and asymmetric [O III] emission-line profiles, are difficult to explain with mergers or galaxy rotation, even for the most massive galaxies, and are attributed to high-velocity outflowing gas (e.g. Heckman et al. 1981; Veilleux et al. 1995; Greene & Ho 2005; Barth et al. 2008; Nesvadba et al. 2008; Greene et al. 2011; Harrison et al. 2012; Westmoquette et al. 2012; Liu et al. 2013b; Rupke & Veilleux 2013). As with all of these studies we favour outflow over inflow due to the exceptionally high velocities and line widths that we observe. In the previous section we isolated kinematic components due to other features (e.g. mergers and galaxy rotation) and we find that these have little effect on the observed kinematic structure of the line width, W_{80} and also in most cases that of the velocity offset, Δv (the exceptions are J1356+1026 and J1316+1753 for which Δv is affected, see Appendix A for details); i.e. these maps are dominated by outflow kinematics. We therefore use these maps to describe the outflow kinematic structures and morphologies. We note that Liu et al. (2013b) use the velocity structure of the median velocity (v_{med}; Fig 4), in which they predominantly see a blue to red velocity gradient, as part of their outflow analysis of their IFU data of $z = 0.3$–0.6 radio-quiet luminous type 2 AGN. We observe a very similar range in maximum line widths and v_{med} maximum velocity gradients (i.e. $\Delta v_{med,\,max} \approx 55$–$520$ km s^{-1}; Table 4) to the objects in Liu et al. (2013b). However, by spatially

resolving v_{med} we find that this quantity is predominantly dominated by the kinematics of the v_p velocity field (Fig. 6 and Figs A1–A15) and consequently v_{med} can often be dominated by kinematics due to galaxy rotation and mergers (see Section 4.2.1). Therefore, we favour Δv over v_{med} to describe the projected outflow velocity offset for the rest of our analysis.

For an outflow consisting of ionized clouds (observable in [O III] emission) embedded in a bulk outflow (e.g. Heckman et al. 1990; Crenshaw & Kraemer 2000) the projected velocity offsets will be sensitive to inclination effects while the emission-line widths (i.e. W_{80}) are more likely to reflect typical bulk motions and be less sensitive to inclination (also see discussion in Harrison et al. 2012). We therefore concentrate on the W_{80} maps to investigate the sizes and morphologies of the outflows (Fig. 8), comparing them with the Δv maps when appropriate (discussed in Appendix A for individual objects). The *observed* outflow velocities and morphologies will also depend on other factors. For example, an outflow with the far side obscured by dust can explain the excess of blue wings in [O III] emission-line profiles (e.g. Heckman et al. 1981; Vrtilek 1985; Veilleux 1991) while, outflowing redshifted components can be explained if the outflow is highly inclined and/or is extended beyond the likely obscuring material (e.g. Barth et al. 2008; Crenshaw et al. 2010; Greene et al. 2012; Rupke & Veilleux 2013). We observe both red and blue velocity offsets in our sample (Table 4). A range of
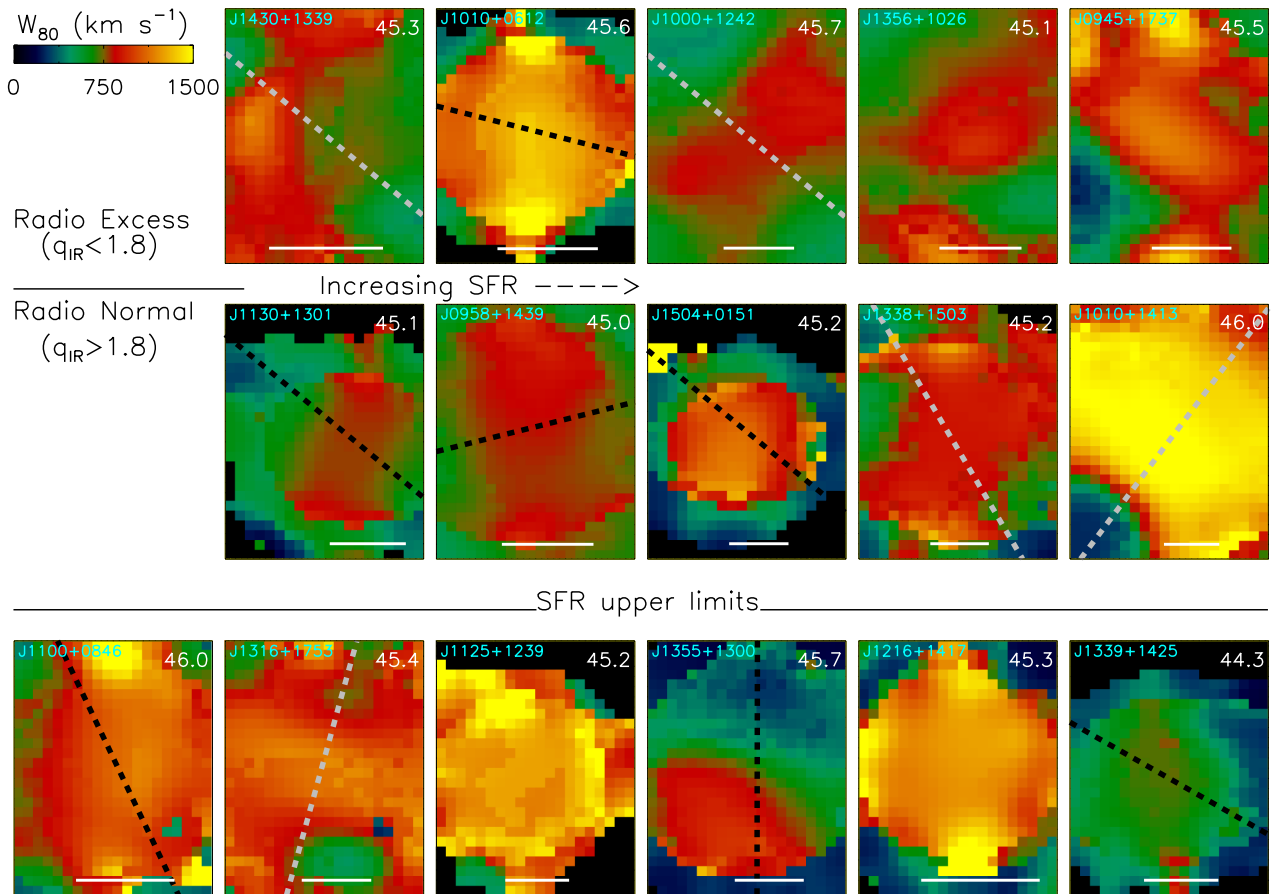
Figure 8. Maps of W_{80} for all 16 type 2 AGN in our sample that illustrate the spatial extent and morphology of the outflows (Section 4.2.2). The maps are ordered in an identical manner to Fig. 7. The dashed lines correspond to the 'major axes' based on the kinematics of the narrow emission-line components (Section 3.3). Black dashed lines are those with blue to red velocity gradients indicative of rotation (i.e. 'R' in Table 4) and grey are those with irregular blue to red velocity gradients (i.e. 'R/I' in Table 4). Sources without a clear blue to red velocity gradient do not have these 'major axes' shown. The solid horizontal bars represent 3 kpc in extent and the number in the top right of each map is $\log [L_{AGN}; \mathrm{erg\ s^{-1}}]$ for that source. We observe a wide variety in the morphology of the kinematically disturbed ionized gas and there is no obvious connection between outflow morphology and SFR, radio excess or AGN luminosity.

structures of outflows have been observed in galaxies both with and without powerful AGN, including spherically symmetric outflows and bi-polar superbubbles (e.g. Veilleux et al. 1994; Greene et al. 2012; Liu et al. 2013b; Rupke & Veilleux 2013). Detailed modelling of the outflow kinematics of individual objects is beyond the scope of this paper; however, we briefly describe the morphology and kinematics of the outflows that we observe in our sample below (we describe individual objects in more detail in Appendix A).

We define the quantity D_{600} (values in Table 4) which is the maximum projected spatial extent of the broad [O III] emission-line profiles (with $W_{80} > 600\,\mathrm{km\,s^{-1}}$; i.e. where the kinematics are likely to be dominated by outflows) based upon the velocity profiles (Fig. 6 and Figs A1–A15). The outflow features are located over large extents in all sources ($D_{600} \gtrsim [6-16]\,\mathrm{kpc}$; Table 4) with the spatial extents being mostly lower limits due to the limited field of view of our observations. We note that in most cases the broad [O III] emission is clearly spatially extended, due to the morphological or kinematic structure that we observe (see below) and in all cases it is extended beyond the seeing; however, a conservative uncertainty on these D_{600} measurements would be ≈ 2 times seeing (see Table 4). Although our sample was initially selected to have luminous and broad [O III] emission-line components (see Section 2.1), these results demonstrate that when these components are seen in the one-dimensional spectra of luminous type 2 AGN (as is the case for at least 45 ± 3 per cent of objects; see Section 2.1 and Fig. 2), they are always found over galaxy-wide scales when observed with spatially resolved spectra (i.e. over at least a few kiloparsecs). To assess how confident we can be of the fraction of extended ionized outflows within our selection criteria we ran Monte Carlo simulations. To do this, we took 246 mock galaxies (i.e. the number from the parent catalogue that met our selection criteria; Section 2.1), assigned them as either 'extended' or 'not extended' (in various ratios) and randomly drew 16 objects from this sample 10^4 times. We found that, at most, 30 per cent of the sources can be 'not extended' in the parent population for the probability of selecting 16 'extended' sources by random chance to be ≤ 0.3 per cent (i.e. the 3σ confidence level). In other words, when broad and luminous emission-line components are observed in one-dimensional spectra (i.e. when $\gtrsim 30$ per cent of the ionized gas appears to be outflowing; Section 2.1) of luminous ($L_{\mathrm{[O\,III]}} > 5 \times 10^{41}\,\mathrm{erg\,s^{-1}}$) $z < 0.2$ type 2 AGN, we can be confident, with 3σ significance, that in *at least* 70 per cent of instances these features are extended on a few kiloparsec scales or greater.

In Fig. 8 we show the W_{80} maps for the whole sample to illustrate the morphology of the outflows. From this figure we can see a large diversity in the morphology. Several of the sources show a preferential axis, which is orientated away from the galaxy 'major axis' (albeit not always perpendicular); however, in some cases we require a stronger constraint on the major axis of the host galaxies to confirm the relative orientations. This is consistent with the collimated winds emerging along the minor axis seen in star-forming galaxies (e.g. Heckman et al. 1990; Rupke & Veilleux 2013). The most impressive outflows that we observe are those which have the kinematic features of ≈ 10–15 kpc scale superbubbles; i.e. high-velocity bi-polar emission-line regions each side of the nucleus. Combining our IFU data with archival imaging and spectroscopic data (see Appendix A) we identify three superbubble candidates (one was previously known: J1356+1026; Greene et al. 2012 and, as far as we are aware, two are new: J1000+1242 and J1430+1339; see Appendix A). In two cases (J1356+1026 and J1430+1339) we only observe the base of these bubbles and therefore require IFU observations with a larger field of view to fully characterize the

kinematics of the outflow structure. In the third case (J1000+1242) we see a clear blue and red sided outflow. Similar outflows have been seen in galaxies both with and without luminous AGN (e.g. Veilleux et al. 1994; Greene et al. 2012; Rupke & Veilleux 2013).

In four of our targets the morphology of the outflows are circular (Fig. 8) with reasonably constant W_{80} and Δv values seen across the extent of the emission-line regions. This kinematic structure is seen in the majority of the more luminous type 2 AGN in Liu et al. (2013b) who argue that these structures are characteristic of spherically symmetric, or wide-angle bi-conal outflows, and a power-law [O III] surface brightness profile (see Liu et al. 2014, for similar observations of type 1 AGN). We note that circular morphologies could (at least partially) be an artefact of the fitting routine since in areas of low surface brightness only single Gaussian components are fit and we are not able to fully characterize the emission-line profile (see Section 3.2); however, this not likely to be the full explanation for the observed morphologies (see Appendix A; also see fig. 5 of Liu et al. 2013b). Finally, in one source (J1355+1300) we observe a spatially distinct high-velocity region, offset from the nucleus, that has a few possible interpretations including a small-scale outflowing bubble (see Appendix A for a discussion).

4.3 Outflow properties: estimates of mass, energy and momentum

The mass, energy and momentum being carried by galaxy-wide outflows are important quantities to constrain in order to understand the role that outflows play in galaxy formation (discussed in Section 5.2) and to also help determine the physical mechanisms that are driving them (discussed in Section 5.1). Outflows are likely to be entraining gas in multiple phases (i.e. ionized, molecular and neutral) and multiple gas phase observations are required to fully characterize the outflow properties (e.g. Shih & Rupke 2010; Mahony et al. 2013; Rupke & Veilleux 2013). However, the warm ionized gas, which we observe in our observations, provides initial information on the outflows in this sample and could represent a large fraction of the overall mass and energy of the total outflows, as has been shown for some AGN (e.g. Rupke & Veilleux 2013). The kinematic structures of the outflows across our sample are diverse and complex (see Section 4.2.2) which makes accurate characterization of the outflows challenging without doing detailed kinematic modelling of individual systems. However, as is often invoked throughout the literature, we can apply some simple outflow models to the whole sample to provide first order constraints on the mass, energy and momentum involved in the outflows and to enable a direct comparison to other studies. As most of the calculations outlined below require measurements of the Hβ luminosity, we do not include the three sources where we did not make this measurement (see Section 3.2).

An important quantity for measuring ionized gas masses, and hence mass outflow rates, is the electron density (n_e). This quantity is often measured from the emission-line ratio [S II] $\lambda 6716/\lambda 6731$ which is sensitive to electron density (e.g. Osterbrock & Ferland 2006). The [S II] doublet is not covered in our IFU observations; however, using single-component Gaussian fitting to the SDSS spectra we find that the emission-line ratios for our sources are in the range [S II] $\lambda 6716/\lambda 6731 = 0.8$–1.2, corresponding to a range of $n_e \approx 200$–1000 cm^{-3} with a median of $n_e = 500$ cm^{-3} (Osterbrock & Ferland 2006; assuming $T_e = 10^4$ K). This range of n_e is in agreement with that previously found for type 2 AGN (e.g. Greene et al. 2011). We note that these are average electron densities within the SDSS fibre and the values for the *outflowing* kinematic components

are unknown and have the potential to be outside of the electron density range that the [S II] $\lambda\lambda6716, 6731$ doublet is sensitive to (i.e. $n_e \gtrsim 10^4$ cm^{-3}; Osterbrock & Ferland 2006; see discussion in Holt et al. 2011; Rodríguez Zaurín et al. 2013), providing a source of uncertainty in the mass and energy outflow rates in *all* studies that use this method. However, we note that Greene et al. (2011) provide convincing arguments that the emission-line regions in their $z < 0.5$ radio-quiet type 2 AGN are likely to be clumpy and that standard mass estimates (such as those we derive below) are likely to be underestimated.

The observed ionized gas mass (i.e. the gas which is emitting in Hβ) can be estimated assuming purely photoionized gas with 'Case B' recombination (with an intrinsic line ratio of Hα/H$\beta = 2.9$) and an electron temperature of $T = 10^4$ K, following Nesvadba et al. (2011) and Osterbrock & Ferland (2006), using the relation[9]

$$\frac{M_{\text{gas}}}{2.82 \times 10^9\,\text{M}_\odot} = \left(\frac{L_{\text{H}\beta}}{10^{43}\,\text{erg s}^{-1}}\right)\left(\frac{n_e}{100\,\text{cm}^{-3}}\right)^{-1}. \quad (2)$$

This relationship between the observed line-emitting gas mass, n_e and $L_{\text{H}\beta}$ (or an equivalent using $L_{\text{H}\alpha}$) is commonly adopted in studies of outflows (e.g. Holt et al. 2006; Genzel et al. 2011; Liu et al. 2013b; Rodríguez Zaurín et al. 2013; Schnorr-Müller et al. 2014) with normalization factors that vary within a factor of a few, depending on the exact assumptions. Using our extinction uncorrected $L_{\text{H}\beta}$ values (Table 2), we obtain total observed ionized gas masses of $M_{\text{gas}} = (2-40) \times 10^7$ M$_\odot$, assuming the commonly adopted $n_e = 100$ cm^{-3} (e.g. Liu et al. 2013b), or $M_{\text{gas}} = (0.4-8) \times 10^7$ M$_\odot$ assuming our median value of $n_e = 500$ cm^{-3}. We note that the ionized gas phase will make up only a fraction of the *total* gas content. For example, taking a typical SFR for our targets (40 M$_\odot$ yr^{-1}) and assuming a star-forming region of ≈ 1 kpc would imply molecular gas masses of $\approx 10^{10}$ M$_\odot$ (Genzel et al. 2011).

The simplest method that we can use to estimate the total kinetic energy in the outflows is the following:

$$E_{\text{kin}} = \frac{1}{2}M_{\text{gas}}v_{\text{gas}}^2. \quad (3)$$

Following Liu et al. (2013b) we assume $n_e = 100$ cm^{-3} and that all of the observed ionized gas is involved in the outflow[10] with a bulk-outflow velocity $v_{\text{gas}} = W_{80}/1.3$ (suitable for the spherically symmetric or wide-angle bi-cone outflow models outlined Liu et al. 2013b; see also Harrison et al. 2012 for different arguments on using line widths to estimate the bulk velocities). Across the sample

---

[9] To be consistent with Liu et al. (2013b), Equation (2) is given in the exact form that is provided in Nesvadba et al. (2011). However, we note that following section 4.2 in Osterbrock & Ferland (2006) with the appropriate value for the recombination coefficient of Hβ for the conditions described (i.e. $\alpha_{\text{H}\beta}^{\text{eff}} = 3.03 \times 10^{-14}$ cm^3 s^{-1}) the normalisation constant in Equation (2) would be 6.78×10^8 M$_\odot$. This factor of four difference to the quoted normalization constant has no significant bearing on our order of magnitude estimates of the gas mass.

[10] As discussed in Section 4.2.1 not all of the ionized gas appears to be involved in an outflow. The broad kinematic components (FWHM > 700 km s^{-1}) in the [O III] and Hβ emission lines typically contribute 30–80 per cent of the total flux (based on Mullaney et al. 2013) which may give an estimate of the fraction of gas involved in the outflows. However, the emission-line ratios of up to Hα/H$\beta = 8$ (from Mullaney et al. 2013) implying that the intrinsic $L_{\text{H}\beta}$ values (and hence total calculated masses) may be up to a factor of 10 times higher than the observed values (following Calzetti et al. 2000). Therefore, these two effects will cancel each other out to some level and this assumption is sufficient for our order-of-magnitude estimates.

this leads to total kinetic energies of $E_{\text{kin}} = (0.5-50) \times 10^{56}$ erg. Assuming the typical maximum radial extent of the outflows is 6 kpc (see Table 4) and a continuous outflow, this implies outflow lifetimes of $t_{\text{out}} \approx 6\,\text{kpc}/v_{\text{gas}} = (5-11)$ Myr and consequently outflow kinetic energy rates of $\dot{E}_{\text{kin}} = (0.1-30) \times 10^{42}$ erg s^{-1}.

An alternative approach is to assume a spherical volume of outflowing ionized gas (following e.g. Rodríguez Zaurín et al. 2013; see also Holt et al. 2006), which gives mass outflow rates of

$$\dot{M}_{\text{out,M1}} = \frac{3M_{\text{gas}}v_{\text{out}}}{r} \quad (4)$$

and outflow kinetic energy rates of

$$\dot{E}_{\text{out,M1}} = \frac{\dot{M}}{2}\left(v_{\text{out}}^2 + 3\sigma^2\right), \quad (5)$$

where σ is the velocity dispersion and v_{out} is the outflow velocity. To match Rodríguez Zaurín et al. (2013) as closely as possible[11] we take the outflow velocity to be $v_{\text{out}} = \Delta v$, the velocity dispersion to be $\sigma = W_{80}/2.355$, the outflow radius to be $r = R_{[\text{O III}]}$ (Table 4) and again use $n_e = 100$ cm^{-3}. Using this approach (we will call 'Method 1') we obtain $\dot{M}_{\text{out,M1}} = 3-70$ M$_\odot$ yr^{-1} and $\dot{E}_{\text{out,M1}} = (0.3-30) \times 10^{42}$ erg s^{-1}. This range in outflow kinetic energy rate is in excellent agreement with the range of values using the previous method, which we will now ignore, and the two methods agree within a factor of ≤ 3 for all sources. Both of these methods provide strict lower limits, as we are only observing the line-emitting gas and hence the total mass involved in the outflow could be much higher (see also e.g. Greene et al. 2011; Liu et al. 2013b).

We also consider the mass and energy injection rates assuming an energy conserving bubble in a uniform medium (e.g. Heckman et al. 1990; Veilleux et al. 2005; Nesvadba et al. 2006, and references therein), which gives the relation

$$\dot{E}_{\text{out,M2}} \approx 1.5 \times 10^{46} r_{10}^2 v_{1000}^3 n_{0.5}\,\text{erg s}^{-1}, \quad (6)$$

where r_{10} is taken to be half the extent of the observed broad [O III] emission (in units of 10 kpc; we assume $r_{10} = 0.6$ for all sources; Table 4), v_{1000} are the velocity offsets in units of 1000 km s^{-1} (we assume $v_{1000} = W_{80}/1300$; Table 4) and $n_{0.5} \approx 1$ is the ambient density (ahead of the expanding bubble in units of 0.5 cm^{-3}). Using this method (we will call 'Method 2') we obtain values of $\dot{E}_{\text{out,M2}} \approx (0.7-7) \times 10^{45}$ erg s^{-1}. The mass outflow rates are then given by $\dot{M}_{\text{out,M2}} = 2\dot{E}_{\text{out,M2}}/v_c^2 \approx (9-20) \times 10^3$ M$_\odot$ yr^{-1}.

We consider 'Method 1' and 'Method 2' to be lower and upper bounds of the mass outflow rates and kinetic energy rates (see also discussion in Greene et al. 2012) and the fiducial values we will use throughout are the mean (in log space) of these two values which are $\dot{E}_{\text{out}} = (0.15-45) \times 10^{44}$ erg s^{-1} and $\dot{M}_{\text{out}} = 170-1200$ M$_\odot$ yr^{-1}. Comparing these values to those found using the approach followed in Liu et al. (2013a,b) provides confirmation that using these fiducial values are reasonable. They argue that the NLR in luminous type 2 AGN can be well described by relatively dense clouds embedded in a hot, low-density, volume-filling wind. A spatial profile with a constant [O III]/Hβ emission-line ratio followed by a sharp decline in this value indicates the break where the clouds become optically thin to ionizing radiation (see full description in Liu et al. 2013b). In four of our sources (these are J0958+1439; J1100+0846; J1316+1753;

---

[11] We note that Rodríguez Zaurín et al. (2013) use a different definition of v_{out} to Δv; however, the two methods agree within a factor of $\approx(1-3)$ with a median of 1.1. Likewise, their definition for σ agrees with $\sigma = W_{80}/2.355$ within a factor of $\approx(1-2)$ and median of 1.2.

J1339+1425; see Appendix A) we see the same sharp decline in the [O III]/Hβ ratio (in most of the other sources this transition may happen beyond our field of view). For these four sources, the kinetic energies and mass outflow rates using their method (see Appendix A) are all within a factor of $\approx$1–3 of the fiducial values we chose to adopt here.[12]

Finally, in preparation for our discussion in Section 5.1, we estimate the mean and upper and lower bounds of outflow momentum rates by taking the mass outflow rates calculated above and assuming $\dot{P}_{out} = \dot{M}_{out} v_{gas}$.

5 DISCUSSION

We have presented our IFU data for a sample of 16 luminous type 2 AGN which traces the ionized gas kinematics (via [O III] and Hβ emission lines) over kiloparsec scales. We have decoupled the kinematics of outflows from other kinematic components, such as galaxy dynamics and mergers, and show that energetic, galaxy-wide ionized outflows are ubiquitous in our sample. Our sample is selected from a well-constrained parent sample so that we can place our observations into the context of the overall AGN population. In this section we use our observations, combined with previous observations from the literature, to discuss the likely driving mechanisms of the outflows (Section 5.1) and the role that these outflow may play in galaxy evolution (Section 5.2).

5.1 What drives the outflows?

The dominant processes that drive galaxy-wide outflows in massive galaxies and the efficiency to which they are able to couple the gas are currently sources of uncertainty in galaxy formation models. Several possible mechanisms have been suggested to drive galaxy-wide outflows, for example: the mechanical input from stellar winds and supernovae (e.g. Heckman et al. 1990; Leitherer et al. 1999); direct radiation pressure from the luminosity of an AGN or star formation (e.g. Murray, Quataert & Thompson 2005); the interaction of radio jets (launched by the AGN) with a clumpy and multiphase interstellar medium (ISM; e.g. Sutherland & Bicknell 2007; Wagner, Bicknell & Umemura 2012); and AGN winds, initially launched at the accretion disc, that propagate through the galaxy and sweep up the ISM (e.g. King, Zubovas & Power 2011; Faucher-Giguère & Quataert 2012). In this section we will investigate which of these processes could be responsible for driving the outflows observed in our targets.

5.1.1 Morphology and structure

A possible method to distinguish between an AGN-driven and star formation driven outflow could be the morphology and structure of the outflow. Galactic-scale star formation driven outflows are known to propagate along low-density regions, perpendicular to galaxy discs (e.g. Heckman, Armus & Miley 1987; Ohyama et al. 2002; Veilleux et al. 2005). In contrast, outflows driven by an AGN on *small scales* have no relation between the orientation of the outflow and the disc in the host galaxy (e.g. Fischer et al. 2013). However, if AGN-driven outflows propagate to galaxy-wide scales they may also be forced to propagate away from the galaxy disc along a path of least resistance (e.g. Faucher-Giguère & Quataert 2012; Gabor & Bournaud 2014) which could make galactic-scale outflows driven from a nuclear star-forming region or an AGN indistinguishable

---

[12] Although here we use a different method to Liu et al. (2013b) we verified our results using a similar method to these authors using IRAF ELLIPSE.

(see also Hopkins & Elvis 2010; Heckman et al. 2011; Diamond-Stanic et al. 2012 for other reasons why it could be difficult to distinguish between AGN and star formation driven outflows). In some observations compact radio jets ($\lesssim$ few kiloparsec in size) are inferred to play a role, where the combination of high-resolution radio data and spatially resolved spectroscopy has shown that high-velocity gas (in multiple phases) is spatially co-incident with radio emission (Baldwin et al. 1980; Whittle et al. 1988; Capetti et al. 1999; Whittle & Wilson 2004; Emonts et al. 2005; Morganti et al. 2005, 2013; Leipski & Bennert 2006; Barbosa et al. 2009; Fu & Stockton 2009; Storchi-Bergmann et al. 2010; Shih, Stockton & Kewley 2013). However, even when radio jets *are* present it appears that they may not always be fully responsible for the observed outflows and other processes are also required (e.g. Villar-Martín et al. 1999; Rupke & Veilleux 2011; Riffel, Storchi-Bergmann & Riffel 2014).

The morphologies of the outflows in our targets are illustrated in Fig. 8. In our sample we observe no obvious relationship between the morphology of the observed outflows and the SFRs, AGN luminosities or radio excess parameters of the host galaxies; i.e. irrespective of the host galaxy or AGN properties we see a range in outflow morphology including those which are escaping away from the galaxy discs. This is in broad agreement with Rupke & Veilleux (2013) who find no structural difference between the outflows in the ULIRGs with and without luminous AGN. Interestingly, all of superbubble candidates are radio excess sources (see Section 4.2.2 and Appendix A). However, deeper and higher resolution radio data are required to search for small and low-luminosity radio jets, which we cannot identify in the FIRST data, and to ultimately determine the origin of the radio emission (see Section 2.4).

5.1.2 Outflow velocities compared to AGN and galaxy properties

Another possible method to determine the driving mechanism of outflows is to search for trends between outflow properties and properties of the host galaxy or AGN. Positive correlations have been claimed to exist between outflow properties, albeit using different observations, for each of SFR (e.g. Martin 2005; Rupke et al. 2005; Bradshaw et al. 2013), AGN luminosity (e.g. Cicone et al. 2014) and radio luminosity (e.g. Nesvadba et al. 2011). Of course these analyses are complicated by the fact that AGN luminosity, SFR and radio luminosity are closely related (e.g. Tadhunter et al. 1998; Ivison et al. 2010; Mullaney et al. 2012; Chen et al. 2013) and that small duty cycles may mean that an AGN-driven outflow may be observed when the AGN itself is no longer observable (e.g. King et al. 2011; Gabor & Bournaud 2014).

In Fig. 9 we show that the line widths (W_{80}) and maximum velocities (v_{02}) of our sample are comparable to those found in more luminous type 2 AGN (Liu et al. 2013b) and ULIRG-AGN composite galaxies (Rodríguez Zaurín et al. 2013).[13] We observe no clear trends between v_{02} or W_{80} and $L_{[O III]}$, despite four orders of magnitude in [O III] luminosity. Additionally, although limited in dynamic range, we do not see any obvious correlation in W_{80} or v_{02} with radio luminosity (Fig. 9). These conclusions are consistent with Mullaney et al. (2013) who demonstrate that the broadest emission lines are prevalent for AGN with radio luminosities of $L_{1.4GHz} \gtrsim 10^{23}$ W Hz^{-1} (i.e. the range that is covered in Fig. 9),

---

[13] Although Rodríguez Zaurín et al. (2013) do not quote the values of W_{80} and v_{02} directly, we reconstructed the emission-line profiles (from the Gaussian components given in their paper) and then measure these values directly.
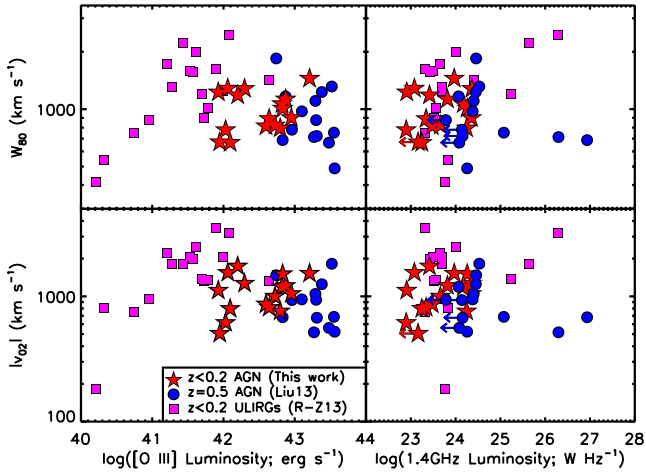
Figure 9. Line width (W_{80}) and maximum velocity (v_{02}) versus [O III] luminosity and 1.4 GHz radio luminosity for our targets (red stars; see Table 2 and Table 4). Also shown are $z \approx 0.3$–0.6 type 2 quasars (blue circles; Liu et al. 2013b) and $z < 0.1$ ULIRG-AGN (magenta squares; Rodríguez Zaurín et al. 2013). High-velocity and disturbed ionized gas is found in AGN over four orders of magnitude in both [O III] and radio luminosity; however, no clear trends are observed between these quantities from these samples.

but found no clear trends with [O III] luminosity when taking radio-luminosity matched samples of AGN. We note that Fig. 1 is not radio-luminosity matched so gives an apparent positive trend between [O III] luminosity and line width; see Mullaney et al. (2013) for details.

In Fig. 10 we compare the galaxy-integrated line widths (W_{80}) and maximum velocities (v_{02}) to the infrared luminosities from star formation ($L_{\mathrm{IR, SF}}$; a proxy for SFR), bolometric AGN luminosities (L_{AGN}) and the radio excess parameter (q_{IR}) derived in Section 2.4. We also compare to the ULIRG-AGN composite galaxies from Rodríguez Zaurín et al. (2013)[14] and the $z < 0.06$ ULIRGs from Rupke & Veilleux (2013; who make these velocity measurements from various ionized emission-line species). In Fig. 10, the only possible trend we observe is between the maximum velocity (v_{02}) and AGN luminosity, although we are limited in measurements below $L_{\mathrm{AGN}} = 10^{45}$ erg s^{-1}. Based on these samples, although high-velocity outflow features are observed across the samples, the most extreme velocities (i.e. $v_{02} \gtrsim 2000$ km s^{-1}) and line widths (i.e. $W_{80} \gtrsim 1500$ km s^{-1}) appear to be predominantly found in the quasar-ULIRG composite galaxies (Fig. 10). This is in broad agreement with other studies of the outflows in ULIRGs and quasars, in multiple different gas phases, that find the most extreme outflows in the quasar-ULIRG composites (e.g. Harrison et al. 2012; Westmoquette et al. 2012; Veilleux et al. 2013; Cicone et al. 2014; Hill & Zakamska 2014). Further evidence that the incidence of extreme ionized outflows in quasar-ULIRG composite galaxies is high, compared to the overall population, is that 16/17 of the objects in Rodríguez Zaurín et al. (2013) have extreme ionized gas kinematics (i.e. significant

broad [O III] emission-line components) which is much larger than we find for the overall optical AGN population (see Section 2.1), and considerably higher than expected given their moderate [O III] luminosities (i.e. $L_{\mathrm{[O\,III]}} \lesssim 10^{42}$ erg s^{-1}; Fig. 1). Furthermore, the flux-weighted average line widths (FWHM$_{\mathrm{avg}} \gtrsim 800$ km s^{-1}) of these quasar-ULIRG composites are representative of the top $\approx$2–3 per cent most extreme objects in Mullaney et al. (2013). This result is not sufficient to establish which process is driving the observed outflows, but instead may demonstrate that the most extreme outflows are most prevalent during an active star formation and AGN phase as is predicted by some evolutionary models (e.g. Sanders et al. 1988; Hopkins et al. 2008).

Finally, we note that Mullaney et al. (2013) show that the fraction of sources with their ionized gas dominated by outflows was considerably higher for sources with moderate-to-high radio luminosities ($L_{\mathrm{1.4\,GHz}} \gtrsim 10^{23}$ W Hz^{-1}). Based on the analysis of the radio emission in our sources and the comparison samples (Section 2.4; Fig. 10), star formation could contribute considerably to the radio emission. Additionally, as noted by Zakamska & Greene (2014), radio emission could be produced by shocks due to outflows that were driven by e.g. quasar winds. Further analysis of the parent population is required to establish the physical process that is driving the trend between radio luminosity and ionized outflows.

5.1.3 Coupling efficiencies and momentum fluxes

A popular method to investigate the likely drivers of galactic-scale outflows is to compare the energy and momentum available from each potential driver (i.e. supernovae and stellar winds, radiation pressure [from AGN or star formation], AGN winds, or radio jets) to the kinetic energy and momentum in the outflows. Although we are limited by a large uncertainty in the outflow kinetic energies (see Section 4.3), we have measured SFRs and AGN luminosities and have identified the sources that are most likely to host radio jets (see Section 2.4 and Table 2). In Fig. 11 we compare the ratio of our outflow kinetic energy rates ($\dot{E}_{\mathrm{out}}$) with (1) the bolometric AGN luminosities; (2) the infrared star formation luminosities[15] and (3) the mechanical radio jet power (estimated using the 1.4 GHz luminosity and the relationship in Cavagnolo et al. 2010). In Fig. 12 we compare the momentum rates of the outflows ($\dot{P}_{\mathrm{out}}$) with the momentum flux output radiatively by (1) star formation (i.e. $L_{\mathrm{IR, SF}}/c$) and (2) the AGN (i.e. L_{AGN}/c). Using these results we now explore the plausibility of different potential driving mechanisms and compare to theoretical predictions.

Fig. 11 shows that a similar outflow coupling efficiency is required to the radiative output of both the AGN (i.e. $\approx$0.5–10 per cent) and star formation (i.e. $\gtrsim$0.5–40 per cent), indicating that either of these processes could power the outflows if they are able to couple their energy to the gas. One way for star formation to drive an outflow is from stellar winds and supernovae. An estimate of the maximum energy injection from stellar winds and supernovae, which is used throughout the literature, is $\approx 7 \times 10^{41}(\mathrm{SFR}/\,\mathrm{M}_{\odot}\,\mathrm{yr}^{-1})$ erg s^{-1} (applicable for stellar ages $\gtrsim$40 Myr and following Leitherer et al. 1999; Veilleux et al. 2005).[16] This corresponds to a maximum $\dot{E}_{\mathrm{out}}/L_{\mathrm{IR,SF}} \approx 2$ per cent (following Kennicutt 1998 but correcting to a Chabrier IMF) that we

---

[14] We fit the SEDs to the *IRAS* and *WISE* data for these sources in a consistent manner to that described in Section 2.4; however, we only accept AGN components if the AGN template contributes $\geq$50 per cent of the flux at 19 μm due to the difficulty in reliably identifying low-luminosity AGN in ULIRGs using this method (see Del Moro et al. 2013). Eight of these ULIRGs also have AGN luminosities derived from *Spitzer* infrared spectra in Veilleux et al. (2009) that we use in favour of our AGN luminosities. We found that the AGN luminosities and IR luminosities are well matched (within a factor of $\lesssim$2) between our method and that in Veilleux et al. (2009).

[15] We note that for infrared luminous galaxies (i.e. $L_{\mathrm{IR}} \geq 10^{11}$ L$_{\odot}$), the infrared luminosity makes up the bulk of the bolometric luminosity; e.g. Sanders & Mirabel (1996) and Veilleux et al. (2005).

[16] If we were to follow instead Dalla Vecchia & Schaye (2008) to estimate this energy input, the values would be a factor of $\approx$2 lower.
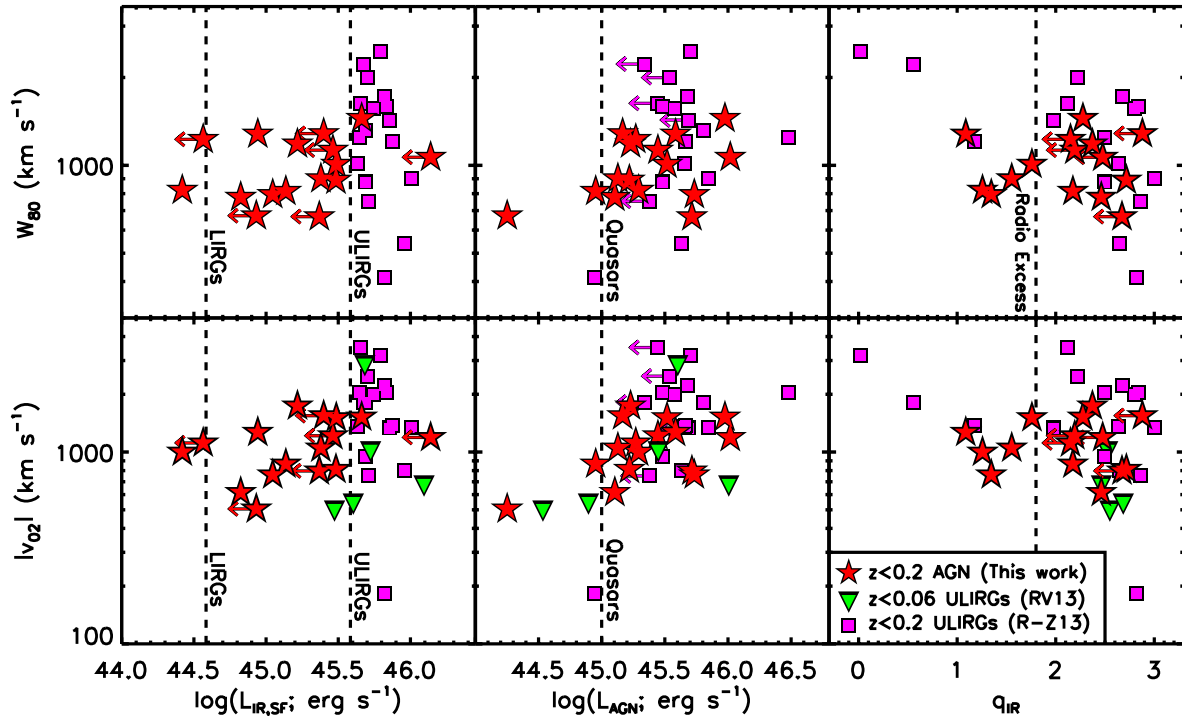
Figure 10. Line width (W_{80}) and maximum velocity (v_{02}) versus infrared luminosity from star formation, AGN luminosity and q_{IR} for our targets (red stars; see Table 2 and Table 4). Also shown are $z < 0.2$ ULIRG-AGN composite galaxies (magenta squares; Rodríguez Zaurín et al. 2013) and $z < 0.06$ ULIRGs (green triangles; Rupke & Veilleux 2013). There is tentative evidence that most extreme velocities and line widths are preferentially found in systems with high SFRs (i.e. ULIRGs) that host the most luminous AGN (i.e. 'quasars'). There is no such effect seen when comparing systems where there is excess radio emission AGN; however, low-level excess radio emission is difficult to identify using this method especially in high SFR systems (see Section 2.4).
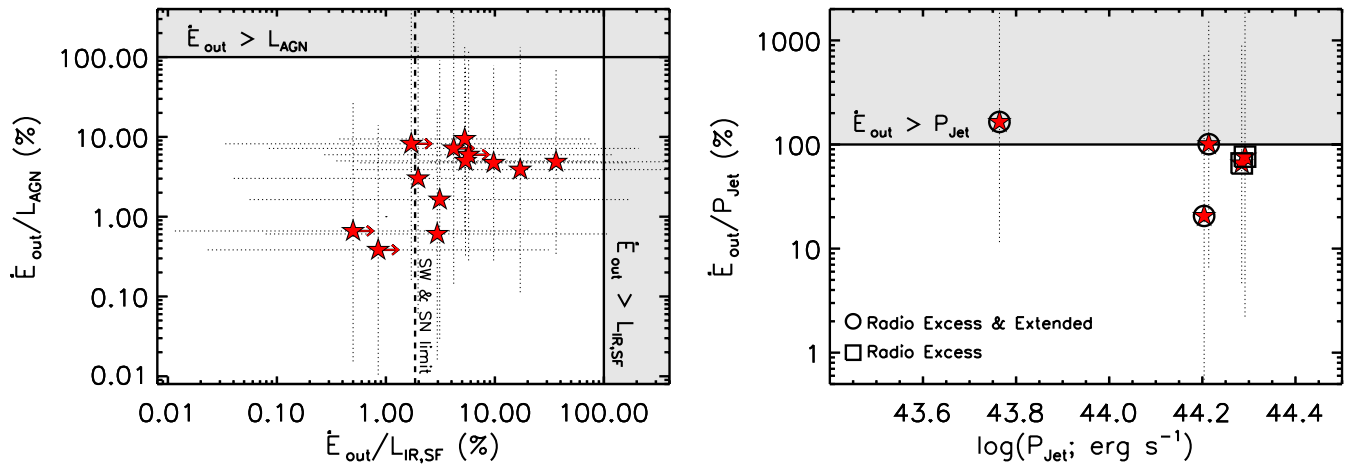
Figure 11. Left-hand panel: the ratio of our estimated outflow kinetic energy rates ($\dot{E}_{out}$; Section 4.3) to the AGN luminosity (ordinate) and to the star formation luminosity (abscissa) for the thirteen sources in our sample for which we estimated $\dot{E}_{out}$. The dotted lines illustrate the ratios from using our upper and lower bounds on the $\dot{E}_{out}$ values (Section 4.3). The shaded regions indicate where >100 per cent coupling efficiency is required between the input energy and the gas to power the outflows. The dashed vertical line is the estimated maximum mechanical input expected from supernovae and stellar winds (see Section 5.1). Right-hand panel: similar to the left-hand panel, but showing the ratio of $\dot{E}_{out}$ to the estimated jet power, as a function of jet power, for the five sources with the strongest evidence of hosting radio jets (see Section 2.4). Based on our simplifying assumptions a similar outflow coupling efficiency is required for AGN (i.e. ≈ 0.5–10 per cent) and star formation (i.e. $\gtrsim 0.5$–40 per cent); however, stellar winds and supernovae are less likely to be fully responsible for the observed outflows. Radio jets would require uncomfortably high coupling efficiencies to power the outflows in some cases (although see Section 5.1).

indicate in Fig. 11. Based on these assumptions, stellar winds and supernovae are unlikely to be fully responsible for the observed outflows. If we instead consider a momentum-driven wind with momentum deposition from the radiation pressure of stars, we expect $\dot{P}_{out} = \tau L_{SF,IR}/c$ (following Murray et al. 2005) that based on our calculations would require unrealistically high optical depths

(i.e. $\tau \gg 1$; see Fig. 12). Further investigation of the possibility that star formation drives the outflows could be achieved using high-resolution optical-continuum imaging to measure the SFR surface densities in our targets (e.g. Heckman et al. 2011; Murray, Ménard & Thompson 2011; Diamond-Stanic et al. 2012; Förster Schreiber et al. 2013).
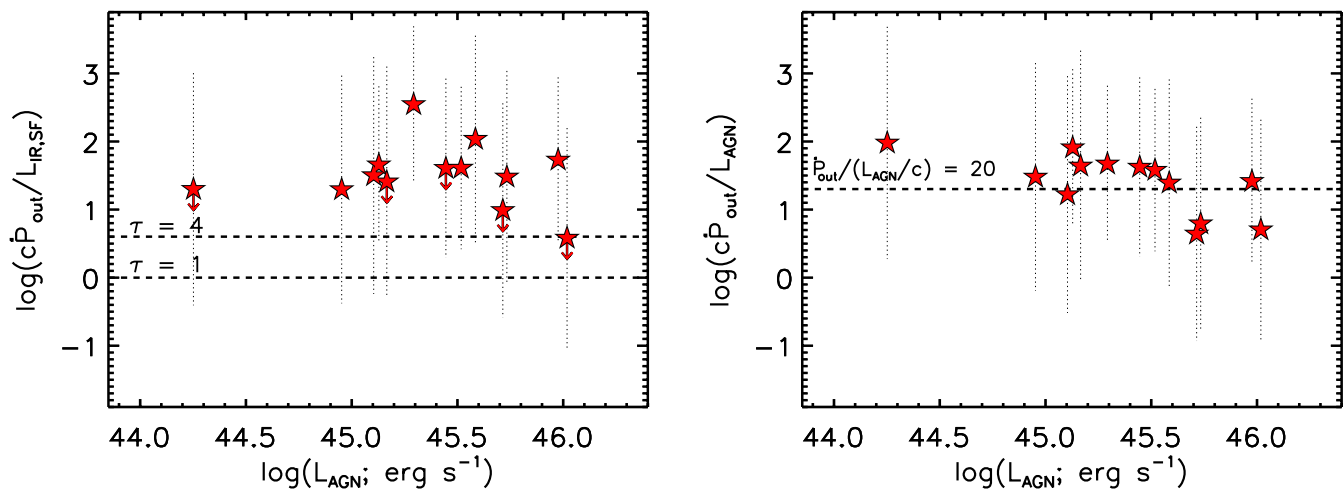
Figure 12. Left-hand panel: momentum rates of the outflows ($\dot{P}_{out}$) normalized to the star formation luminosity ($L_{IR,\,SF}/c$) versus AGN luminosity. The dashed lines represent the required optical depths if the outflows are driven by radiation pressure from star formation (see Section 5.1). Right-hand panel: momentum rate of the outflows normalized to the AGN luminosities (L_{AGN}/c) versus AGN luminosity. In both panels the vertical dotted lines represent the upper and lower bounds in $\dot{P}_{out}$ (see Section 4.3). Based on our assumptions, the outflows are unlikely to be purely radiatively driven but are broadly consistent with theoretical predictions of galactic-scale energy-driven outflows that are launched by an AGN accretion-disc wind (i.e. $\dot{P}_{out} \gtrsim 10$–$20L_{AGN}/c$; e.g. Zubovas & King 2012; Faucher-Giguère & Quataert 2012; Debuhr et al. 2012).

The estimated coupling efficiencies between the bolometric AGN luminosity and the outflows (i.e. ≈0.5–10 per cent) are consistent with those predicted by various models (e.g. Di Matteo et al. 2005; Hopkins & Elvis 2010; Debuhr et al. 2012; Zubovas & King 2012). However, we note that these coupling efficiencies do not tell us *how* the AGN couples to the gas. It is thought that direct radiation pressure from an AGN is unlikely to drive momentum-driven galaxy-wide outflows (e.g. King et al. 2011; Debuhr et al. 2012) and this is supported by the high outflow momentum rates we observe (Fig. 12). However, it has been predicted that for high accretion rate AGN, an accretion-disc wind could sweep up material and become a galaxy-wide energy-driven outflow (e.g. King et al. 2011; Debuhr et al. 2012; Faucher-Giguère & Quataert 2012; Zubovas & King 2012). These models predict momentum rates of $\dot{P}_{out} \approx 10$–$40L_{AGN}/c$ on ≈1–10 kpc scales that is in good agreement with our observations (Fig. 12) as well as multi gas-phase outflow observations of other AGN (e.g. Zubovas & King 2012; Cicone et al. 2014, and references there-in). An AGN could also couple to the gas in their host galaxies though the interaction of a radio jet with the ISM. In Fig. 11 we show that the coupling efficiencies between the radio jet power and the outflows is estimated to be ≈20–160 per cent (calculated for the sources with the strongest evidence for radio AGN activity only; see Section 2.4). These basic calculations may rule out radio jets being solely responsible for all of the outflows observed (Fig. 11; but see Appendix A for a discussion on the radio jets in individual objects); however, these numbers are uncertain and reasonably high coupling efficiencies are predicted for outflows driven by jet–ISM interactions [e.g. Wagner et al. (2012) predict ≈10–40 per cent].

In summary, based on our analyses we find no definitive evidence that the outflows we observe are universally driven by the AGN (either launched by accretion-disc winds or radio jets) or by star formation. However, using the arguments that we have presented we find that supernovae, stellar winds, radio jets or radiation pressure are unlikely to be solely responsible for all of the outflows that we observe. Although uncertain, we have shown that the outflows we observe have properties that are broadly consistent with

predictions of energy-conserving outflows that are initially driven by accretion-disc winds. It is certainly viable that multiple processes contribute to driving the observed outflows as has been seen in local systems, where star formation winds, nuclear winds (potentially AGN-driven) and radio jets all are playing a role (e.g. Cecil et al. 2001; Storchi-Bergmann et al. 2010; Rupke & Veilleux 2011; also see discussion on our individual targets in Appendix A). As has been highlighted throughout this section, multiphase (i.e. ionized, atomic and molecular) observations of the outflows, combined with high-resolution multiwavelength imaging will provide the required information to determine the relative role of these different outflow driving mechanisms in our targets.

5.2 What role do these outflows play in galaxy evolution?

Galaxy-wide outflows are required in galaxy formation models, driven by both star formation and AGN activity, to reproduce the observable properties of galaxies and the intergalactic medium (e.g. Silk & Rees 1998; Di Matteo et al. 2005; Dalla Vecchia & Schaye 2008; Hopkins et al. 2008, 2013a; Booth & Schaye 2010; Debuhr et al. 2012). In these models some fraction of the gas escapes from the potential of the host galaxy, regulating future star formation and BH growth and enriching the larger scale environment with metals. In this section we will assess what impact the outflows that we observe may have on the evolution of their host galaxies.

If we consider the estimated mass outflow rates (derived in Section 4.3) we find that they are ≈6–20 times greater than the SFRs of our targets [with one exception at 100 times (J1430+1339) and excluding upper limits]. These 'mass loading' values are typically higher than those observed in star-forming galaxies but similar to those seen in luminous AGN, derived from a variety of observations of outflows in different gas phases (e.g. Martin 1999; Heckman et al. 2000; Newman et al. 2012; Cicone et al. 2014). We do not know the multiphase outflowing gas properties of our targets; however, these observations imply that the star-forming material may be rapidly depleted, as has also been suggested from molecular gas

observations of a few nearby ULIRG-AGN composite galaxies (Cicone et al. 2014).

We can assess if the outflows will be able to escape the potential of their host galaxies. The escape velocities of typical type 2 AGN within the luminosity range of our sample are ≈ 500–$1000\,\mathrm{km\,s^{-1}}$ (assuming an isothermal sphere of mass out to 100 kpc; Greene et al. 2011). These escape velocities correspond to circular velocities of ≈ 200–$400\,\mathrm{km\,s^{-1}}$, which are likely to be representative of the intrinsic values for our galaxies, based on those in which we identify rotation (see Section 4.2.1). If we assume the intrinsic bulk velocities of the outflows are $v_{\mathrm{out}} = W_{80}/1.3$ (see Section 4.3) then we have a range of outflow velocities $v_{\mathrm{out}} = 510$–$1100\,\mathrm{km\,s^{-1}}$ (with a median of $780\,\mathrm{km\,s^{-1}}$) which are comparable to the escape velocities. The maximum projected velocities are even higher (up to $v_{02} \approx -1700\,\mathrm{km\,s^{-1}}$; Table 4). If we instead consider a $\approx 10^{11}\,\mathrm{M_\odot}$ galaxy inside a $\approx 10^{13}\,\mathrm{M_\odot}$ dark matter halo with Navarro–Frenk–White (Navarro, Frenk & White 1996) density profile, the gas is unlikely to escape unless it is travelling at $\gtrsim 1000\,\mathrm{km\,s^{-1}}$ (see the calculation in section 5.2 of Harrison et al. 2012). Indeed, some models have shown that even massive outflows may stall in the galaxy halo, re-collapse and cool at later times (along with new fuel supplies), resulting in re-ignition of star formation and BH growth (e.g. Lagos, Cora & Padilla 2008; Gabor et al. 2011; McCarthy et al. 2011; Hopkins et al. 2013b; Rosas-Guevara et al. 2013; see also Gabor & Bournaud 2014).

In summary, while it is not possible to constrain the ultimate fate of outflowing gas from observations, we have observed outflows with extremely high velocities and the estimated outflow kinetic energy rates (i.e. ≈ 0.5–10 per cent of L_{AGN}) and momentum rates ($\gtrsim 10$–$20 \times L_{\mathrm{AGN}}/c$) are in broad agreement with the requirements of models that invoke AGN-driven outflows to regulate star formation and BH growth in luminous AGN (e.g. Di Matteo et al. 2005; Hopkins & Elvis 2010; Debuhr et al. 2012). Even if the outflows do not escape the galaxy haloes, they may be the required pre-cursor to the postulated 'maintenance mode' of feedback that appears to be necessary to control the level of cooling in massive haloes at later times (e.g. Churazov et al. 2005; Gabor et al. 2011; McCarthy et al. 2011; Bower et al. 2012).

6 CONCLUSIONS

We have presented optical IFU observations covering the [O III] $\lambda\lambda4959$, 5007 and Hβ emission lines of 16 $z = 0.08$–0.2 type 2 AGN. Our targets were selected from a parent sample of $\approx 24\,000$ $z < 0.4$ AGN (Mullaney et al. 2013) and we demonstrate that they are representative of the 45 ±3 per cent of luminous ($L_{\mathrm{[OIII]}} \geq 5 \times 10^{41}\,\mathrm{erg\,s^{-1}}$) $z < 0.2$ type 2 AGN that have a significant fraction ($\gtrsim 30$ per cent) of their ionized gas outflowing (Section 2.1). The fraction of AGN with ionized outflows at lower levels will be much higher. We use infrared SED decomposition on our targets to derive SFRs ($\lesssim [10$–$100]\,\mathrm{M_\odot\,yr^{-1}}$) and AGN luminosities ($L_{\mathrm{AGN}} = 10^{44.3}$–$10^{46.0}\,\mathrm{erg\,s^{-1}}$) for our targets. We also show that the radio emission in our targets (luminosity range: $L_{1.4\,\mathrm{GHz}} \leq 10^{24.4}\,\mathrm{W\,Hz^{-1}}$) is due to a combination of star formation and other processes, with five targets showing a 'radio excess' above that expected from star formation and at least three of these showing spatially resolved radio emission (on scales $R_{1.4} \gtrsim 7$ kpc) that could be due to radio jets or shocks (Section 2.4). In summary, our targets are taken from a well-constrained parent sample and are not extreme star-forming systems or radio loud AGN that have been the focus of many similar studies.

The main results from our analysis are as follows.

(i) We find extended [O III] emission-line regions over the full field of view of our IFU observations (i.e. total extents of ≥ 10–20 kpc). In most of the sources these emission-line regions are circular or moderately elliptical; however, we observe some irregular morphologies, particularly in the radio excess sources (see Section 4.1).

(ii) By tracing narrow [O III] emission-line components across the field of view, we identify a range of kinematic features associated with galaxy dynamics including galaxy rotation, merger debris and double nuclei. We isolate these kinematic components from any kinematics due to outflows (see Section 4.2).

(iii) We find high-velocity and disturbed ionized gas (velocity widths of $W_{80} \approx 600$–$1500\,\mathrm{km\,s^{-1}}$) extended over $\gtrsim (6$–16) kpc in all of our targets. With our knowledge of the parent sample we conclude that, ≥ 70 per cent (3σ confidence level) of the outflow features observed in the [O III] emission-line profiles of $z < 0.2$ luminous type 2 AGN are extended on kiloparsec scales (see Section 4.2).

(iv) The bulk outflow velocities across the sample are $v_{\mathrm{out}} \approx 510$–$1100\,\mathrm{km\,s^{-1}}$, which are comparable to the galaxy escape velocities. The maximum projected gas velocities reach up to $v_{02} \approx 1700\,\mathrm{km\,s^{-1}}$ (see Section 4.2). These velocities indicate that ionized gas is currently being unbound from their host galaxies but it is not clear if it will permanently escape their host galaxy haloes (see Section 5.2).

(v) We observe a range of kinematic structure in the outflows including signatures of spherical outflows and bi-polar superbubbles. In several cases the outflows are preferentially oriented away from the plane of the host galaxy. We observe no obvious relationship between the outflow kinematic structures as a function of AGN luminosity, SFR or the presence or absence of radio AGN activity (see Sections 4.2 and 5.1). However, we do find that all of our three superbubble candidates are radio excess sources.

(vi) Based on our analyses we find that both star formation and AGN activity may contribute to driving the outflows that we observe, with no definitive evidence that favours one over the other in the sample as a whole; however, we discuss individual objects in more detail (see Section 5.1). By combining our observations with those from the literature, we show that kiloparsec-scale ionized outflows are not confined to the most luminous AGN, extreme star-forming galaxies or radio-loud AGN; however, we find that the most extreme ionized gas velocities (with maximum velocities: $v_{02} \gtrsim 2000\,\mathrm{km\,s^{-1}}$ and line widths $W_{80} \gtrsim 1500\,\mathrm{km\,s^{-1}}$) are preferentially found in quasar-ULIRG composite galaxies (see Section 5.1).

(vii) Although based on simplifying assumptions, we estimate kinetic energy outflow rates ($\dot{E}_{\mathrm{out}} \approx (0.15$–$45) \times 10^{44}\,\mathrm{erg\,s^{-1}}$) and mass outflow rates (typical $\approx 10 \times$ the SFRs) that imply that considerable mass and energy are being carried in the observed outflows (see Section 4.3).

(viii) It is not possible to provide *direct* evidence of the long-term impact of individual outflows; however, although uncertain, we find that the mass outflow rates, the outflow kinetic energy rates (≈ 0.5–10 per cent of L_{AGN}) and outflow momentum rates (typically $\gtrsim 10$–$20 \times L_{\mathrm{AGN}}/c$) are in broad agreement with theoretical predictions of AGN-driven outflows that are postulated to play significant role in shaping the evolution of galaxies (see Section 5.2).

In this paper, we have investigated the prevalence, properties and potential impact of galaxy-wide ionized outflows. By selecting targets for detailed observations from our well-constrained parent

sample we have been able to place our observations into the context of the overall AGN population. We have established that galaxy-wide ionized outflows are prevalent in AGN. Our investigation was based upon outflows of ionized gas since it is currently the only suitable gas phase for performing large statistical studies of outflows; however, it is imperative that we now obtain multi gas-phase observations of outflows from representative samples of objects, such as our targets, to fully characterize the properties and impact of galaxy-wide outflows in the global population.

ACKNOWLEDGEMENTS

REFERENCES

Abazajian K. N. et al., 2009, ApJS, 182, 543
Alatalo K. et al., 2011, ApJ, 735, 88
Alexander D. M., Hickox R. C., 2012, New Astron. Rev., 56, 93
Alexander D. M., Swinbank A. M., Smail I., McDermid R., Nesvadba N. P. H., 2010, MNRAS, 402, 2211
Allington-Smith J. et al., 2002, PASP, 114, 892
Antonucci R., 1993, ARA&A, 31, 473
Baldwin J. A., Carswell R. F., Wampler E. J., Boksenberg A., Smith H. E., Burbidge E. M., 1980, ApJ, 236, 388
Baldwin J. A., Phillips M. M., Terlevich R., 1981, PASP, 93, 5
Barbosa F. K. B., Storchi-Bergmann T., Cid Fernandes R., Winge C., Schmitt H., 2009, MNRAS, 396, 2
Barrows R. S., Sandberg Lacy C. H., Kennefick J., Comerford J. M., Kennefick D., Berrier J. C., 2013, ApJ, 769, 95
Barth A. J., Greene J. E., Ho L. C., 2008, AJ, 136, 1179
Becker R. H., White R. L., Helfand D. J., 1995, ApJ, 450, 559
Bennert N., Falcke H., Schulz H., Wilson A. S., Wills B. J., 2002, ApJ, 574, L105
Benson A. J., Bower R. G., Frenk C. S., Lacey C. G., Baugh C. M., Cole S., 2003, ApJ, 599, 38
Blustin A. J. et al., 2003, A&A, 403, 481
Booth C. M., Schaye J., 2010, MNRAS, 405, L1
Boroson T., 2005, AJ, 130, 381
Boroson T. A., Green R. F., 1992, ApJS, 80, 109
Boroson T. A., Persson S. E., Oke J. B., 1985, ApJ, 293, 120
Bower R. G., Benson A. J., Malbon R., Helly J. C., Frenk C. S., Baugh C. M., Cole S., Lacey C. G., 2006, MNRAS, 370, 645
Bower R. G., Benson A. J., Crain R. A., 2012, MNRAS, 422, 2816
Bradshaw E. J. et al., 2013, MNRAS, 433, 194
Brinchmann J., Kunth D., Durret F., 2008, A&A, 485, 657
Calzetti D., Armus L., Bohlin R. C., Kinney A. L., Koornneef J., Storchi-Bergmann T., 2000, ApJ, 533, 682
Cano-Díaz M., Maiolino R., Marconi A., Netzer H., Shemmer O., Cresci G., 2012, A&A, 537, L8
Capetti A., Axon D. J., Macchetto F. D., Marconi A., Winge C., 1999, ApJ, 516, 187

Cattaneo A. et al., 2009, Nature, 460, 213
Cavagnolo K. W., McNamara B. R., Nulsen P. E. J., Carilli C. L., Jones C., Bîrzan L., 2010, ApJ, 720, 1066
Cecil G., Bland-Hawthorn J., Veilleux S., Filippenko A. V., 2001, ApJ, 555, 338
Chabrier G., 2003, PASP, 115, 763
Chen C.-T. J. et al., 2013, ApJ, 773, 3
Churazov E., Sazonov S., Sunyaev R., Forman W., Jones C., Böhringer H., 2005, MNRAS, 363, L91
Cicone C. et al., 2014, A&A, 562, A21
Cimatti A. et al., 2013, ApJ, 779, L13
Cisternas M. et al., 2011, ApJ, 726, 57
Colina L., Arribas S., Borne K. D., 1999, ApJ, 527, L13
Comerford J. M., Gerke B. F., Stern D., Cooper M. C., Weiner B. J., Newman J. A., Madsen K., Barrows R. S., 2012, ApJ, 753, 42
Comerford J. M., Schluns K., Greene J. E., Cool R. J., 2013, ApJ, 777, 64
Condon J. J., Anderson E., Broderick J. J., 1995, AJ, 109, 2318
Condon J. J., Cotton W. D., Greisen E. W., Yin Q. F., Perley R. A., Taylor G. B., Broderick J. J., 1998, AJ, 115, 1693
Condon J. J., Kellermann K. I., Kimball A. E., Ivezić Ž., Perley R. A., 2013, ApJ, 768, 37
Courteau S., 1997, AJ, 114, 2402
Crenshaw D. M., Kraemer S. B., 2000, ApJ, 532, L101
Crenshaw D. M., Schmitt H. R., Kraemer S. B., Mushotzky R. F., Dunn J. P., 2010, ApJ, 708, 419
Cui J., Xia X.-Y., Deng Z.-G., Mao S., Zou Z.-L., 2001, AJ, 122, 63
Dalla Vecchia C., Schaye J., 2008, MNRAS, 387, 1431
Debuhr J., Quataert E., Ma C.-P., 2012, MNRAS, 420, 2221
Del Moro A. et al., 2013, A&A, 549, A59
Di Matteo T., Springel V., Hernquist L., 2005, Nature, 433, 604
Diamond-Stanic A. M., Moustakas J., Tremonti C. A., Coil A. L., Hickox R. C., Robaina A. R., Rudnick G. H., Sell P. H., 2012, ApJ, 755, L26
Dimitrijević M. S., Popović L. Č., Kovačević J., Dačić M., Ilić D., 2007, MNRAS, 374, 1181
Emonts B. H. C., Morganti R., Tadhunter C. N., Oosterloo T. A., Holt J., van der Hulst J. M., 2005, MNRAS, 362, 931
Fabian A. C., 1999, MNRAS, 308, L39
Fabian A. C., 2012, ARA&A, 50, 455
Faucher-Giguère C.-A., Quataert E., 2012, MNRAS, 425, 605
Feldman F. R., Weedman D. W., Balzano V. A., Ramsey L. W., 1982, ApJ, 256, 427
Feruglio C., Maiolino R., Piconcelli E., Menci N., Aussel H., Lamastra A., Fiore F., 2010, A&A, 518, L155
Fischer J. et al., 2010, A&A, 518, L41
Fischer T. C., Crenshaw D. M., Kraemer S. B., Schmitt H. R., Mushotsky R. F., Dunn J. P., 2011, ApJ, 727, 71
Fischer T. C., Crenshaw D. M., Kraemer S. B., Schmitt H. R., 2013, ApJS, 209, 1
Förster Schreiber N. M. et al., 2013, preprint (arXiv:1311.2596)
Fu H., Stockton A., 2009, ApJ, 690, 953
Fu H., Myers A. D., Djorgovski S. G., Yan L., 2011, ApJ, 733, 103
Fu H., Yan L., Myers A. D., Stockton A., Djorgovski S. G., Aldering G., Rich J. A., 2012, ApJ, 745, 67
Gabor J. M., Bournaud F., 2014, preprint (arXiv:1402.4482)
Gabor J. M., Davé R., Oppenheimer B. D., Finlator K., 2011, MNRAS, 417, 2676
Ganguly R., Brotherton M. S., 2008, ApJ, 672, 102
Gaspari M., Melioli C., Brighenti F., D'Ercole A., 2011, MNRAS, 411, 349
Ge J.-Q., Hu C., Wang J.-M., Bai J.-M., Zhang S., 2012, ApJS, 201, 31
Gelderman R., Whittle M., 1994, ApJS, 91, 491
Genzel R. et al., 2011, ApJ, 733, 101
Gofford J. et al., 2011, MNRAS, 414, 3307
Granato G. L., De Zotti G., Silva L., Bressan A., Danese L., 2004, ApJ, 600, 580
Greene J. E., Ho L. C., 2005, ApJ, 627, 721
Greene J. E., Zakamska N. L., Ho L. C., Barth A. J., 2011, ApJ, 732, 9
Greene J. E., Zakamska N. L., Smith P. S., 2012, ApJ, 746, 86

Gültekin K. et al., 2009, ApJ, 698, 198

Hainline K. N., Hickox R., Greene J. E., Myers A. D., Zakamska N. L., 2013, ApJ, 774, 145

Harrison C. M., 2013, preprint (arXiv:1312.3609)

Harrison C. M. et al., 2012, MNRAS, 426, 1073

Hatch N. A. et al., 2013, MNRAS, 436, 2244

Heckman T. M., Miley G. K., van Breugel W. J. M., Butcher H. R., 1981, ApJ, 247, 403

Heckman T. M., Miley G. K., Green R. F., 1984, ApJ, 281, 525

Heckman T. M., Armus L., Miley G. K., 1987, AJ, 93, 276

Heckman T. M., Armus L., Miley G. K., 1990, ApJS, 74, 833

Heckman T. M., Lehnert M. D., Strickland D. K., Armus L., 2000, ApJS, 129, 493

Heckman T. M., Kauffmann G., Brinchmann J., Charlot S., Tremonti C., White S. D. M., 2004, ApJ, 613, 109

Heckman T. M. et al., 2011, ApJ, 730, 5

Helou G., Soifer B. T., Rowan-Robinson M., 1985, ApJ, 298, L7

Hill M. J., Zakamska N. L., 2014, MNRAS, 439, 2701

Holt J., Tadhunter C., Morganti R., Bellamy M., González Delgado R. M., Tzioumis A., Inskip K. J., 2006, MNRAS, 370, 1633

Holt J., Tadhunter C. N., Morganti R., 2008, MNRAS, 387, 639

Holt J., Tadhunter C. N., Morganti R., Emonts B. H. C., 2011, MNRAS, 410, 1527

Hopkins P. F., Elvis M., 2010, MNRAS, 401, 7

Hopkins P. F., Hernquist L., Cox T. J., Di Matteo T., Robertson B., Springel V., 2006, ApJS, 163, 1

Hopkins P. F., Hernquist L., Cox T. J., Kereš D., 2008, ApJS, 175, 356

Hopkins P. F., Cox T. J., Hernquist L., Narayanan D., Hayward C. C., Murray N., 2013a, MNRAS, 430, 1901

Hopkins P. F., Kereš D., Murray N., Hernquist L., Narayanan D., Hayward C. C., 2013b, MNRAS, 433, 78

Humphrey A., Villar-Martín M., Sánchez S. F., Martínez-Sansigre A., Delgado R. G., Pérez E., Tadhunter C., Pérez-Torres M. A., 2010, MNRAS, 408, L1

Husemann B., Wisotzki L., Sánchez S. F., Jahnke K., 2013, A&A, 549, A43

Ivison R. J. et al., 2010, A&A, 518, L31

Keel W. C. et al., 2012, MNRAS, 420, 878

Kennicutt R. C., Jr, 1998, ARA&A, 36, 189

Kim D.-C., Sanders D. B., Veilleux S., Mazzarella J. M., Soifer B. T., 1995, ApJS, 98, 129

Kim M., Ho L. C., Lonsdale C. J., Lacy M., Blain A. W., Kimball A. E., 2013, ApJ, 768, L9

Kimball A. E., Ivezić Ž., 2008, AJ, 136, 684

King A., 2003, ApJ, 596, L27

King A. R., Zubovas K., Power C., 2011, MNRAS, 415, L6

Komossa S., Xu D., Zhou H., Storchi-Bergmann T., Binette L., 2008, ApJ, 680, 926

Kormendy J., Ho L. C., 2013, ARA&A, 51, 511

Kormendy J., Richstone D., 1995, ARA&A, 33, 581

Krajnović D., Cappellari M., de Zeeuw P. T., Copin Y., 2006, MNRAS, 366, 787

Lagos C. D. P., Cora S. A., Padilla N. D., 2008, MNRAS, 388, 587

Lawrence A., Elvis M., 2010, ApJ, 714, 561

Lehnert M. D., Heckman T. M., 1996, ApJ, 462, 651

Leipski C., Bennert N., 2006, A&A, 448, 165

Leitherer C. et al., 1999, ApJS, 123, 3

Lipari S. et al., 2009, MNRAS, 392, 1295

Lípari S. et al., 2009, MNRAS, 398, 658

Liu X., Shen Y., Strauss M. A., Greene J. E., 2010, ApJ, 708, 427

Liu G., Zakamska N. L., Greene J. E., Nesvadba N. P. H., Liu X., 2013a, MNRAS, 430, 2327

Liu G., Zakamska N. L., Greene J. E., Nesvadba N. P. H., Liu X., 2013b, MNRAS, 436, 2576

Liu G., Zakamska N. L., Greene J. E., 2014, preprint (arXiv:1401.0536)

McCarthy P. J., Baum S. A., Spinrad H., 1996, ApJS, 106, 281

McCarthy I. G. et al., 2010, MNRAS, 406, 822

McCarthy I. G., Schaye J., Bower R. G., Ponman T. J., Booth C. M., Dalla Vecchia C., Springel V., 2011, MNRAS, 412, 1965

McNamara B. R., Nulsen P. E. J., 2012, New J. Phys., 14, 055023

Magorrian J. et al., 1998, AJ, 115, 2285

Mahony E. K., Morganti R., Emonts B. H. C., Oosterloo T. A., Tadhunter C., 2013, MNRAS, 435, L58

Markwardt C. B., 2009, in Bohlender D. A., Durand D., Dowler P., eds, ASP Conf. Ser. Vol. 411, Astronomical Data Analysis Software and Systems XVIII. Astron. Soc. Pac., San Francisco, p. 251

Martin C. L., 1999, ApJ, 513, 156

Martin C. L., 2005, ApJ, 621, 227

Mateos S. et al., 2012, MNRAS, 426, 3271

Morganti R., Oosterloo T. A., Tadhunter C. N., van Moorsel G., Emonts B., 2005, A&A, 439, 521

Morganti R., Frieswijk W., Oonk R. J. B., Oosterloo T., Tadhunter C., 2013, A&A, 552, L4

Moshir M., Kopman G., Conrow T. A. O., 1992, in Moshir M., Kopman G., Conrow T. a. o., eds, IRAS Faint Source Survey, Explanatory Supplement Version 2. Calif. Inst. Technol., Pasadena

Mullaney J. R., Alexander D. M., Huynh M., Goulding A. D., Frayer D., 2010, MNRAS, 401, 995

Mullaney J. R., Alexander D. M., Goulding A. D., Hickox R. C., 2011, MNRAS, 414, 1082

Mullaney J. R. et al., 2012, ApJ, 753, L30

Mullaney J. R., Alexander D. M., Fine S., Goulding A. D., Harrison C. M., Hickox R. C., 2013, MNRAS, 433, 622

Murray N., Quataert E., Thompson T. A., 2005, ApJ, 618, 569

Murray N., Ménard B., Thompson T. A., 2011, ApJ, 735, 66

Navarro J. F., Frenk C. S., White S. D. M., 1996, ApJ, 462, 563

Nelson C. H., Whittle M., 1996, ApJ, 465, 96

Nesvadba N. P. H., Lehnert M. D., Eisenhauer F., Gilbert A., Tecza M., Abuter R., 2006, ApJ, 650, 693

Nesvadba N. P. H., Lehnert M. D., De Breuck C., Gilbert A., van Breugel W., 2007, A&A, 475, 145

Nesvadba N. P. H., Lehnert M. D., De Breuck C., Gilbert A. M., van Breugel W., 2008, A&A, 491, 407

Nesvadba N. P. H., Polletta M., Lehnert M. D., Bergeron J., De Breuck C., Lagache G., Omont A., 2011, MNRAS, 415, 2359

Neugebauer G. et al., 1984, ApJ, 278, L1

Newman S. F. et al., 2012, ApJ, 761, 43

Ohyama Y. et al., 2002, PASJ, 54, 891

Osterbrock D. E., 1989, Astrophysics of Gaseous Nebulae and Active Galactic Nuclei. Univ. Science Books, Mill Valley, CA

Osterbrock D. E., Ferland G. J., 2006, Astrophysics of Gaseous Nebulae and Active Galactic Nuclei. Univ. Science Books, Mill Valley, CA

Ramos Almeida C., Tadhunter C. N., Inskip K. J., Morganti R., Holt J., Dicken D., 2011, MNRAS, 410, 1550

Reeves J. N., O'Brien P. T., Ward M. J., 2003, ApJ, 593, L65

Reyes R. et al., 2008, AJ, 136, 2373

Richards G. T. et al., 2006, ApJS, 166, 470

Riffel R. A., Storchi-Bergmann T., Riffel R., 2014, ApJ, 780, L24

Rodríguez Zaurín J., Tadhunter C. N., Rose M., Holt J., 2013, MNRAS, 432, 138

Rosario D. J., Shields G. A., Taylor G. B., Salviander S., Smith K. L., 2010, ApJ, 716, 131

Rosario D. J. et al., 2012, A&A, 545, A45

Rosas-Guevara Y. M. et al., 2013, preprint (arXiv:1312.0598)

Rupke D. S. N., Veilleux S., 2011, ApJ, 729, L27

Rupke D. S. N., Veilleux S., 2013, ApJ, 768, 75

Rupke D. S., Veilleux S., Sanders D. B., 2005, ApJS, 160, 115

Sanders D. B., Mirabel I. F., 1996, ARA&A, 34, 749

Sanders D. B., Soifer B. T., Elias J. H., Neugebauer G., Matthews K., 1988, ApJ, 328, L35

Sargsyan L., Mickaelian A., Weedman D., Houck J., 2008, ApJ, 683, 114

Schirmer M., Diaz R., Holhjem K., Levenson N. A., Winge C., 2013, ApJ, 763, 60

Schnorr-Müller A., Storchi-Bergmann T., Nagar N. M., Robinson A., Lena D., Riffel R. A., Couto G. S., 2014, MNRAS, 437, 1708

Shen Y., Liu X., Greene J. E., Strauss M. A., 2011, ApJ, 735, 48

Shih H.-Y., Rupke D. S. N., 2010, ApJ, 724, 1430
Shih H.-Y., Stockton A., Kewley L., 2013, ApJ, 772, 138
Silk J., Rees M. J., 1998, A&A, 331, L1
Simpson C. et al., 2012, MNRAS, 421, 3060
Smith K. L., Shields G. A., Bonning E. W., McMullen C. C., Rosario D. J., Salviander S., 2010, ApJ, 716, 866
Smith K. L., Shields G. A., Salviander S., Stevens A. C., Rosario D. J., 2012, ApJ, 752, 63
Soto K. T., Martin C. L., 2010, ApJ, 716, 332
Springel V., Di Matteo T., Hernquist L., 2005, MNRAS, 361, 776
Stockton A., 1976, ApJ, 205, L113
Stockton A., MacKenty J. W., 1987, ApJ, 316, 584
Storchi-Bergmann T., Lopes R. D. S., McGregor P. J., Riffel R. A., Beck T., Martini P., 2010, MNRAS, 402, 819
Sutherland R. S., Bicknell G. V., 2007, ApJS, 173, 37
Swinbank A. M. et al., 2009, MNRAS, 400, 1121
Tadhunter C. N., Morganti R., Robinson A., Dickson R., Villar-Martin M., Fosbury R. A. E., 1998, MNRAS, 298, 1035
Tombesi F., Cappi M., Reeves J. N., Palumbo G. G. C., Yaqoob T., Braito V., Dadina M., 2010, A&A, 521, A57
Tremaine S. et al., 2002, ApJ, 574, 740
Veilleux S., 1991, ApJS, 75, 383
Veilleux S., Cecil G., Bland-Hawthorn J., Tully R. B., Filippenko A. V., Sargent W. L. W., 1994, ApJ, 433, 48
Veilleux S., Kim D.-C., Sanders D. B., Mazzarella J. M., Soifer B. T., 1995, ApJS, 98, 171
Veilleux S., Cecil G., Bland-Hawthorn J., 2005, ARA&A, 43, 769
Veilleux S. et al., 2009, ApJS, 182, 628
Veilleux S. et al., 2013, ApJ, 776, 27
Veron M. P., 1981, A&A, 100, 12
Villar-Martín M., Binette L., Fosbury R. A. E., 1999, A&A, 346, 7
Villar-Martín M., Tadhunter C., Humphrey A., Encina R. F., Delgado R. G., Torres M. P., Martínez-Sansigre A., 2011a, MNRAS, 416, 262
Villar-Martín M., Humphrey A., Delgado R. G., Colina L., Arribas S., 2011b, MNRAS, 418, 2032
Villar-Martín M., Cabrera Lavers A., Bessiere P., Tadhunter C., Rose M., de Breuck C., 2012, MNRAS, 423, 80
Vrtilek J. M., 1985, ApJ, 294, 121
Wagner A. Y., Bicknell G. V., Umemura M., 2012, ApJ, 757, 136
Wampler E. J., Burbidge E. M., Baldwin J. A., Robinson L. B., 1975, ApJ, 198, L49
Wang J.-M., Chen Y.-M., Hu C., Mao W.-M., Zhang S., Bian W.-H., 2009, ApJ, 705, L76
Wang J., Mao Y. F., Wei J. Y., 2011, ApJ, 741, 50
Wang L., Rowan-Robinson M., Norberg P., Heinis S., Han J., 2014, preprint (arXiv:1402.4991)
Weedman D. W., 1970, ApJ, 159, 405
Westmoquette M. S., Clements D. L., Bendo G. J., Khan S. A., 2012, MNRAS, 424, 416
Whittle M., 1985, MNRAS, 213, 1
Whittle M., 1992, ApJ, 387, 109
Whittle M., Wilson A. S., 2004, AJ, 127, 606
Whittle M., Pedlar A., Meurs E. J. A., Unger S. W., Axon D. J., Ward M. J., 1988, ApJ, 326, 125
Wilson A. S., Heckman T. M., 1985, in Miller J. S., ed., Astrophysics of Active Galaxies and Quasi-Stellar Objects. Univ. Science Books, Mill Valley, CA, p. 39
Wright E. L. et al., 2010, AJ, 140, 1868
Xu D., Komossa S., 2009, ApJ, 705, L20
Xu C., Livio M., Baum S., 1999, AJ, 118, 1169
York D. G. et al., 2000, AJ, 120, 1579
Zakamska N. L., Greene J. E., 2014, preprint (arXiv:1402.6736)
Zakamska N. L., Strauss M. A., Heckman T. M., Ivezić Ž., Krolik J. H., 2004, AJ, 128, 1002
Zakamska N. L., Gómez L., Strauss M. A., Krolik J. H., 2008, AJ, 136, 1607
Zhang K., Dong X.-B., Wang T.-G., Gaskell C. M., 2011, ApJ, 737, 71Z
Zubovas K., King A., 2012, ApJ, 745, L34
Zubovas K., King A., 2014, MNRAS, 439, 400

APPENDIX A: NOTES ON INDIVIDUAL SOURCES

In this appendix we provide some notes on individual sources by highlighting relevant previous multiwavelength observations from the literature and describing some of the key features in our IFU observations. The majority of these sources have received little or no attention previously in the literature, with the exceptions of J0945+1737, J1316+1753 and J1356+1026 that have been studied in some detail. The IFU data for all of our sources are displayed in this appendix (Fig. A1–A15), except for J1010+1413 that can be found in Figs 5 and 6 as it is used as an example in the main text.

J0945+1737. In agreement with our classifications (see Table 2) the source J0945+1737 has previously been identified as an LIRG with a type 2 AGN nucleus (Kim et al. 1995; Veilleux et al. 1995) and as a type 2 ('obscured') quasar by Reyes et al. (2008). It has been shown to have a single nucleus based upon *HST* observations (Cui et al. 2001). The infrared luminosity that we measure (Table 2) is consistent with previous measurements (Cui et al. 2001) and our AGN luminosity measurement is consistent with that derived from Spitzer infrared spectroscopy (Sargsyan et al. 2008). This source has evidence for a galaxy-scale radio jet due to its radio excess, above that expected from star formation, and the extended radio emission observed in FIRST ($R_{1.4} \approx 6.6$ kpc; see Section 2.4 and Table 2).

Our IFU data for this source are shown in Fig. A1. The [O III] peak velocity (v_p) field is irregular (Fig. A1) and therefore, based on these data alone, we do not attribute the v_p velocity field to galaxy rotation; however, we do note that the continuum image from our IFU data is elongated roughly in alignment with our kinematic 'major axis'. The high-velocity broad underlying wings in the [O III] emission-line profile are located over the full field of view ($\approx 8 \times 11$ kpc) but dominate in the central regions (with $W_{80} \approx 1100$ km s^{-1} and $\Delta v \approx -260$ km s^{-1}), preferentially located along an N–S axis (i.e. with a PA ≈ 0). This is not parallel to the radio axis based on the FIRST data (PA $\approx 110°$) that may disfavour a connection between a radio jet and the outflow; however, high-resolution radio data are required to accurately measure the morphology and origin of the radio emission.

J0958+1439. The IFU data for J0958+1439 are shown in Fig. A2. The data reveal that the 'flat-top' emission-line profile seen in the galaxy-integrated spectrum is primarily due to the sum of two luminous narrow kinematic components separated in velocity by ≈ 400 km s^{-1}, with the red component dominating in the south and the blue in the north. At the limit of our resolution (≈ 1.4 kpc) we do not see two separate continuum or emission-line regions. Additionally, the similarity of the Hβ and [O III] emission-line profiles indicate similar [O III]/Hβ ratios for each kinematic component (also seen in the velocity profile; Fig. A2) suggesting that the two kinematic components are illuminated by a single AGN. The kinematic 'major axis' we identify from the peak velocity (v_p) map is oriented parallel to the morphological major axis observed in the SDSS image and our continuum data (Fig. A2). Overall, we favour the interpretation that the v_p velocity map is tracing galaxy rotation, although we cannot rule out a late stage merger without higher spatial resolution imaging or spectroscopic data.

In addition to the narrow [O III] emission-line components there are underlying broad wings in the emission-line profile over the full field of view ($\approx 7 \times 10$ kpc; Fig. A2). These broad emission-line profiles (with $W_{80} \approx 850$ km s^{-1} and $\Delta v \approx -50$ km s^{-1}) are

more dominant perpendicular to the kinematic 'major axis'. This potentially indicates that the outflow is escaping away from a galactic disc. The emission-line flux ratio $\log([\text{O\,{\sc iii}}]/\text{H}\beta) \approx 1.1$ remains constant over the central $\approx 6\,\text{kpc}$ and then abruptly declines, in a similar manner to that seen in the type 2 quasars of Liu et al. (2013a; see Section 4.3). Therefore, to measure the outflow kinetic energy following Liu et al. (2013b) we adopt a value of $R_{\text{br}} = 3\,\text{kpc}$ and measure a Hβ surface brightness of $\Sigma_{\text{H}\beta} = 1.4 \times 10^{-15}\,\text{erg\,s}^{-1}\,\text{arcsec}^{-2}$ in an annulus at this radius (corrected for cosmological dimming). Using this method we obtain an outflow kinetic energy of $\dot{E} \approx 2.8 \times 10^{43}\,\text{erg\,s}^{-1}$, which is in excellent agreement with the value that we derive in Section 4.3 of $\dot{E}_{\text{out}} \approx 2.7 \times 10^{43}\,\text{erg\,s}^{-1}$.

J1000+1242. Reyes et al. (2008) previously identified J1000+1242 as a type 2 ('obscured') quasar. This source has excess radio emission (above that expected from star formation; Table 2) that is marginally resolved based on the FIRST data ($R_{1.4} \approx 8.4\,\text{kpc}$ with a PA $\approx 160°$; see Section 2.4 and Table 2). Although fairly irregular, our IFU data reveal a velocity gradient from blue to red in the peak of the [O\,{\sc iii}] emission-line profile ($\Delta v_{\text{p}} \approx 200\,\text{km\,s}^{-1}$) at a PA of $\approx 240°$ (Fig. A3). The peak S/N map, combined with the velocity maps reveal a distinct luminous emission-line region $\approx 3.5\,\text{kpc}$ north-east of the nucleus that has a reasonably narrow emission-line profile ($W_{80} \lesssim 600\,\text{km\,s}^{-1}$). This feature may be merger debris, halo gas or an outflow remnant (see Section 4.2.1).

Roughly perpendicular to the v_{p} velocity gradient (with a PA $\approx 160–170°$) we observe regions with broad underlying wings (with $W_{80} \approx 850\,\text{km\,s}^{-1}$) in the [O\,{\sc iii}] emission-line profile. From the spectra in boxes 12, 17 and 18 in Fig. A3 it can be seen that this broad emission is built up from multiple narrow components. This emission shows a velocity shift from blue (with $\Delta v \approx -100\,\text{km\,s}^{-1}$) to red (with $\Delta v \approx 100\,\text{km\,s}^{-1}$) over $\approx 10–15\,\text{kpc}$. We also see an irregular morphology of the emission-line region. All of the above indicates that we are observing an outflowing bi-polar superbubble, with a strikingly similar kinematic structure to previously identified superbubbles (i.e. J1356+1026 from Greene et al. 2012; J0319−0019 from Liu et al. 2013b; and Mrk 273 from Rupke & Veilleux 2013). The PA of the superbubbles we observe in J1000+1242 is parallel to the axis of the extended radio emission and found over a similar spatial extent, potentially demonstrating a direct connection between a radio jet and the outflow, although shock-induced radio emission is another possibility. The SDSS image of this source (Fig. A3) is extended beyond the field of view of our observations and therefore IFU observations over larger regions are required to trace the full kinematic structure of this target.

J1010+1413. We show our IFU data for J1010+1413 in Figs 5 and 6. This source has the broadest [O\,{\sc iii}] emission-line width of the entire sample ($W_{80} = 1450\,\text{km\,s}^{-1}$) and is kinematically complex. In the central regions we observe a smooth gradient from red to blue in the [O\,{\sc iii}] peak velocity (v_{p}; Fig. 6), although the overall velocity field is irregular (Fig. 5). There are luminous narrow [O\,{\sc iii}] emission-line components located to the north and south of the nucleus, separated by $\approx 16\,\text{kpc}$ in projected distance and $\approx 350\,\text{km\,s}^{-1}$ in projected velocity, that appear to be associated with emission-line regions that are apparent in the SDSS image (Fig. 6). These features may be merger debris, halo gas or outflow remnants (see Section 4.2.1). The extremely broad emission-line profiles, with velocity offsets reaching up to $\Delta v \approx -350\,\text{km\,s}^{-1}$, are located out to the very edge of the field of view (i.e. over $\gtrsim 16\,\text{kpc}$).

J1010+0612. Reyes et al. (2008) previously identified J1010+0612 as a type 2 ('obscured') quasar. This source has a clear radio excess above that expected from star formation alone (Table 2). Based on the FIRST data we do not spatially resolve any radio emission on scales $\gtrsim 2$ arcsec (see Section 2.4 and Table 2).

We show our IFU data for this object in Fig. A4. We identify a regular blue to red velocity field, indicative of galactic rotation, in the [O\,{\sc iii}] peak velocity (with $\Delta v_{\text{p}} \approx 300\,\text{km\,s}^{-1}$). Broad underlying wings lead to emission-line widths of $W_{80} \approx 1100 - 1300\,\text{km\,s}^{-1}$ and velocity offsets of $\Delta v \approx -100\,\text{km\,s}^{-1}$ and are located over the full extent of the field of view ($\approx 6 \times 9\,\text{kpc}$) with a roughly circular morphology.

J1100+0846. Reyes et al. (2008) previously identified J1100+0846 as a type 2 ('obscured') quasar and we show our IFU data for this object in Fig. A5. Although the peak velocity (v_{p}) map shows some irregular features we see a smooth velocity gradient ($\Delta v_{\text{p}} \approx 100\,\text{km\,s}^{-1}$) along a PA $\approx 250°$. Additionally, this kinematic 'major axis' is parallel to the morphological major axis seen in the SDSS image (with hints of the same axis in our continuum image), providing evidence that kinematics due to galaxy rotation are being observed. Broad wings (leading to $W_{80} \approx 700–1100\,\text{km\,s}^{-1}$) are observed in the emission-line profiles over the full field of view ($\approx 9 \times 6\,\text{kpc}$). The uncertainties on the velocity offset of the broad emission (i.e. Δv) are large; however, the velocity seems to be highest in the southern regions with velocities between $\Delta v \approx -100$ and $-80\,\text{km\,s}^{-1}$. These blueshifted velocities could indicate the near-side of an outflow that is moving away from the almost face on galaxy disc. In the velocity profile (Fig. A5), we observe that the emission-line flux ratio of $\log([\text{O\,{\sc iii}}]/\text{H}\beta) \approx 1.0–1.1$ is constant over the central regions then declines at a break radius of $R_{\text{br}} = 2.5\,\text{kpc}$ (see Section 4.3). We therefore measure a Hβ surface brightness of $\Sigma_{\text{H}\beta} = 1.7 \times 10^{-15}\,\text{erg\,s}^{-1}\,\text{arcsec}^{-2}$ in an annulus at this break radius (corrected for cosmological dimming) and calculate the outflow kinetic energy following Liu et al. (2013b). The kinetic outflow energy we obtain using this method, i.e. $\dot{E} \approx 6.3 \times 10^{43}\,\text{erg\,s}^{-1}$, is in excellent agreement with the value that we calculate in Section 4.3, i.e. $\dot{E}_{\text{out}} \approx 6.9 \times 10^{43}\,\text{erg\,s}^{-1}$.

J1125+1239. We show our IFU observations for J1125+1239 in Fig. A6. We observe an emission-line region that is extended right to the edges of the field of view (over $\gtrsim 13\,\text{kpc}$). We do not observe any velocity gradients in the peak of the [O\,{\sc iii}] emission-line profile (i.e. v_{p}; Fig. A6). There is faint, high-velocity ($\Delta v \approx -250$ to $-300\,\text{km\,s}^{-1}$) and extremely broad [O\,{\sc iii}] emission ($W \approx 1200–1500\,\text{km\,s}^{-1}$), out to the very edges of the field of view. Due to the low surface brightness the morphology of the broad emission is uncertain; however, the SDSS image shows faint extended emission beyond the IFU field of view, parallel to the axis where we predominantly observe this broad emission (i.e. PA $\approx 250°$; Fig. A6).

J1130+1301. We show our IFU observations for J1130+1301 in Fig. A7. The peak velocity map (v_{p}) is indicative of galactic rotation showing a smooth velocity gradient from red to blue with $\Delta v_{\text{p}} \approx 300\,\text{km\,s}^{-1}$. This interpretation is strengthened by the kinematic major axis being aligned with the morphological major axis observed in the SDSS image and the continuum observed in our data. The broad emission-line wings (with $W_{80} > 600\,\text{km\,s}^{-1}$) are found perpendicular to the galaxy major axis over $\approx 8\,\text{kpc}$. Although both blue and red wings are observed in the emission-line profile

the red wing is more luminous resulting in an overall velocity offset that is positive (i.e. $\Delta v \approx 150\,\mathrm{km\,s^{-1}}$).

J1216+1417. Spectroscopy of J1216+1417 has previously identified that Wolf–Rayet stars are located in this source and consequently shows that a recent star formation episode has occurred (i.e. ≈ 2–5 Myr; Brinchmann, Kunth & Durret 2008). Furthermore, a subtle 4000 Å break and stellar absorption features are seen in the SDSS spectrum and may explain why the Hβ emission-line profile is different to that seen in [O III] (Fig. A8). We show our IFU data in Fig. A8. We see little velocity structure in the $v_{\rm p}$ velocity map. The [O III] emission-line profile is irregular, with both a blue wing (out to $v \approx 1000\,\mathrm{km\,s^{-1}}$) and a large red wing out to $v \approx 2000\,\mathrm{km\,s^{-1}}$. This is seen in both lines of the [O III] $\lambda\lambda 4959,5007$ emission-line doublet indicating that it is a true [O III] feature associated with this source. Further kinematic analysis, beyond the scope of this work, is required to fully identify the origin of these high-velocity wings. The blue and red wings observed in the [O III] emission line are predominantly found in a circular region across the central $\gtrsim 6\,\mathrm{kpc}$; however, the low surface brightness of the emission in the outer regions puts some uncertainty on the spatial extent and morphology.

J1316+1753. The target J1316+1753 has a double peaked [O III] emission-line profile, with components separated by ≈ 400–$500\,\mathrm{km\,s^{-1}}$ (Fig. A9). As a result of this, this source has previously been identified as a dual AGN candidate (Xu & Komossa 2009; also see Section 4.2.1). In the peak S/N map we observe two spatial regions separated by ≈ 2–3 kpc and orientated with a PA $\approx 130°$ associated with these kinematics components; however, at the resolution of our observations ($\approx 2\,\mathrm{kpc}$) we do not observe two continuum peaks (Fig. A9). The similarity of the emission-line ratios in both systems, and the lack of a double continuum source, suggests that these kinematic components may be illuminated by a single ionizing source. Also, the kinematic components have similar fluxes and the velocities are independent of projected distance from the centre; therefore, the double-peaked profile may by the result of gas kinematics, jet interactions and/or AGN-driven outflows (Fig. A9; also see Xu & Komossa 2009; Smith et al. 2010; Barrows et al. 2013). The lack of evidence for extended luminous radio emission on $\gtrsim 2$ arcsec scales from the FIRST data (Table 2) could argue against a jet interaction (as seen in other sources e.g. Rosario et al. 2010); however, deep and high-resolution radio data would be required to confirm this. Additionally the axis of the two components is aligned with the morphological major axis seen in the SDSS image and the continuum emission seen in our data (Fig. A9). Overall, all of these observations favour the scenarios of a rotating gas disc or two merging components (separated by $\lesssim 2\,\mathrm{kpc}$) illuminated by a single AGN to explain the double peaked [O III] emission-line profile in this source (also see Smith et al. 2012 and Comerford et al. 2012). Combining these IFU data with deep high spatial resolution optical, X-ray and radio images would provide the data required to robustly distinguish between all of the possible scenarios.

In addition to the narrow components our IFU data for J1316+1753 (Fig. A9) reveal a very broad [O III] emission-line profile ($W_{80} \approx 1100$–$1200\,\mathrm{km\,s^{-1}}$), preferentially located perpendicular to the kinematic 'major axis' defined from the $v_{\rm p}$ map. This [O III] emission has a velocity offset of $\Delta v \approx -200\,\mathrm{km\,s^{-1}}$ and is extended right to the edge of the field of view (i.e. over $\gtrsim 14\,\mathrm{kpc}$).

In the velocity profile, we observe an emission-line flux ratio $\log([\mathrm{O\,III}]/\mathrm{H}\beta) \approx 1.0$–1.1 over the central regions and that declines at a break radius of $R_{\rm br} = 5\,\mathrm{kpc}$ (see Section 4.3). Therefore, we measure a Hβ surface brightness of $\Sigma_{\mathrm{H}\beta} = 6.2 \times 10^{-16}\,\mathrm{erg\,s^{-1}\,arcsec^{-2}}$ in an annulus at this break radius (corrected for cosmological dimming) and measure the outflow kinetic energy following Liu et al. (2013b). Following this method we obtain an outflow kinetic energy of $\dot{E} \approx 5.4 \times 10^{43}\,\mathrm{erg\,s^{-1}}$ that is within a factor of 3 of the value we calculated in Section 4.3, i.e. $\dot{E}_{\rm out} \approx 1.7 \times 10^{44}\,\mathrm{erg\,s^{-1}}$.

J1338+1503. We show our IFU data for J1338+1503 in Fig. A10. We note that hints of stellar continua are seen in the SDSS spectrum and contamination from stellar absorption may cause the difference in the Hβ and [O III] emission-line profiles (Fig. A10). The peak velocity map ($v_{\rm p}$) for J1338+1503 is irregular; however, we do see a general shift from blue to red. This source has a predominantly red wing, in addition to a weaker blue wing leading to an overall velocity offset of $\Delta v \approx 120\,\mathrm{km\,s^{-1}}$ across the central few kiloparsecs. The broad emission ($W_{80} \approx 900\,\mathrm{km\,s^{-1}}$) is preferentially found perpendicular to the velocity gradient (i.e. the kinematic 'major axis') that we observe in $v_{\rm p}$ (Fig. A10).

J1339+1425. The source J1339+1425 is the least luminous AGN in our sample (in both $L_{\rm AGN}$ and $L_{[\mathrm{O\,III}]}$) and is the only source not detected at 1.4 GHz by FIRST or NVSS (Table 2). We show our IFU data for this source in Fig. A11 where we observed [O III] emission right to the edge of the field of view of our observations (i.e. over $\gtrsim 12\,\mathrm{kpc}$). This emission-line region is dominated by narrow kinematic components (i.e. with $W_{80} < 600\,\mathrm{km\,s^{-1}}$) that trace out a small velocity gradient ($\Delta v_{\rm p} \approx 100\,\mathrm{km\,s^{-1}}$) from blue to red. We find that the kinematic major axis is broadly consistent with the continuum morphological axis observed in our data and the SDSS image (Fig. A11). We therefore appear to be tracing galactic rotation in the $v_{\rm p}$ map.

Across the central $\approx 6\,\mathrm{kpc}$ we observe a blue and red wing in the [O III] emission-line profile, with an overall velocity offset of $\Delta v \approx 150\,\mathrm{km\,s^{-1}}$, that is preferentially located at $\approx 50°$–$70°$ away from this kinematic 'major axis'. In the velocity profile, we observe that the emission-line flux ratio $\log([\mathrm{O\,III}]/\mathrm{H}\beta) \approx 1.1$ is constant over the central regions and then declines at a break radius of $R_{\rm br} = 2\,\mathrm{kpc}$ (see Section 4.3). We therefore measure a Hβ surface brightness of $\Sigma_{\mathrm{H}\beta} = 7.5 \times 10^{-16}\,\mathrm{erg\,s^{-1}\,arcsec^{-2}}$ in an annulus at this break radius (corrected for cosmological dimming) and calculate the outflow kinetic energy following Liu et al. (2013b). Using this method we obtain an outflow kinetic energy of $\dot{E} \approx 5.5 \times 10^{42}\,\mathrm{erg\,s^{-1}}$ that is within a factor of ≈ 3 of the value we calculated in Section 4.3, i.e. $\dot{E}_{\rm out} \approx 1.5 \times 10^{43}\,\mathrm{erg\,s^{-1}}$.

J1355+1300. We show our IFU data for J1355+1300 in Fig. A12. The majority of the emission-line region is dominated by narrow [O III] emission-line profiles ($W_{80} \approx 300$–$400\,\mathrm{km\,s^{-1}}$) and we observe a small velocity gradient (with $\Delta v_{\rm p} \approx 100\,\mathrm{km\,s^{-1}}$) from blue to red in a north–south direction in the peak velocity map ($v_{\rm p}$) indicative of galactic rotation. Located $\approx 3\,\mathrm{kpc}$ to the south-east of the nucleus there is a distinct kinematic component with a velocity between ≈ -500 and $-600\,\mathrm{km\,s^{-1}}$ which has a high-velocity blue wing in the emission-line profile (see grids of spectra in Fig. A12). The similarity of the galaxy-integrated [O III] and Hβ emission-line ratios for this kinematic component (see Fig. A12) could imply that the ionizing source is the same as that for the rest of the emission-line region and is therefore likely to be illuminated by the central source. At the depth of our observations, we observe no spatially

distinct continuum source or emission-line region coincident with this kinematic component (Fig. A12). The exact origin of this high-velocity feature is difficult to determine with these observations alone; however, the highly disturbed nature and lack of associated continuum strongly suggests an outflow. This feature is similar to that seen in J1430+1339 and therefore could indicate a smaller scale outflowing bubble and/or could be due to a jet–ISM interaction at this position (as is seen in other sources, e.g. Emonts et al. 2005). Due to the faintness of the radio emission, and the lack of *IRAS* detections we are unable to constrain the radio excess parameter for this source (see Section 2.4 and Table 2); therefore, deep and high-resolution radio imaging is required to determine if radio jets are present and if they are aligned with this high-velocity feature.

J1356+1026. As a well-known type 2 ('obscured') quasar (Reyes et al. 2008) this source has already received a lot of attention in the literature. Two merging galactic nuclei with a projected separation of ≈ 2.5 kpc are seen in the optical and near-infrared (Fu et al. 2011; Shen et al. 2011; Greene et al. 2012). In agreement with this, our IFU data reveal two continuum sources and, moderately offset from this, corresponding emission-line regions with distinct velocities (Fig. A13). We note that Fu et al. (2012) did not confidently associate an emission-line region with the southern nucleus in their IFU data, although our data are unambiguous (Figs 7 and A13). Combined with the observation that these kinematic components have slightly different [O III]/Hβ emission-line flux ratios implies two distinct type 2 quasars (Fig. A13; also see Greene et al. 2012). This source has a clear radio excess above that expected from star formation alone (see Section 2.4 and Table 2). However, there is no evidence for *extended* radio emission at the few mJy level on scales of $\gtrsim 2$ arcsec based on the FIRST data (Section 2.4; Table 2).

Using longslit observations, Greene et al. (2012) revealed [O III] emission extended over tens of kiloparsecs, reaching beyond the field of view of our IFU observations. In particular they reveal a 'bubble' of [O III] emission with a spatial extent of 12 kpc to the south and high-velocity 'clumps' to the north. These 'bubble' and 'clumps' reach a projected velocity of ≈ 250 km s^{-1}. Greene et al. (2012) postulate a quasi-spherical outflow that extends from the south to the north, where the outflow is forced into this bi-polar shape due to high-density regions of gas and dust in the central galaxies (e.g. Faucher-Giguère & Quataert 2012). Our IFU observations (Fig. A13) cover the base of these features. It is worth noting that despite our lack of spatial coverage and different approaches, our outflow energy injection rate estimate ($\dot{E}_{out} \approx 1.3 \times 10^{44}$ erg s^{-1}; Section 4.3) is consistent with the fiducial range $= 10^{44}$–10^{45} erg s^{-1} quoted in Greene et al. (2012). Based on our SED fitting (Section 2.4) the bolometric luminosity of the AGN in this source is $\approx 1 \times 10^{45}$ erg s^{-1} while the infrared luminosity from star formation is $\approx 2 \times 10^{45}$ erg s^{-1} (SFR ≈ 60 M$_\odot$ yr^{-1}; Table 2). Therefore, in contrast to the conclusions of Greene et al. (2012) we find there is a comparable amount of energy available from the AGN and star formation to power the outflow. The observed radio emission in FIRST is on much smaller scales than the ≈ 10 kpc outflowing bubble that may argue against a jet-driven outflows; however, deep and high-resolution radio imaging is required to determine the origin and morphology of the radio emission in this source.

J1430+1339. Reyes et al. (2008) previously identified J1430+1339 as a type 2 ('obscured') quasar. Additionally, this source was identified by Galaxy Zoo (Keel et al. 2012) as having an extended emission-line region, due to the arc shaped 'purple haze' to the north-east of the SDSS image (Fig. A14). This galaxy has consequently received the nickname the 'Teacup'. Follow-up *HST* imaging[17] has revealed that this is actually a 5–10 kpc emission-line 'loop' accompanied by a smaller emission-line 'arc' on the opposite side of the nucleus, potentially analogous to the bi-polar outflow observed in J1356+1026 (Fig. A13; Greene et al. 2012). The exact origin of these emission-line regions are unknown; however, our IFU data (Fig. A14) cover the base of the north-east loop and reveal it has a velocity of ≈ -900 km s^{-1} from the systemic with a high-velocity tail out to ≈ -1400 km s^{-1}. The [O III] peak S/N map shows faint extended features similar to those seen in outflowing superbubbles (e.g. Liu et al. 2013b). Additionally these features look remarkably similar to the bi-conal shells of ionized gas seen in the high-redshift radio galaxy MRC 0406$-$244 that appear to be due to gas that has been expelled from the host galaxy by radio jets and/or star formation (Hatch et al. 2013; see also Nesvadba et al. 2008). Indeed, the PAs of these high-velocity ionized gas features in J1430+1339 are roughly aligned with, and found over a similar scale to, the extended radio emission seen in the FIRST data (see Section 3 and Table 2). High-resolution radio imaging of this source will play a crucial role in determining the true origin of the radio emission (e.g. radio jets or shocks). IFU observations covering the full extent of the emission-line region will reveal the full velocity structure in these regions. The peak velocity (v_p) map shows a large velocity gradient from blue to red ($\Delta v_p \approx 600$ km s^{-1}) along an axis with PA $\approx 30°$ (Fig. A14).

J1504+0151. Reyes et al. (2008) previously identified this source as being a type 2 ('obscured') quasar. We note that there are stellar continuum and absorption features visible in the SDSS spectrum of this source and therefore contamination from stellar absorption may result in the different Hβ and [O III] emission-line profiles (Fig. A15). This source is one of the faintest in our sample; however, we still observe an [O III] emission-line region out to the edges of the field of view (i.e. over $\gtrsim 13$ kpc; Fig. A15). The peak velocity map (v_p) shows a smooth velocity gradient from blue to red (with $\Delta v_p \approx 150$ km s^{-1}) indicative of galaxy rotation with a PA $\approx 140°$. Due to the faint emission lines, it is difficult to establish the true extent and morphology of the broad, high-velocity emission (which has $W_{80} \approx 1000$ km s^{-1} and a velocity offset between $\Delta v \approx -300$ and -500 km s^{-1}); however, it appears to dominate in the central few kiloparsecs (Fig. A15).

---

[17] http://blog.galaxyzoo.org/2012/06/14/hubble-spies-the-teacup-and-i-spy-hubble
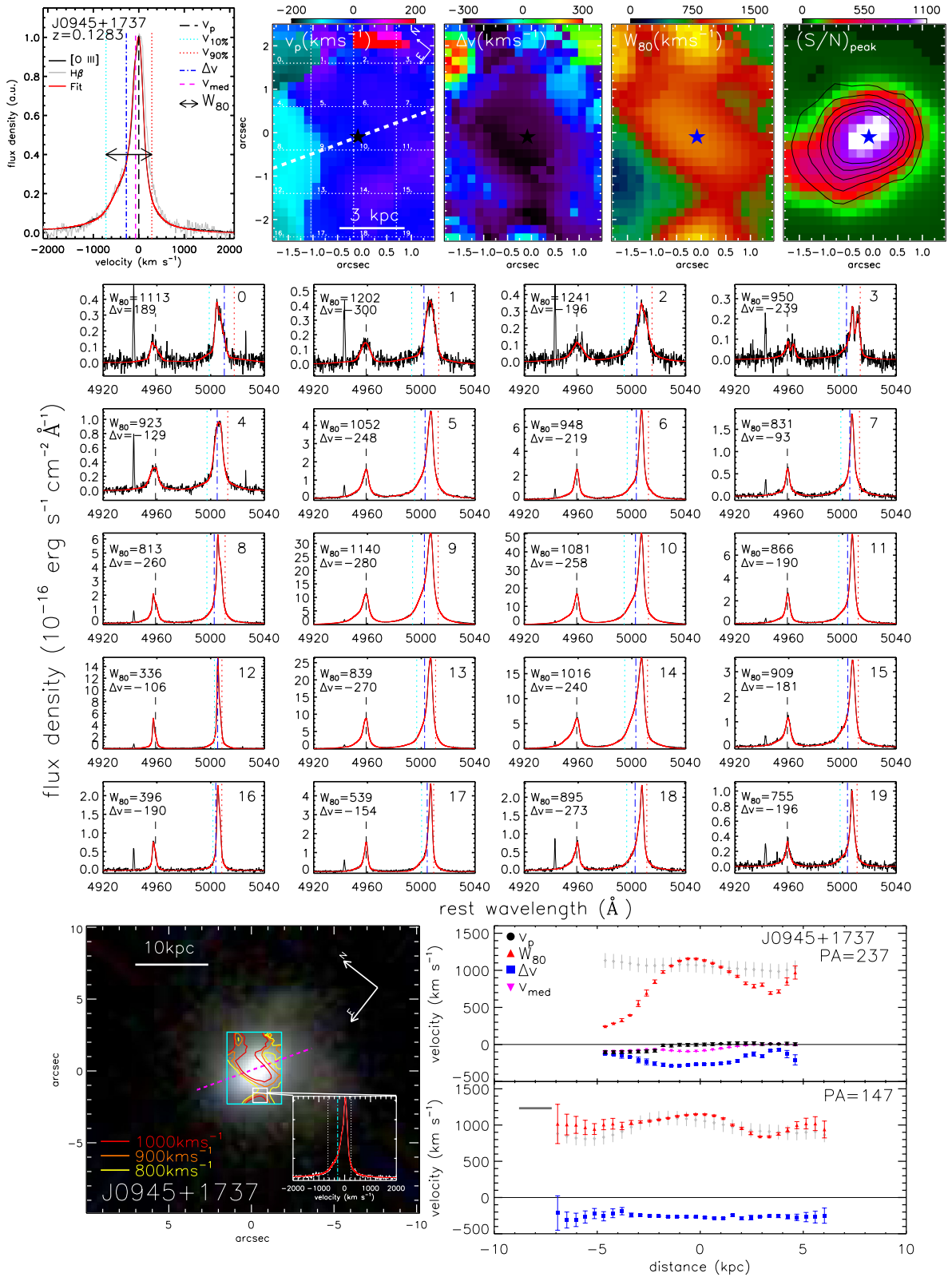
Figure A1. Our IFU data for SDSS J0945+1737. In summary (see captions in Figs 5 and 6 for a full description), top row from left to right: panel 1: galaxy-integrated [O III] λ5007 and Hβ emission-line profiles. Panel 2: velocity map of the peak in the [O III] emission-line profile (v_p). Panel 3: map of the velocity offset (Δv) of the broad [O III] emission-line wings. Panel 4: [O III] line-width (W_{80}) map. Panel 5: map of the S/N of the peak in the [O III] emission-line profile. The grid of panels shows [O III] $\lambda\lambda$4959, 5007 emission-line profiles extracted from the spatial regions illustrated in panel panel 2. Bottom left: SDSS image with contours overlaid of constant W_{80} from our IFU data. Bottom right: velocity-distance profiles along the 'major axis' shown in panel 2 and an axis perpendicular to this major axis.
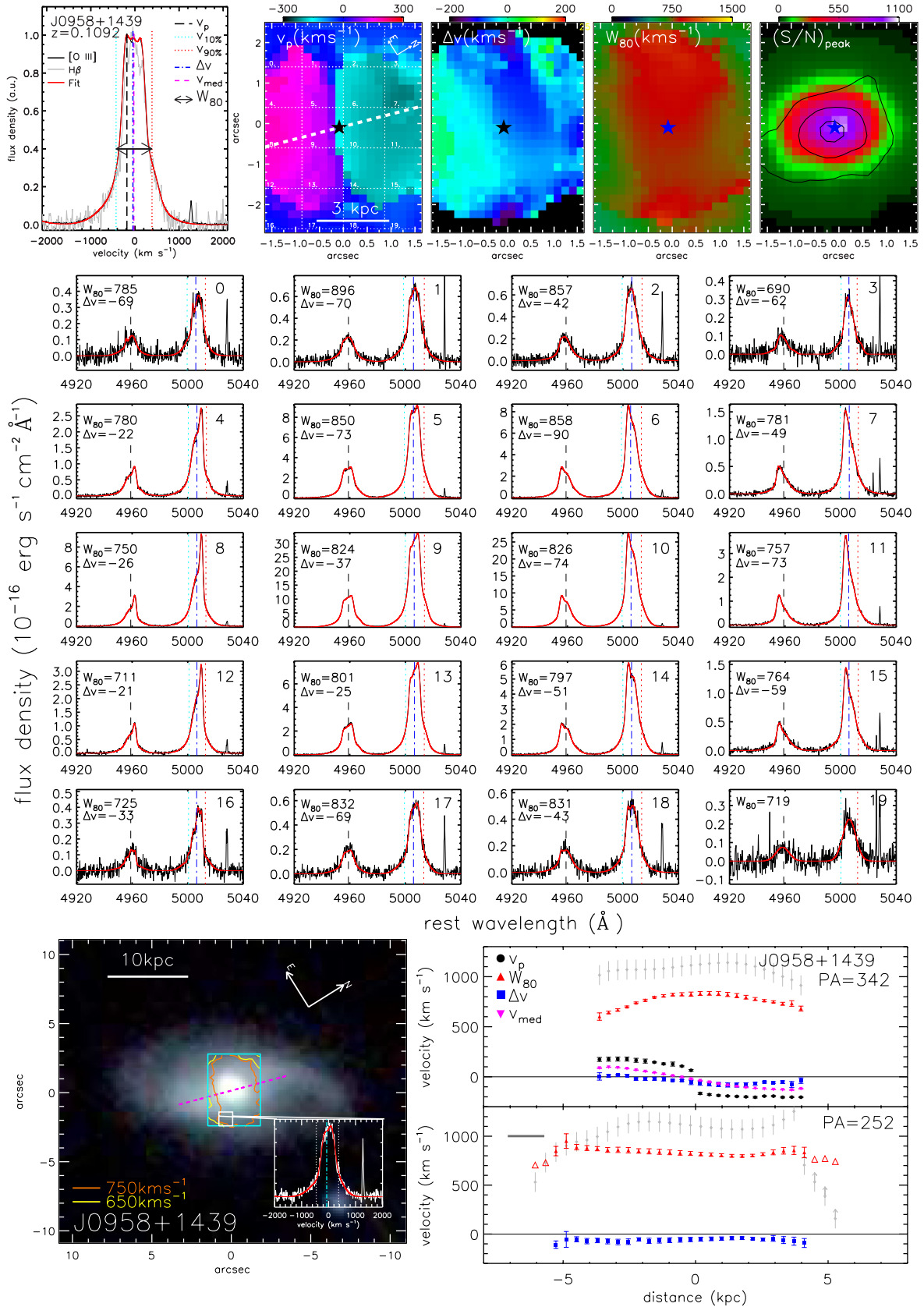
Figure A2. Same as Figs 5 and 6 but for SDSS J0958+1439.
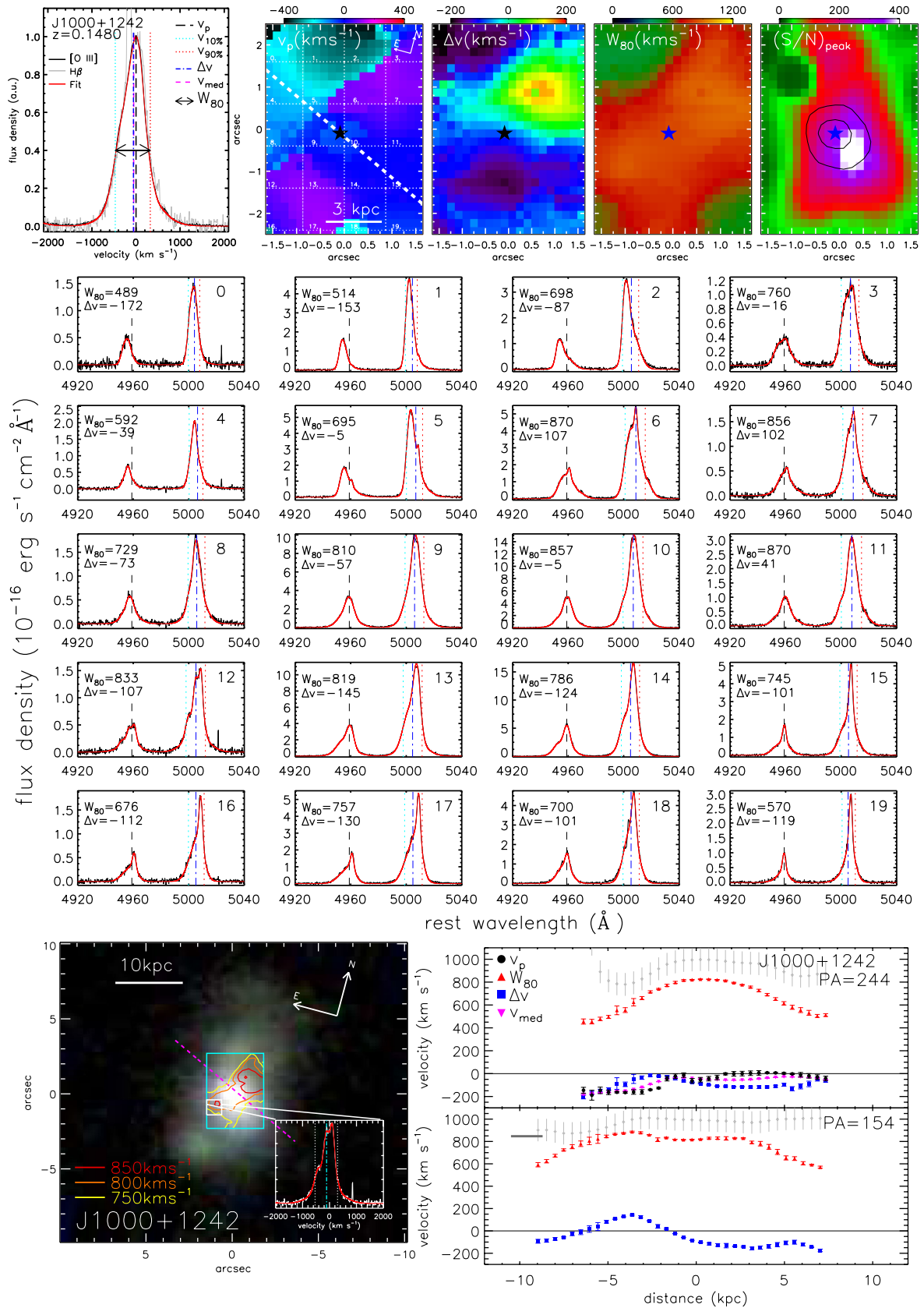
Figure A3. Same as Figs 5 and 6 but for SDSS J1000+1242.
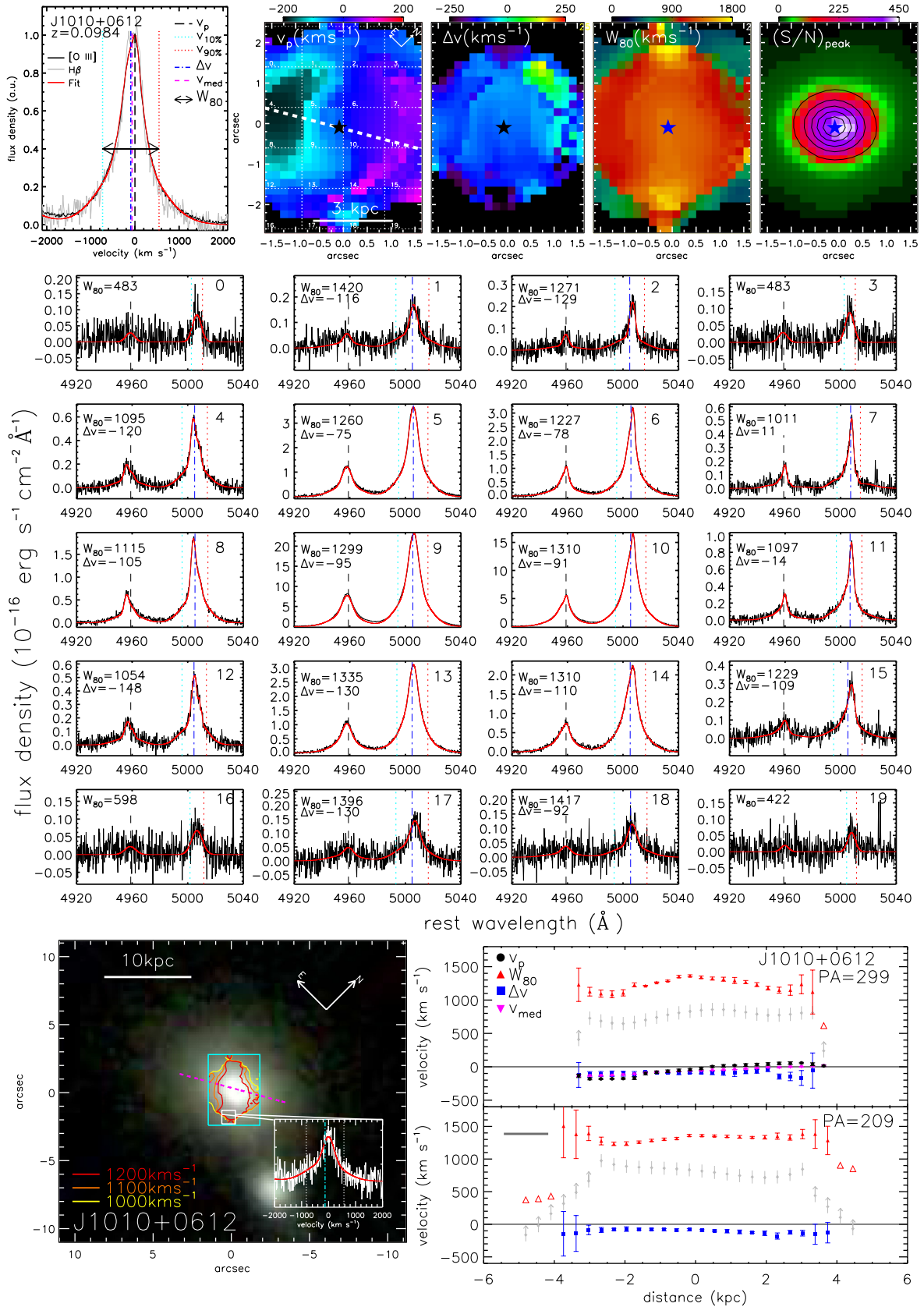
Figure A4. Same as Figs 5 and 6 but for SDSS J1010+0612.
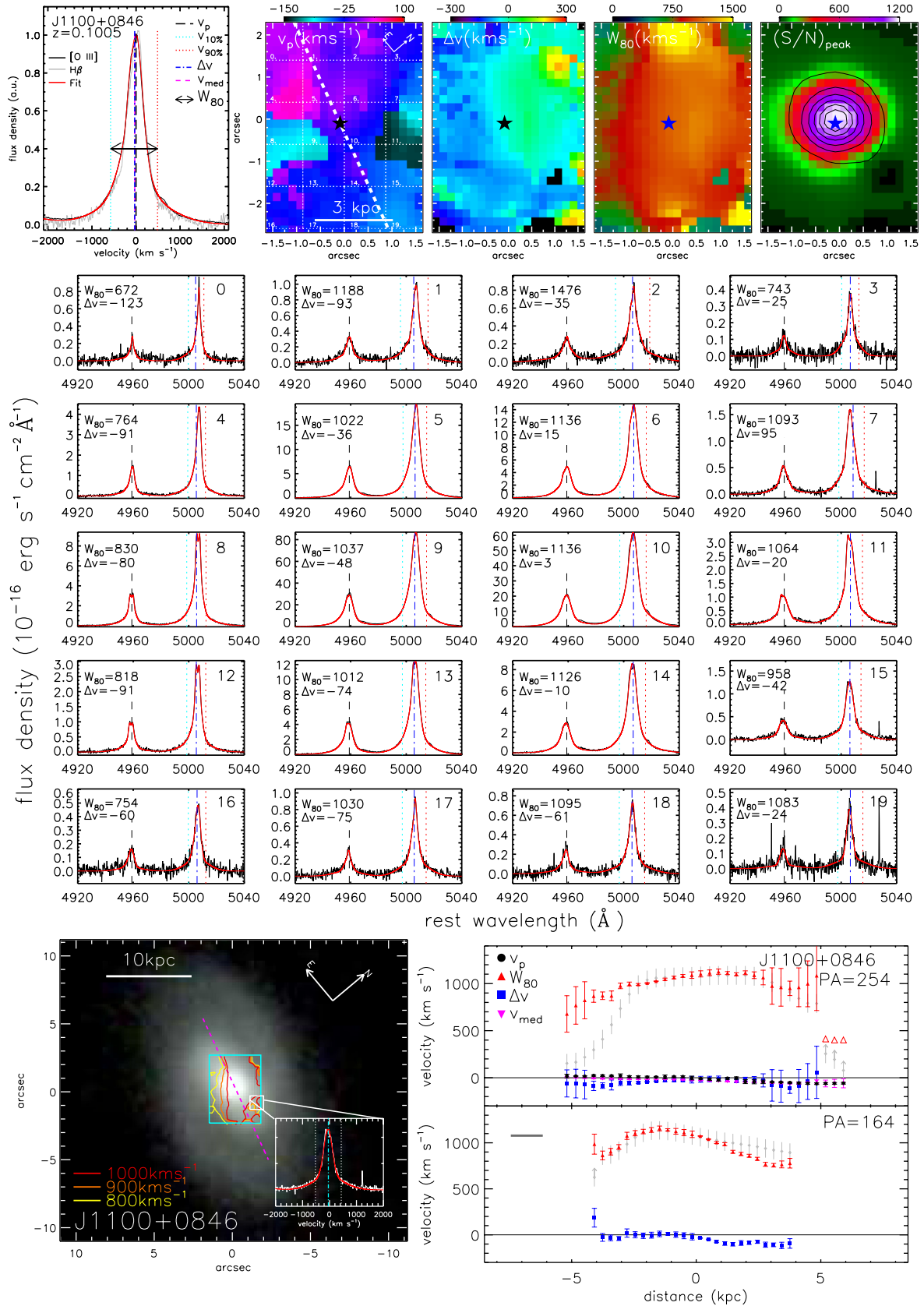
Figure A5. Same as Figs 5 and 6 but for SDSS J1100+0846.
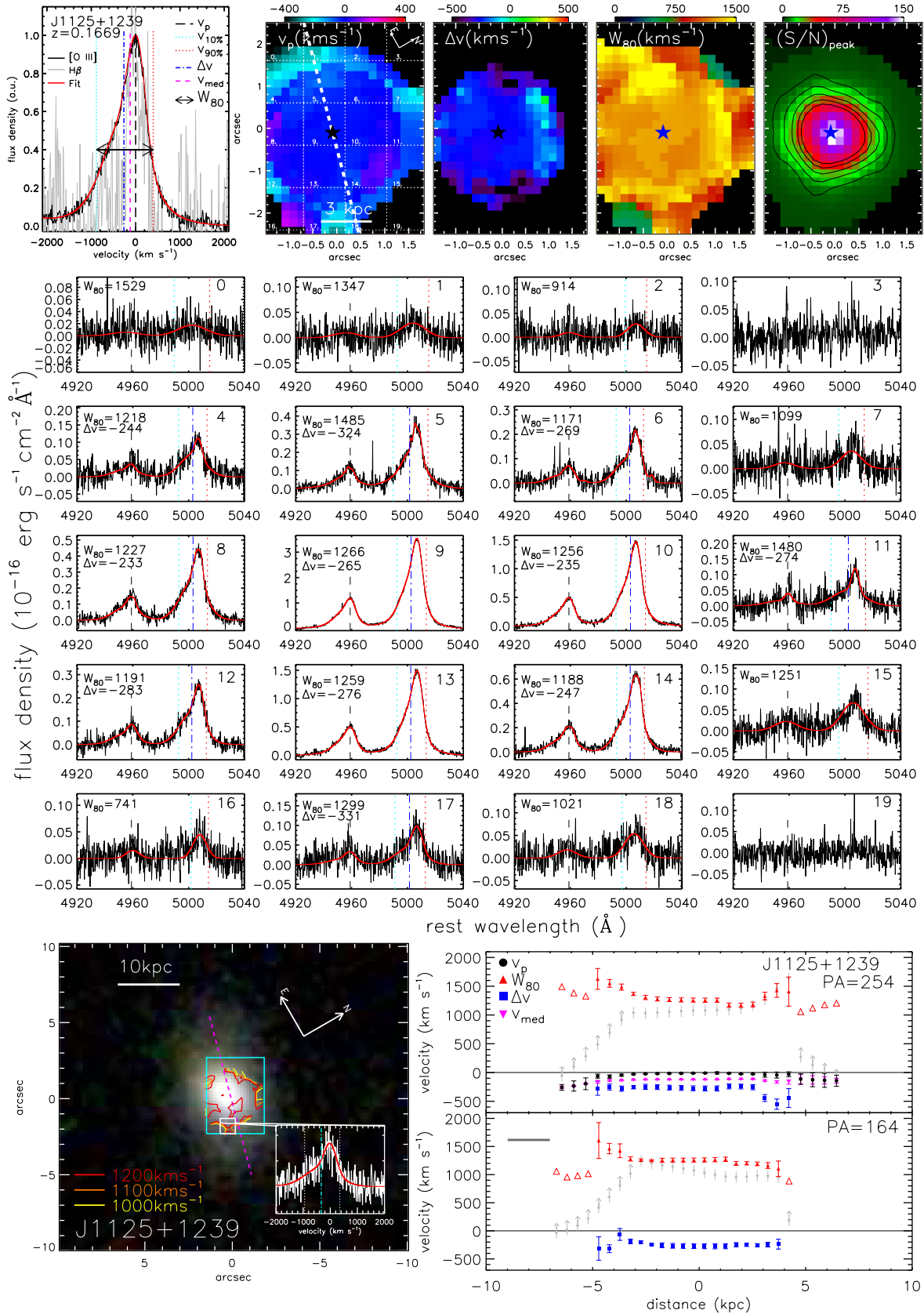
Figure A6. Same as Figs 5 and 6 but for SDSS J1125+1239.
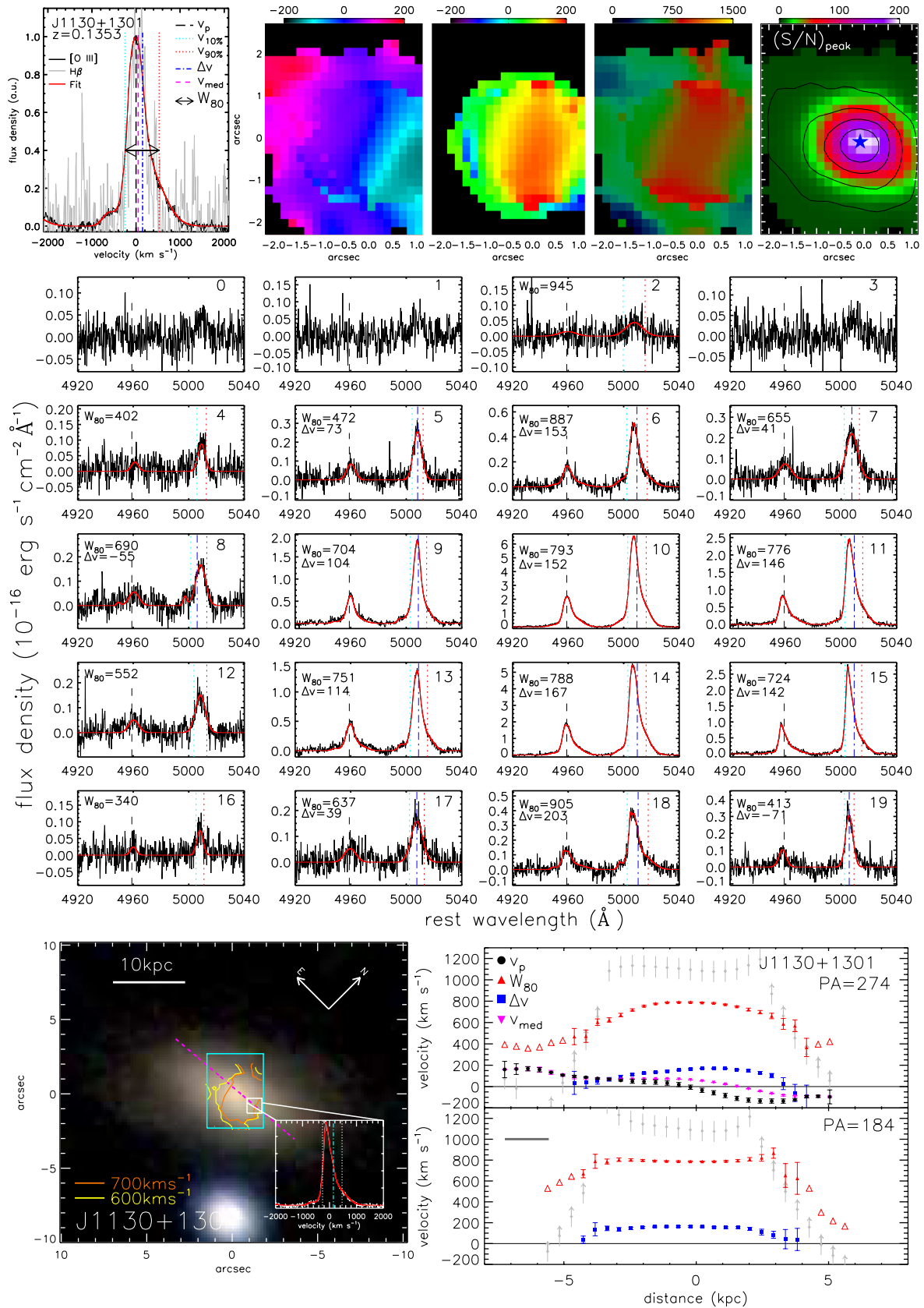
Figure A7. Same as Figs 5 and 6 but for SDSS J1130+1301.
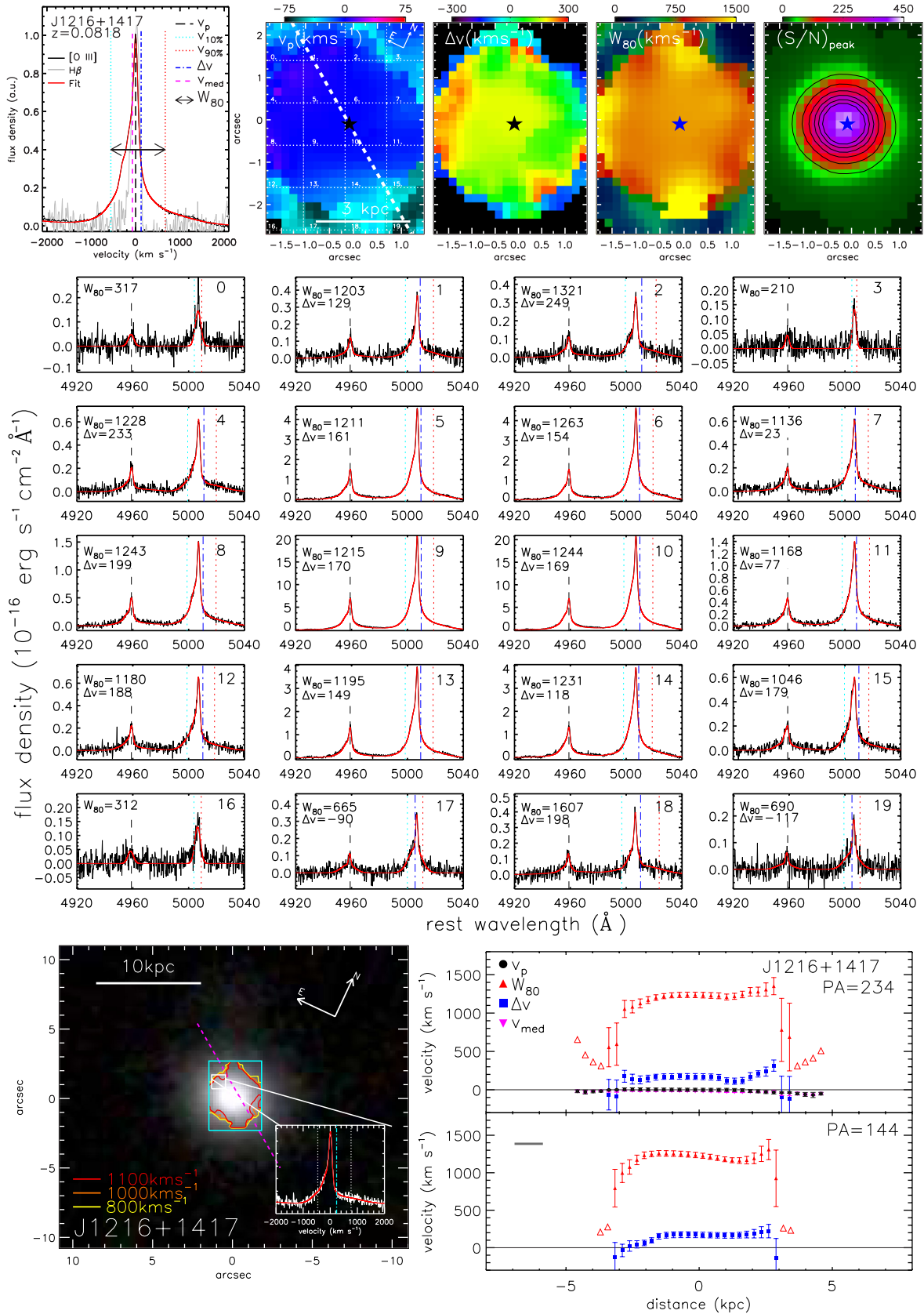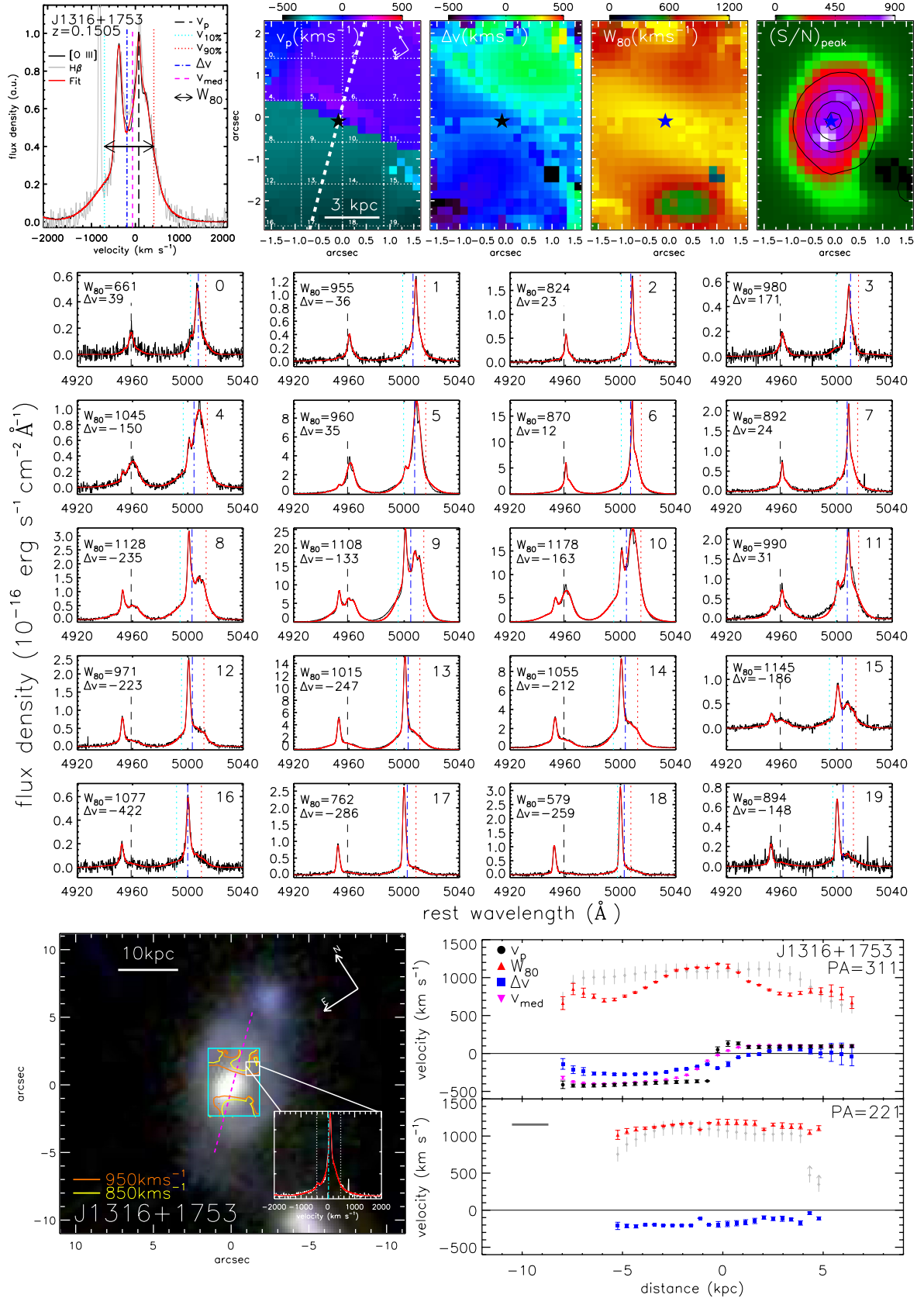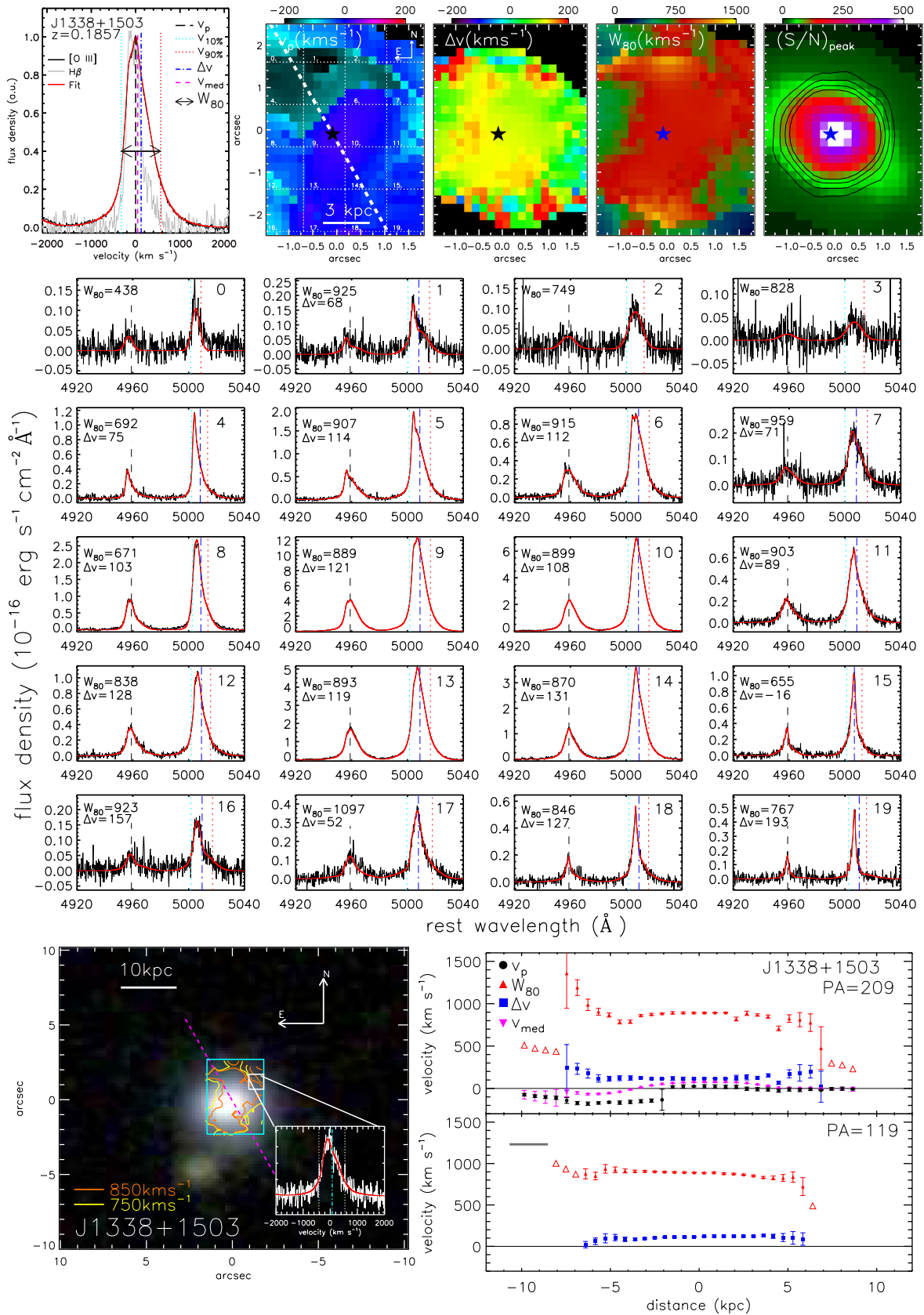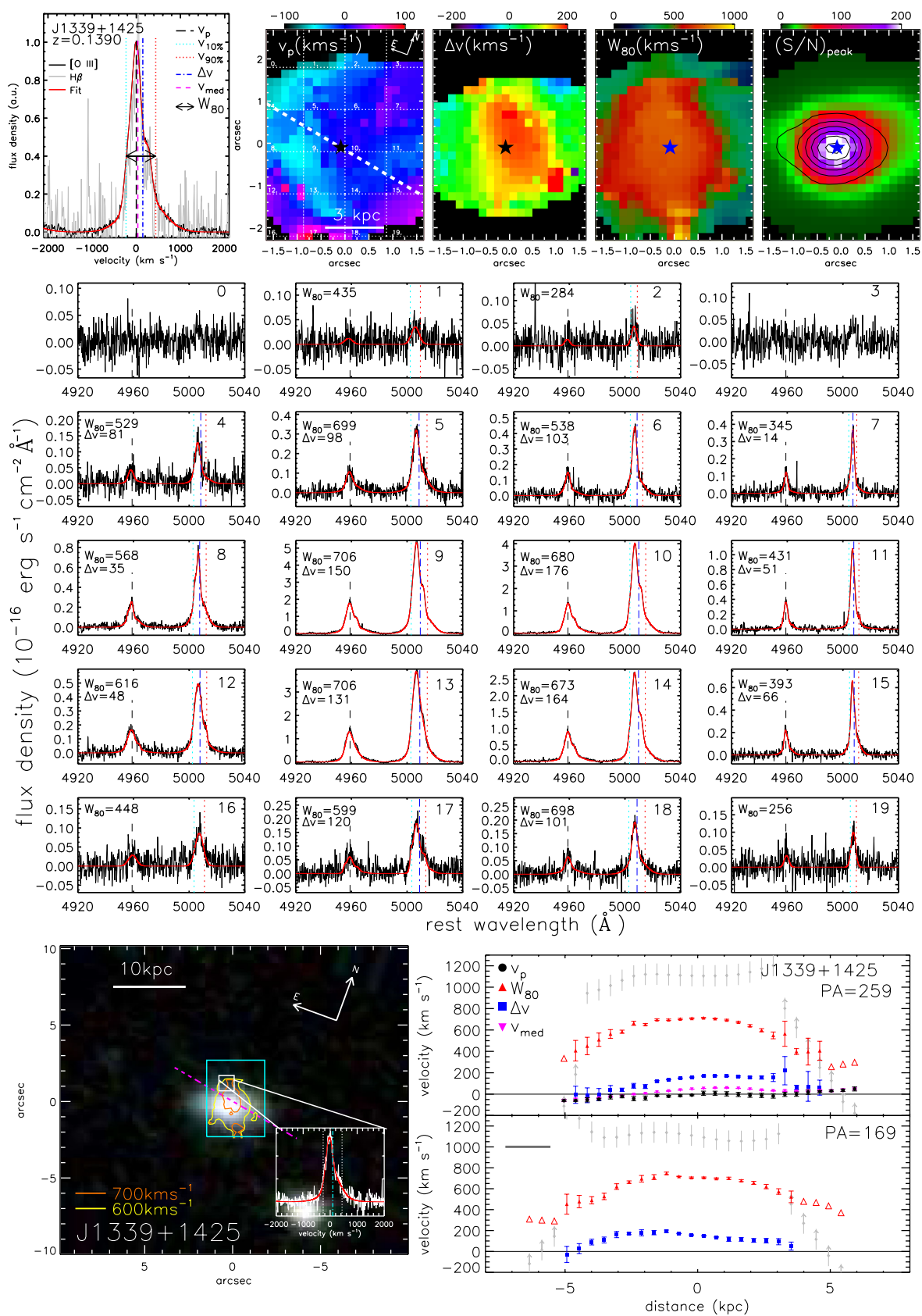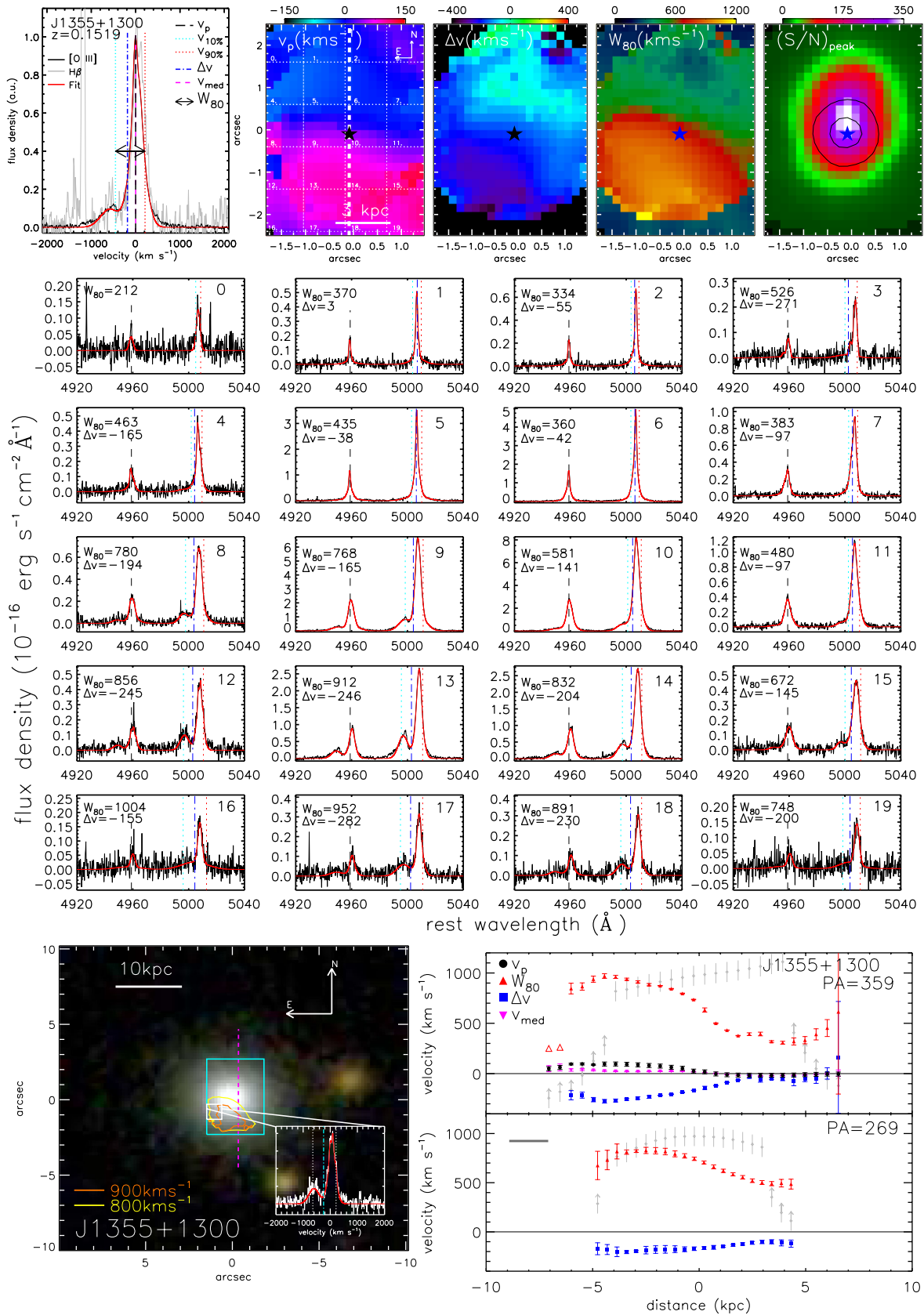
Figure A8. Same as Figs 5 and 6 but for SDSS J1216+1417.

Figure A9. Same as Figs 5 and 6 but for SDSS J1316+1753.

Figure A10. Same as Figs 5 and 6 but for SDSS J1338+1503.

Figure A11. Same as Figs 5 and 6 but for SDSS J1339+1425.

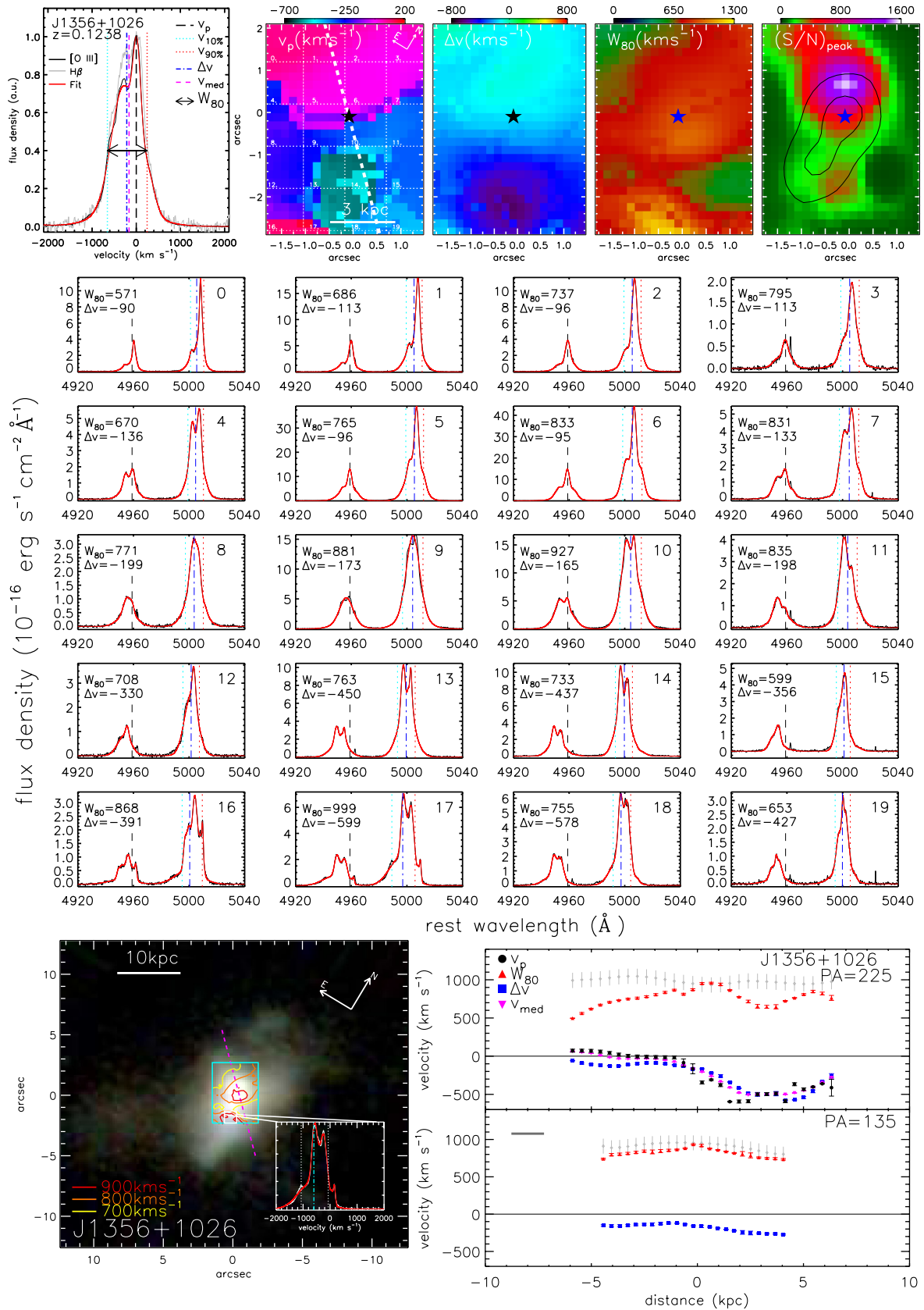**Figure A12.** Same as Figs 5 and 6 but for SDSS J1355+1300.

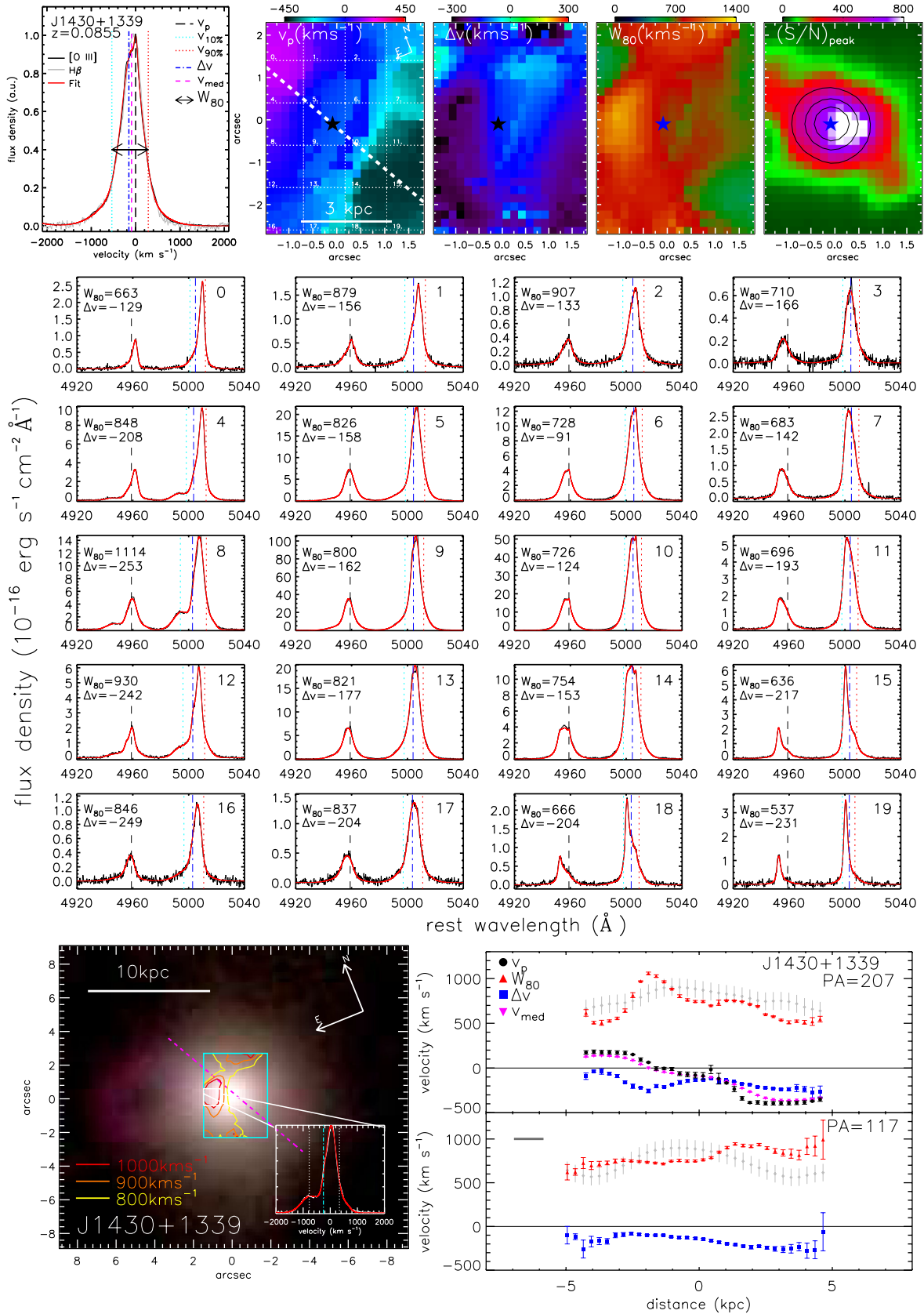**Figure A13.** Same as Figs 5 and 6 but for SDSS J1356+1026.

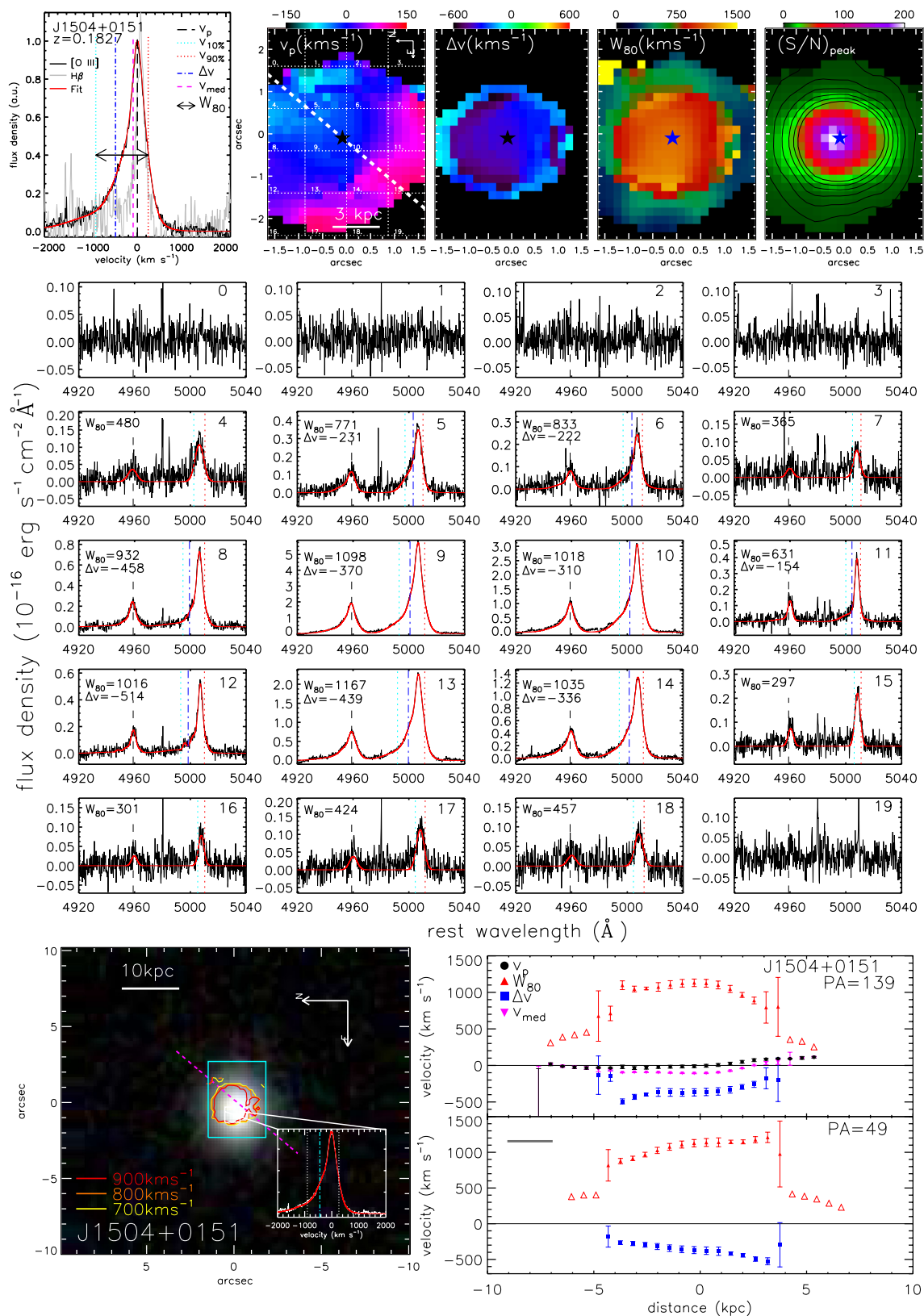**Figure A14.** Same as Figs 5 and 6 but for SDSS J1430+1339.

Figure A15. Same as Figs 5 and 6 but for SDSS J1504+0151.

This paper has been typeset from a TEX/LATEX file prepared by the author.